

**On the Reliability and Validity of
Electrophysiological
Computational Modeling to
Study Nerve Activation**

January 2015

José David Gómez Tames
Graduate School of Engineering
CHIBA UNIVERSITY

千葉大学審査学位論文

**On the Reliability and Validity of
Electrophysiological
Computational Modeling to
Study Nerve Activation**

January 2015

José David Gómez Tames
Graduate School of Engineering
CHIBA UNIVERSITY

Abstract

The development of electrophysiological computational modeling of the human body would provide new insights into the understanding of the underlying processes of biological systems. One important instance process is the effect of electrical stimulation which is affected by anatomical, electric, and stimulation factors and their interaction. Several studies have investigated them; however, they were not able to assess anatomical and electrical effects in a systematic way, and no studies have clarified the level of geometric detail and simplification of the formulation. This is why the aim of this study was to develop an electrophysiological computational model to investigate those factors for two purposes: 1) model validation and reduction, and 2) their role in nerve activation. A series of studies were carried out: 1) Simplification of the formulation. 2) Clarification of the geometric detail. 3) A novel method that combines tissue-equivalent phantom with known and adjustable dielectric properties to systematically study tissues properties in muscle activation. The results showed that 1) an optimal conductivity is valid for quasi-static approximation; 2) simplified models could predict the tendency of the nerve activation for parameters optimization; moreover, the presence of blood vessels and sciatic nerve in the model depends on the stimulation site; 3) a systemic study of the relationship between tissues and dielectric properties, and muscle activation can be achieved by using the novel human-phantom coupling experiment. Based on the insights acquired, a framework to evaluate different parameters can be translated to different physics to evaluate the trade-off between computation cost and prediction, which in turn, can help in the development of a complete biophysically based computational modeling of the human.

To my dearest family
A mi querida familia

Acknowledgements

I would never have been able to finish my dissertation without the guidance and support of my advisor and my committee members, help from colleagues of the laboratory and friends, and support from my family.

I would like to express my sincere gratitude to my thesis advisor, Dr. Wenwei Yu, for his excellent guidance, caring, lot of patience, encourage and support to go further in my research. I would also like to thank my committee members: Dr. Etsuji Yamamoto, whose very interesting observations help me to investigate further, Dr. Kazuyuki Saito, who allow me to visit his laboratory to learn about his work, and Dr. Tadashi Yamaguchi, for serving as my committee member.

I would especially like to thank my colleagues of the laboratory for providing a great atmosphere for doing research. To Jose Gonzalez, Yu Ikemoto, Rigo Martinez, and Yuan Baoping, who help me a lot when I came to Japan, provided me useful feedback and helpful advices. To Yuto Fukuhara and Siyu He, who help me a lot during the human-phantom coupling experiments. To Nevrez Imamoglu for his great support in the image processing of the model construction. To Dr. Kahori Kita for her careful revision of my thesis and presentation. Many thanks to Tapio T., Enrique D., M. Sekine, H. Soma, C. Hiroki, H. Suzuki and other workers in the laboratory.

Next, I would also like to thank Dr. Le Xie and Dr. Dongyun Gu, from Jiao Tong University, for their support in providing me a database of a human model and Ho-Yu Lin, from Ito-Saito laboratory in Chiba University, for his help.

Finally, I also would like to thank the Japanese Ministry of Education, Culture, Sports, Science and Technology for its financial support during my studies during the first two years. Also, I gratefully acknowledge the

funding by the Japan Society for the Promotion of Science during the last year (Grant-in-Aid for JSPS Fellows 14J06745).

A special thanks to my family and friends. Words cannot express how grateful I am to my mother, father, two sisters, and brother-in-law for all support and the sacrifices that you have made on my behalf.

Contents

List of Figures	xi
List of Tables	xv
1 Introduction	1
1.1 Background	1
1.1.1 Patient specific computational models	1
1.1.2 Electrical stimulation	3
1.1.3 Electrical stimulation models review	6
1.2 Motivation	7
1.3 Related work and problems	7
1.4 Aims and contents of the thesis	12
2 Anatomical and Electrophysiological Background	15
2.1 Overview	15
2.2 Neuronal and musculoskeletal interaction	16
2.2.1 Neuron	16
2.2.2 Skeletal muscle	17
2.3 Artificial stimulation of the axon	19
2.4 Dielectric properties of the human tissues	20
3 Implementation of the Bioelectrical Based Computational Model	21
3.1 Overview	21
3.2 Model	23
3.2.1 First step: voltage distribution	23
3.2.2 Dielectric parameters of the tissues	26

CONTENTS

3.2.3	Second step: nerve activation	27
3.3	Geometry	33
3.3.1	Semitendinosus muscle	34
3.4	Model analysis	38
3.5	Phantom experiments	39
3.5.1	Phantom materials	39
3.5.2	Phantom measurements	42
3.5.3	Human-phantom coupling	47
4	Validation and Simplification of the Quasi-Static Approximation For Neural Stimulation	49
4.1	Overview	49
4.2	Method	51
4.2.1	Formulation	51
4.2.2	Tissue-like phantom experiment	51
4.2.3	Measurement locations for the validation of the dispersive model	54
4.3	Results	55
4.3.1	Validation of dispersive model by tissue-equivalent phantom . . .	55
4.3.2	Optimal frequency for quasi-static approximation	56
4.4	Discussion	60
4.5	Conclusions	62
5	Geometric Representations of the Volume Conductor on Nerve Acti- vation	63
5.1	Overview	63
5.2	Method	64
5.2.1	Average fat thickness and bone-to-muscle distance	67
5.3	Simulation results	68
5.3.1	Nerve activity prediction by the CM and PM	68
5.3.2	CM and PM predicting AM-R nerve activation tendency	70
5.3.3	Effect of non-homogeneities in the activation of superficial nerves	71
5.3.4	Effect of nerve depth and curvature in the activation prediction .	72
5.4	Discussion	74
5.5	Conclusions	76

6	On the Dominance of the Tissues' Conductivity by Simulation Study and Human-Phantom Experiment	79
6.1	Overview	79
6.2	On the dominance of the tissues' conductivity in muscle recruitment . .	81
6.2.1	Method	81
6.2.2	Simulation results	82
6.2.3	Discussion	84
6.2.4	Conclusions	88
6.3	Human-phantom experiment to study the variation of the dispersive di- electric properties on the tissues	88
6.3.1	Method	88
6.3.2	Results	89
6.3.3	Discussion	90
6.3.4	Conclusions	97
7	Role of the fat thickness and electrodes	99
7.1	Overview	99
7.2	Current density study	100
7.2.1	Parameters	100
7.2.2	Results	100
7.2.3	Discussion and conclusion	102
7.3	Fat thickness study	104
7.3.1	Parameters	104
7.3.2	Results	104
7.3.3	Discussion and conclusion	105
7.4	Inter-electrode distance and area of the electrode	106
7.4.1	Parameters	107
7.4.2	Results	108
7.4.3	Discussion and conclusion	110
7.5	Electrode shape and current study	114
7.5.1	Parameters	114
7.5.2	Results	114
7.5.3	Discussion and conclusion	117

CONTENTS

8 Conclusion and Future Work	119
8.1 Conclusions	119
8.2 Future work	122
References	123
Publication List	133
A Nerve Activation Model	137
B Lumped Model Equations	141

List of Figures

1.1	Basic steps for the implementation of patient specific computational models.	2
1.2	Factors that influence nerve activation.	8
1.3	Proposed solution.	13
2.1	Motor neuron structure.	17
2.2	Action potential.	18
3.1	Two-step solution for nerve activation.	22
3.2	Solution steps of the dispersive model.	24
3.3	Dispersion of the tissues employed in the models calculated by 4-Cole-Cole equation.	28
3.4	Compartment model of the myelinated fiber.	29
3.5	Dynamics of the CRRSS model for a given node of Ranvier.	32
3.6	Two-step method summary.	33
3.7	Geometry extraction process.	34
3.8	Cylindrical simplification of the thigh.	35
3.9	A simplified geometry of the semitendinosus muscle	36
3.10	Diameter distribution of the motor nerve axons in the sciatic nerve. . .	36
3.11	Endplates band.	37
3.12	Recruitment-duration curve	37
3.13	Activation volume in the CM.	38
3.14	Activation depth.	39
3.15	Example of the selectivity of two different TES configurations.	40
3.16	Example of MT before and afterwards an action potential is elicited. . .	40

LIST OF FIGURES

3.17	Convergence of the MT solution for different volume conductor geometries.	41
3.18	Output voltage of the DM for constant amplitude and MT conditions. .	42
3.19	Measurement set up of the dielectric properties	43
3.20	Verification of the phantom measurement experiment.	44
3.21	Dispersion of fat-equivalent phantom.	45
3.22	Dispersion of muscle-equivalent phantom.	46
3.23	Human-phantom coupling experiment.	47
4.1	Experimental set up to measure the voltage in the tissue-like phantom. .	52
4.2	Voltage distribution in the phantom at 2 kHz	53
4.3	Selected locations for potential measurement in the phantom.	53
4.4	Output voltage obtained from the DM and RM	54
4.5	Flow diagram for the validation and simplification of the formulation. .	55
4.6	Voltage at different depths using current stimulation	57
4.7	Voltage along x-axis locations using current stimulation	57
4.8	Voltage along z-axis locations using current stimulation	58
4.9	Voltage along z-axis locations using voltage stimulation	58
4.10	Voltage at different pulse durations	59
4.11	Mean error of the voltage calculated between DM and RM	60
4.12	Error of the MT between DM and RM	61
5.1	Different geometries of volume conductors derived from the thigh. . . .	66
5.2	Flow diagram for the verification of simplified geometries.	67
5.3	Projections of the tissues boundaries.	68
5.4	Distribution of the activation error of the PM and CM	69
5.5	Geometry discrepancy of bone location and fat thickness	70
5.6	Cross-Correlation between models.	71
5.7	Distribution of the activation error of AM-(VN)' with respect to AM-R	72
5.8	Effect of nerve depth.	73
5.9	Influence of the curvature on the MT	74
5.10	Optimization of CM geometry.	77
6.1	Recruitment of three models with different conductivity configurations .	82

LIST OF FIGURES

6.2 Comparison of the recruitment percentage between models to determine the conductivity dominance by layer.	83
6.3 Recruitment vs. conductivity of skin, fat, and muscle layers at 200 mA.	84
6.4 Lumped model.	87
6.5 Geometry representation by concentric cylinders.	90
6.6 Normalized MT using fat-equivalent phantom with three different conductivities for the human-phantom coupling experiment and simulation.	91
6.7 Effect of the inter-electrode distance in the human-phantom coupling experiment.	92
6.8 Simulation of the dispersive conductivity variation for current and voltage stimulation.	93
6.9 Effect of the current and voltage stimulation using the lumped model.	94
6.10 Simulation of the effect on the MT of the dispersion of the electrodes during the experiment.	95
6.11 Transfer functions for (a) current and (b) voltage stimulation	96
7.1 Current density at the boundary between different tissues.	101
7.2 Percentage of the total input current density at the boundaries between the tissues.	102
7.3 Effect of the fat thickness in the laterally distribution of the current.	103
7.4 Effect of the fat thickness in VAV and AD.	105
7.5 AV vs. inter-electrode distance.	109
7.6 AD vs. inter-electrode distance.	110
7.7 Selectivity vs. inter-electrode distance.	111
7.8 Shape of the AV at different inter-electrode distances.	113
7.9 Depolarization and hyperpolarization regions under the cathode and anode electrode.	113
7.10 Effect of the current density in AV, AD, and selectivity.	116

List of Tables

1.1	Applications and problems of electrical stimulation	4
3.1	Materials for the fat-equivalent and muscle-equivalent phantoms	43
4.1	Estimation error of the voltage using the DM	56
4.2	Summary of the optimal frequencies to approximate DM by RM	62
5.1	Geometry and conductivity parameters of the models	64
6.1	Electrical parameters of the tissues and dimensions	81
7.1	Parameters to study the transmission of current	100
7.2	Simulation parameters to study the effect of fat thickness in nerve activation	104
7.3	Parameters to study the influence of inter-electrode distance and size of the electrode in nerve activation	108
7.4	Simulation parameters to study the effect of current intensity and shape of the electrode in nerve activation	114
7.5	Motor threshold for a small and large electrode using a round and square electrodes	115
A.1	Parameters of the CRRSS nerve model	139
A.2	Comparison of nerve models	140

Abbreviations

Abbreviation	Description
AD	Activation Depth
AF	Activating Function
AM	Anatomical Model
AP	Action Potential
AV	Activation Volume
BMAC	Burst-Modulated Alternating Current
CM	Cylindrical Model
CRRSS	Chiu-Ritchie-Rogart-Stagg-Swenney
DM	Dispersive Model
FEM	Finite Element Model
FES	Functional Electrical Stimulation
HC	High Conductivity
HH	Hodgkin-Huxley
LC	Low Conductivity
MRI	Magnetic Resonance Imaging
MT	Motor Threshold
PC	Pulse Current
PDE	Partial Differential Equation
PM	Parallel Model
PW	Pulse Duration
RM	Resistive Model
SM	Standard Model
ST	Semitendinosus Muscle
TES	Transcutaneous Electrical Stimulation
VAV	Volume of the Activation Volume

Chapter 1

Introduction

1.1 Background

1.1.1 Patient specific computational models

The full understanding of the exact behavior of the different biological processes, their interrelationships, and the root of different pathologies is not complete. This is partially due to limitations of experimental studies such as their high cost, accurate measures and the difficult to systematically reproduce certain natural, pathological or degenerative situations. Therefore, detailed models can generate insights to understand and interpret experimental data. The governing equations of biological processes in combination with realistic biological properties, computational analysis techniques and medical imaging techniques (CT, MRI) provides the tools necessary for biophysically based computational modeling by integrating different range of spatial and temporal scales with different physics (multi-scale and multi-physics modeling); for instance, electromechanics (kinematics and excitation-contraction coupling for muscle activation and motion), fluids dynamics (cardiovascular and circulatory system) as shown in Fig. 1.1.

Reliability and validity are fundamental in the simulation and model implementation. Reliability is the consistency of the obtained results; therefore, the model geometry approximation, formulation, sensitivity of the model results to parameters, and convergence of the solution should be investigated in the context of simulation results. Validity is the degree of how close the simulation results are to the experimental results,

1. INTRODUCTION

and therefore, especial attention should be paid to the selection and implementation of the equations and material properties for the model.

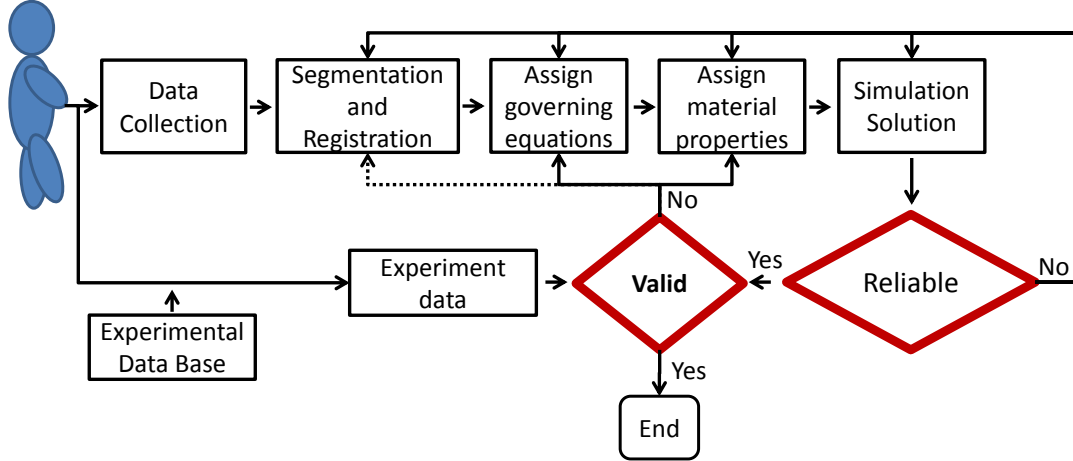


Figure 1.1: Basic steps for the implementation of patient specific computational models. Based on (1).

Some challenges should be overcome to make computational model possible in clinical application: 1) Create tailored anatomically based models efficiently. 2) Assure reliability and validity. 3) Model reduction for over detailed geometry and over-parameterization. 4) Multi-scale and multi-physics model integration (2). From this models, new tools are expected for prevention, prediction of diseases and therapies using a holistic approach, such as the virtual physiological human project (2, 3).

Models with different physics formulation (multi-physics) need to be integrated to represent complex biological processes. One of these processes is electro-physiological. It has been implemented analytically and numerically to explain the generation, propagation, and responses of neural activities. Applications include muscle condition assessment by electrical impedance myography (EIM) (4), understanding, interpretation, and application of electromyogram (EMG), electroencephalography (EEG), and electrocardiography recordings (ECG) (5, 6), electrical impedance tomography (EIT) (7), and evaluation of antenna transmission within tissues for body-area network applications (BAN) (8). Moreover, simulations of the neurons' polarization and depolarization when responding to external stimuli have been developed, such as transcranial magnetic stimulation (TMS)(9), spinal cord stimulation (SCS) (10), and functional electrical stimulation (FES) (11, 12, 13). These studies can be categorized in three

different levels: 1) generation, process, and transmission of bioelectrical signals, 2) biosignals measurement, processing, and analysis (EEG, ECG, EMG), 3) control of electrophysiological process by imposing and external electric field: EIT, EIM, TMS, FES, SCS, etc. This study focused on electrical stimulation.

1.1.2 Electrical stimulation

Electrical stimulation artificially activates the neuronal tissues by the electric field introduced through superficial electrodes. That is possible if the electric field generates enough change in the extracellular voltage to depolarize the fiber membrane to a level sufficient to generate an action potential (AP) to evoke muscle contractions.

Some applications are the following (Table 1.1):

1. Functional recovery as therapeutic and orthotic aid in medicine to neurologically impaired individuals: upper limbs (grabbing) and lower limb (drop foot syndrome (14, 15) and cycling (16, 17))
2. Rehabilitation and training method: 1) maintenance and recovery of muscle mass and function during extended disuse or immobilization (18, 19) and 2) improvement of muscle function (20, 21, 22, 23).
3. In vivo assessment of the neuromuscular function of healthy and impaired muscles: standardized muscle contractions can be induced to evaluate function of intact muscle (e.g., force-frequency relationship, fatigability during constant stimulation, and nerve conduction studies) (21).
4. Pain relief (24) and sensory prosthesis (25).

Electrical stimulation presents two basic problems (Table 1.1): 1) strong discomfort associated with the peripheral stimulation (26, 27) and 2) incomplete spatial recruitment of muscle fibers (28, 29, 30).

Voluntary contractions presents size related orderly recruitment: from small, typically slow, motor units to the larger, typically fast, motor units (Henneman size principle) and being quite temporal asynchronous to reduce fatigue. On the contrary, reversal of the motor unit activation order would be expected in electrical stimulation since large-diameter axons of the fast units are more easily excited by imposed electric fields than are small-diameter axons of the slow units. However, in the case of in

1. INTRODUCTION

vivo muscle stimulation, the imposed electric field generates a random or disorderly recruitment regardless of the fiber type (31, 32). Therefore, electrical stimulation recruits motor units in a nonselective, spatially fixed, and temporally synchronous pattern rather than in a reversal order (29). The spatially fixed recruitment (current density decreases with increasing depth) implies that the same motor units are repeatedly activated by the same amount of electrical current which contributes to increased muscle fatigue when compared with voluntary contraction. Other studies have indicated that the recruitment pattern was not exclusively superficial, but rather dispersed if stimulation is directly over the nerve trunk that innervates the muscle under interest rather than the muscle belly (33, 34) or if the motor entry zone is superficially close to the stimulation electrode. In both cases, control and durability are affected (35, 36).

Table 1.1: Applications and problems of electrical stimulation

Applications	Problems
Functional recovery	Control
Rehabilitation	Durability
Training method	Inter-individual variability
In vivo assessment	Assessment of comfort and selectivity
Pain relief	

Different stimulation parameters have a direct effect in the muscle response:

1. Lower frequency (10-30 Hz) could produce more lasting periods than higher frequencies (50-80 Hz).
2. Higher amplitude has a stronger depolarizing and deeper effect in the structures underlying the electrodes.
3. Pulse width or pulse duration is characterized by the strength-duration curve which is a plot of the threshold required for stimulation vs. pulse duration in a hyperbolic-like relationship with the current required increasing with decreasing pulse duration (37, 38).
4. Muscle tissues was able to recover faster and produce greater torque using duty cycle as compared to when constant stimulation patterns were used (39, 40).

5. Larger surface electrodes are more dispersive (less selective) but activate larger regions of a muscle and increase comfort, and smaller electrodes produce a more focalized concentration of current densities; thus, less crossover stimulation of nearby muscles but with a reduction of comfort (41, 42).
6. Different stimulation schemes, such as pulse current (PC) and burst-modulated alternating current (BMAC), and different parameters for these schemes have been proposed to elicit greater muscle torque while keeping discomfort low, PC stimulation usually has a pulse frequency ranging from 1 Hz to about 100 Hz. BMAC stimulation is a kilohertz-frequency AC, delivered in bursts, with the burst frequency generally up to 100 Hz. Examples of BMAC are Russian, interferential, and pre-modulated stimulation (43). Interferential stimulators produce two independent kilohertz-frequency with constant intensity applied by two separate pairs of electrodes located diagonally opposed to generate an interference effect in the central intersection region. The resulting waveform has a modulated frequency equal to the difference between the two independent AC frequencies at the muscle. Pre-modulated stimulation is similar to interferential current, but its current is modulated before applied into the tissue. Russian stimulation is modulated at low frequencies, typically 50 Hz. Some studies favored the BMAC stimulation over PC stimulation, especially for short duration bursts (2 ms to 4 ms) (43, 44). It is argued that the modulated frequency reduces the pain or discomfort and increases force-generating capacity. One argument to support this result is that the skin impedance is lower at high AC frequencies; therefore, more energy will be transmitted deeper into the muscle, increasing the force generation when compared with low-frequency pulse current. On the other hand, other studies have claimed that PC stimulation had better force production and was more comfortable than BMAC stimulation (45, 46, 47) or at least there was no difference (48). They showed that interferential and Russian waveform were somehow more comfortable than square wave stimulation, but Russian and interferential stimulation required higher currents to achieve the same force by square wave stimulation because of the poor penetration into the muscle. Also, their results indicated stimulating by sine waveform stimulation generated significantly higher

1. INTRODUCTION

muscle force and less pain than square wave, Russian or interferential stimulation at that same current intensity.

1.1.3 Electrical stimulation models review

Computational models in musculoskeletal rehabilitation using electrical stimulation in terms of daily physiological condition, dynamical motion, and multi-scale (skin, fat, motor unit, musculo-skeletal level), multi-physical human body system are necessary to study the nerve activation responding to different configurations of electrical stimulation (49, 50, 51, 52) may provide a deeper understanding to improve selectivity of nerves and comfort to the patient.

Hodgkin-Huxley model (1952) (53) was the first model to describe that neural signals propagates as membrane voltage along a nerve fiber axon on the non-myelinated squid axon using the space clamp experiment (stimulation without propagation). This model lead to subsequent models, such as Frankenhaeuser-Huxley (myelinated frog, 1964) (54) and CRRSS (mammalian myelinated fibers, 1987) (55, 56). Furthermore, McNeal (1976) (57) developed a compartment model for myelinated nerve fiber and its response to external point source stimulation. A derivation of his work was the activating function (AF) which explains the basic mechanism of external stimulation without complicated ion-channels dynamics (58). The usage of compartment models and activating function permit the study of nerve activation using electrical stimulation.

In past studies, a two-step method has been adopted for superficial stimulation using the compartment model (41, 59, 60). The first step is the calculation of potentials within the tissues produced by the external stimulation. The second step is the prediction of an AP of the nerve or muscle fiber due to extracellular potentials generated by the stimulation. Finite element method (FEM) or Finite difference model have been used to study electrical stimulation in a multi-layer and physically based models (skin, fat, muscle, bone). The previous models have been extended to anatomically-based multi-scale model comprising electro-physiological properties of individual cells and anatomical distribution of muscle fibers with muscle dynamics (61, 62, 63). They are capable of the implementation of an electromechanical skeletal muscle behavior (motor unit recruitment, force generation, and fatigue) to analyze, for example, effects of muscle fatigue given a specific multi-electrode array arrangement.

1.2 Motivation

The development of electrophysiological computational model of the human body provides a deeper understanding and new insights of the mechanism and control of the underlying processes of biological systems. For that, the model and simulation should be able to express, quantify, and reproduce the phenomenon. For instance, electrophysiological modeling has revealed that the optimal location of the electrodes for activation of denervated muscle fiber changes according to the electrode-fiber distance: central region for near field and borders for far field (64). Also optimization of electrode material and size for better muscle activation have been clarified (42, 65).

One important instance process is the effect on discomfort and spatial recruitment of electrical stimulation. Those effects, at the same time, are affected by anatomical factors, electric properties, stimulation factors, and their interaction (Fig. 1.2), which in turn, affect the nerve activation, force, and motion; therefore, they should be investigated in detail for the reliability and validity of electrophysiological computational modeling.

1. Anatomical factors: tissues shape, size, and location. (Inter-individual difference and medical conditions such as obesity.)
2. Electrical properties factors: dielectric properties. (Variation of the dielectric properties of the tissues can happen under natural processes, like aging (66), or under natural conditions, such as moisture in the skin (67). Muscle conductivity can be changed after acute denervation injury (4), and temperature can increase or decrease blood flow, which directly affects the impedance of the body (68).)
3. Stimulation factors: electrode material and shape, waveform, and location of the electrodes. (Revised in detail in previous subsection: “Electrical stimulation”.)

1.3 Related work and problems

The study of those factors can be conducted by experimental or computational methods. On the one hand, quantification of muscle selectivity and activation regions, and systematic assessment of the anatomical and electrical properties effects in nerve activation are difficult in experimental method approaches. For example, the control of the

1. INTRODUCTION

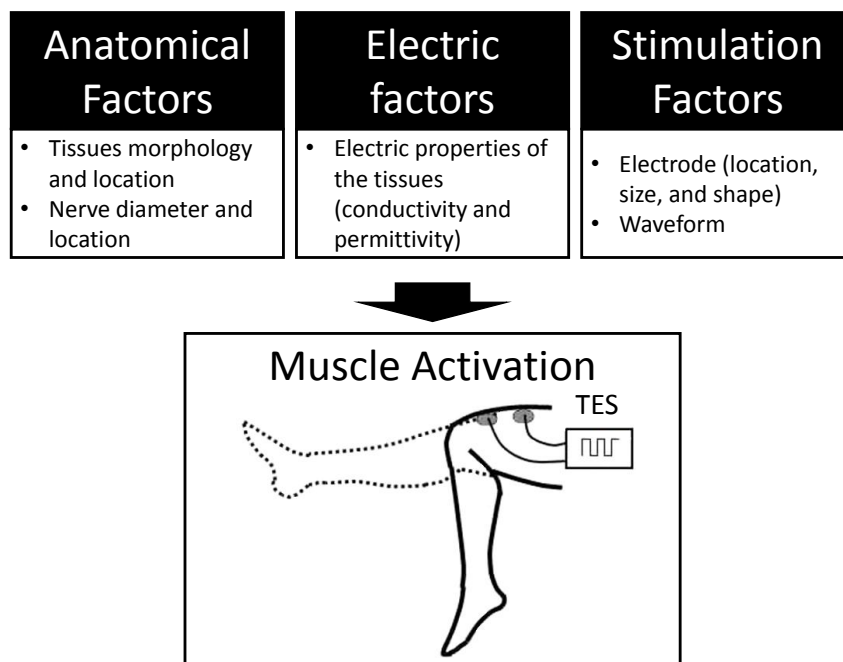


Figure 1.2: Factors that influence nerve activation. These factors affect directly the stimulation and should be considered during the implementation of the model.

fat thickness effect and the variation of electrical properties of tissues in several patients is very demanding in experimental methods. Moreover, the measurement of selectivity and depth of the activation is difficult, invasive, and exhausting for the subjects. Thus, computational model approaches prove to be useful to overcome these issues. On the other hand, computational methods lack enough validation studies and a clear implementation requirements of its geometries. For example, there are no studies that 1) clarified the level of geometric detail and which tissues should be considered or neglected, 2) investigated the conditions for quasistatic simplification in transcutaneous electrical stimulation (TES), 3) and validated formulations that accounts the electrically dispersive properties of the tissues. A literature review related to experimental and computational methods and its problems are presented in the following paragraphs.

Several experimental studies measured and calculated the current density distribution and transmission within the tissues (45, 69, 70) but without considering the role of the variation of the tissues conductivity in nerve activation and force production. Also, there are no experimental studies that investigate the role of tissues' conductivity in the recruitment because of the complexity of isolating the effect of each tissue and

comparing the same tissues with different conductivity values in vivo.

Simulation models are a complementary solution but their validation is a fundamental step. The validation could be verified by measuring potential distribution in the tissues and nerve activation. Experimental validation of the potentials are conducted by needle and surface electrodes, and experimental validation of the nerve activation is measured indirectly by recruitment-duration curves and strength-duration. Transient finite element model has shown close results to experimental measurements in the muscle and skin for non-harmonic input signal (when the tissue materials were fitted) (71, 72) and quasi-static model for harmonic input signals (73). Also, the nonlinear dynamic property of the tissues of human skin has been modeled and validated by using a lumped model (74). However, the non-linearity of skin was shown to be not relevant for nerve activation in a transient finite element model study (75) for current stimulation. Moreover, transient and quasi-static models have predicted experimental measurements of strength-duration and recruitment-duration curves to validate the computation of the nerve activation (76).

The Laplace equation is used to calculate the electric scalar potential (V_e). If electrically dispersive tissues are included, the model is capable of describing more realistic calculations of the potentials generated by non-harmonic stimulation signals than, for example, quasi-static approximation approach. However, there are not any validation experiment for the dispersive model in literature. Most of the simulation models for electrical stimulation assume that the quasi-static approximation is valid: capacitive, inductive, and wave propagation are ignored, which are based in (77) for signals originated from the cells that have a low spectral content (e.g., electrocardiography, electromyography and electroencephalography). In the case of neural stimulation, short pulse duration with higher frequency components could invalid some of the simplifications. However, Bossetti et al. (78) confirmed that propagation and inductive effects can be also ignored for neural stimulation; on the contrary, ignoring the capacitive condition is still a questionable simplification for specific tissues, such as skin and to a lesser extent muscle. Moreover, the electrically dispersion of the tissues (frequency-dependent) presents a filtering effect in the potential distribution, which in turn, affects the neuronal excitation. Therefore, some studies have investigated the impact of the strong frequency dependence of the tissues on the potentials. Stoykov et al. (79) argued that the dielectric properties of the tissues are more significant when high-frequency

1. INTRODUCTION

components are present in the power spectrum of the stimulation. They showed that dispersion can cause a high error for high frequency components of the EMG employing cylindrical muscle. In addition, Butson and McIntyre (80) showed that the quasi-static approximation may produce an overestimate of the volume of tissue activated by neural stimulation and larger errors with shorter pulse widths during current-controlled stimulation and with longer pulses during voltage-current stimulation. However, conductivity was fixed and only limited to a number of permittivities in their analysis using a cuboid geometry for brain tissue. Also, it has been suggested that dispersion may be approximated by resistive (78) and capacitive models (81). Bossetti et al. (78) compared the quasi-static approximation (resistive model) with a homogeneous analytical model, considering a point current stimulus in infinite space. He showed that the exact solution for the potential can be approximated by an appropriate value of the conductivity for the quasi-static solution. Grant et al. (81) showed that capacitive model (fixed conductivity and permittivity) also approximates a dispersive mode for an ellipsoidal geometry model of the intracranial conducting volume. However, the referred simulation studies made use of over-simplified geometries focused on brain stimulation and no experimental validation has been conducted to confirm the optimal frequency. In addition, most of the simulation studies of TES didn't incorporate the electrically dispersion of the tissues; they used the quasi-static approach.

Different volume representations have been used during model simulation studies: anatomical, cylindrical, and parallel structures. Parallel layered model (PM) and cylindrical layered model (CM) are of extended use (5, 41, 60, 82, 83, 84) because they are simpler to implement (no need of image segmentation), less computationally expensive (axial symmetry for the limbs), and easier to reproduce in phantom tissues for validation tests. For instance, Doheney et al. (60) investigated the effects of fat thickness to optimize the inter-electrode distance and electrode size parameters. On the other hand, the anatomically based model (AM) better reflects the influence of tissue irregularities on the current distribution and nerve activation. In addition, as the CM and PM are usually constructed with concentric cylinders and cubes, the discrepancy of the fat thickness and bone location with AM can partly influence the muscle activation. Krasteva et al. (85) showed that the omission of non-homogeneities can also introduce misleading errors in a simulation study of peripheral nerve stimulation in an AM. Thus, evaluating the limitations of different implementations of bioelectrical models

is fundamental to investigate how close the solution of this simplified model is to an anatomical model. However, there are no studies aimed at clarifying the level of geometric detail necessary to represent the tissues and which tissues should be considered or which could be neglected. For instance, even though nerve trunk and blood vessel have an appreciable volume their influence in the spatial distribution of the voltage is often omitted (63, 86).

Computational models have investigated the role of electric properties of the tissues involved in electrical stimulation. The effect on muscle activation of the interface's conductivity between an electrode array and the skin was studied to improve selectivity (65, 82). Livshitz et al. (59, 87) presented a model with three tissue layers as an extension of the previous analytical model to study the current density distribution through the tissues and force production; however, that study did not consider nerve model or muscle conductivity variation, or, anatomical characteristics. Sticker et al. (83) inspected the excitability of muscle fibers on denervated muscle after training by simulating changes in the conductivity and size of the muscle. Additionally, simulation of muscle deformation, configuration of muscle fibers, and distribution of the innervation zone have been also inspected (84).

Different studies have investigated stimulation factors, such as the effect of electrode size, configuration, resulting current distribution, nerve excitation, selectivity and comfort. Martinek et al. (88) developed a model for the fibers of denervated skeletal muscles in conjunction with FES via surface electrodes. They studied the percentage of activation of the muscles for a variable stimulation time and different inter-electrode distance. Kuhn et al. (41) used a computation model to study comfort and selectivity parameters to determine the optimal size of the electrode among (0.64, 1.96, 5.29, 10.64 and 16.81) cm^2 in different fat thickness (0.1 , 0.6 , 1.1) cm. They obtained that: 1) motor threshold increases with larger electrodes, 2) selectivity decreases with larger electrodes, 3) comfort is related with electrode size, fat thickness, and target region of the stimulation: small electrodes, thin fat layers and superficial nerves or larger electrodes, thicker fat layer and deeper nerves are the best combinations for better comfort. Doheny et al. (60) used a similar approach to study the effect of fat thickness, inter-electrode distance, and electrode size in case of obese people. They showed that as the fat thickness increases, activation threshold is not affected by the variation of the electrode size and inter-electrode distance during current-controlled stimulation.

1.4 Aims and contents of the thesis

Computational models have the advantage of providing a good overview on the potential distribution, structural relations, and geometric influences that are difficult to obtain by in vivo measurements. Anatomical, electrical properties of the tissues, and stimulation factors should be carefully represented at an appropriate level to include its effect in nerve activation. However, there are no studies that investigate the effects of anatomical and electric properties of the tissues in a systematic way, clarified the level of geometric detail and which tissues should be considered or neglected, and the validation of dispersive models and its simplified version (quasi-static approximation) when non-harmonic stimulation waveforms are used as input signal.

This is why the aim of this study was to develop an electrophysiological computational model responding to TES to investigate anatomical, electrical properties, and stimulation factors of electrical stimulation for two purposes:

1. Validation and simplification of the model: easier formulation and simplified geometric for numerical and feasibility for analytical solutions.
2. Role in nerve activation: improvement of electrical stimulation: selectivity, force, and control.

We expected that by simplifying the formulation, morphology and parameters, and generating new insights in the selection of the morphologies, faster solutions for numerical and feasibility for analytical solutions could be achieved, while keeping reliability and validity. Moreover, improvement of selectivity, force, and control of electrical stimulation is expected from the study of stimulation and electric properties of the tissues, Fig. 1.3.

Model implementation and a series of simulation and experimental studies were carried out to studied the factors related to electrical stimulation:

1. Chapter 2 introduces some electro-physiological concepts related to nerve activation necessary in this work.
2. Chapter 3 explains the model implementation. First, the formulation and parameters are presented. Next, implementation of the morphology of the model is described. Finally, model analysis and validation are introduced.

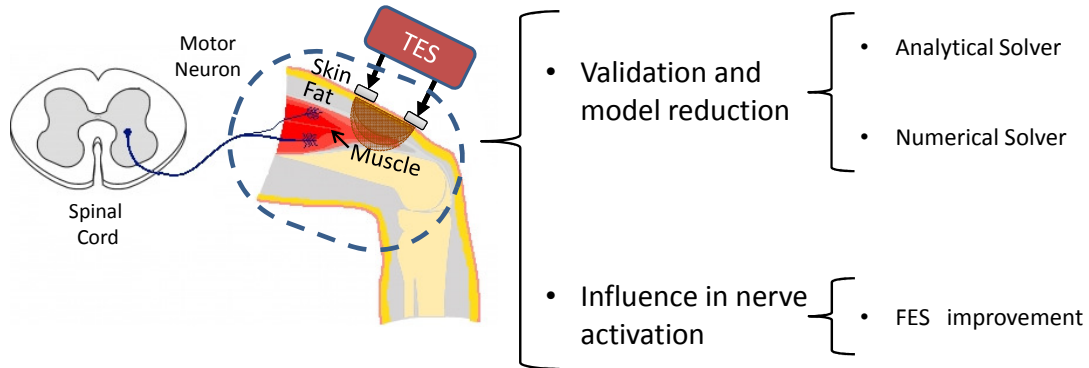


Figure 1.3: Proposed solution. Description of the elements incorporated in electro-physiological computational model.

3. Chapter 4 introduces the first experimental validation of the dispersive model using tissues-like phantom. Then, dispersive formulation is reduced to a non-dispersive formulation (quasi-static approximation) by simplifying the dispersive electric properties of the tissues by confirming the existence of an optimal frequency of the conductivity parameter, which in turn, can reduce computation time for numerical implementation and facilitate the analytical implementation.
4. Chapter 5 evaluates the limitations of different geometric representations for simulation studies. The following questions are addressed: 1) Does nerve activation differ between CM and PM? 2) How well do CM and PM approximate an AM? 3) What is the effect of the presence of blood vessels and nerve trunk on nerve activation prediction? The results showed that simplified geometries can predict the tendency of the nerve activation for studies of electrodes optimization, and their error prediction could be reduced by adjusting only the fat thickness. Also, the addition or not of blood vessels and sciatic nerve in the model depends on the stimulation location.
5. Chapter 6 treats the dominance of tissues' conductivity in the recruitment of a simplified semitendinosus muscle model. The results show that the variability of the properties of the fat and muscle are fundamental for nerve activation, contrary to skin. Also, it introduces a novel method that combines a tissue-equivalent phantom, with known and adjustable electric properties, coupled with

1. INTRODUCTION

a human thigh to systematically study the relationship between tissues and electric properties, and muscle activation showing that long pulses are better for energy transmission in current stimulation, and short pulses are better in voltage stimulation.

6. Chapter 7 confirms the role of different stimulation factors in nerve activation selectivity and penetration and new insights are obtained from the study of electrode shape.

Based on the insights acquired from the exploration of the factors related to electrical stimulation using simulation and a novel experimental studies, a framework to evaluate different parameters can be translated to different physics to evaluate the trade-off between computation cost and prediction, reliability, and validity of complex geometries and formulations, which in turn, can help in the development of a complete biophysically based computational modeling of the human.

Chapter 2

Anatomical and Electrophysiological Background

2.1 Overview

The field of study of the electrical properties of the body is known as electro-physiology. This chapter deals with the basic theory to understand and implement the computational model of the thigh responding to TES, which is explained in next chapter. The first part explains the neuron and its interaction with the muscle and the second part covers the mechanism of excitation to elicit an action potential from external stimulation.

2. ANATOMICAL AND ELECTROPHYSIOLOGICAL BACKGROUND

2.2 Neuronal and musculoskeletal interaction

This section describes the basic structure of the neuronal system (the neuron), and how it interacts with the musculoskeletal system to produce motion.

2.2.1 Neuron

Nervous system is composed of many individual cells: neurons and glia. Neuron is the main fundamental part of the nervous systems. It receives and transmits information to other cells by electrical signals. Typically, neurons have dendrites, a soma (cell body), an axon, and pre-synaptic terminals, Fig. 2.1. Dendrites are branching fibers, and its surface is lined with specialized synaptic receptors, at which the dendrite receives information from other neurons. The soma contains the nucleus, ribosome, mitochondria, and other structures found in most cells. The axons is the information sender of the neuron, conveying an impulse toward other neurons or an organ or muscle, called action potential (AP).

According to the function of the neuron, there are motor neuron and sensory neuron. The motor neuron, which originate in the central nervous system (CNS) project their axons to the skeletal muscles and directly or indirectly control muscles. It receives excitation from other neurons through its dendrites and conducts impulses along its axon to a muscle. On the other hand, sensory neurons is specialized at one end to be highly sensitive to a particular type of stimulation, such as light, sound, or touch. The motor neuron is associated with efferent neuron, or alpha motor neurons. To increase the speed of the AP, many vertebrates axons are covered with a fatty insulating material called a myelin sheath. This sheath has interruptions at regular intervals, known as nodes of Ranvier.

Action potential

Nerves and muscle cells possess a semi-permeable cellular membrane that are excitable allowing the transmission of APs. This membrane selectively regulates the chemical exchange of certain ions between the cell and its surrounding through ion channels. In the absence of any outside perturbation, the membrane of a neuron maintains an electrical potential difference between the inside and the outside of the cell. This difference in voltage in a resting neuron is called the resting potential, which is the

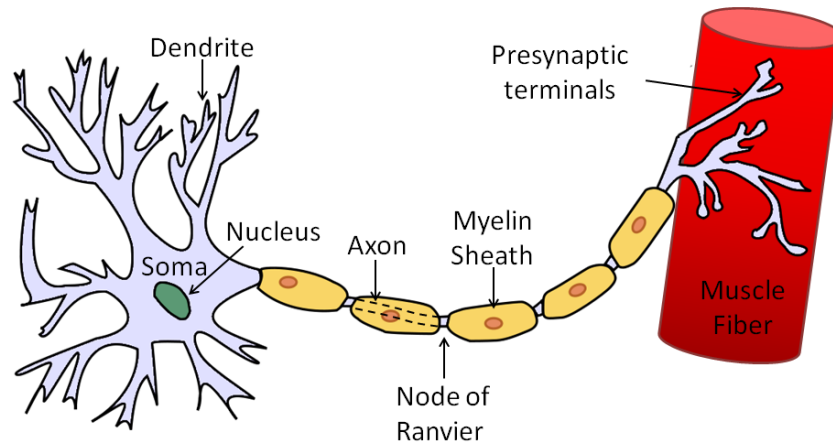


Figure 2.1: Motor neuron structure. The dendrite, soma and axon are presented. The axon is covered by a myelin sheath to increase the speed of transmission of the AP to the muscle. It was based on (89).

result of negatively charged proteins inside the cell. In most cells the resting potential has a negative value, which by convention means that the inside potential is about 70 mV lower than the outside. When an axon is depolarized above the threshold of excitation about -55mV, an AP is generated. Depolarization of the axon below this threshold does not generate an AP and the potential difference of the axon will return to the resting potential Fig. 2.2. APs are all-or-none impulses with an amplitude of about 100 mV and a duration of about 1 ms. The speed of the AP propagating along the axon can be in the range of 1 m/s to 100 m/s.

2.2.2 Skeletal muscle

Vertebrates muscles fall into three categories: smooth muscle, used primarily for internal actions; cardiac muscle, used exclusively for pumping blood; and skeletal muscle, used primarily for moving bones. Skeletal muscle is subdivided into parallel bundles of stringlike fascicles, which themselves are bundles of even smaller stringlike multinucleated cells called muscle fibers. A typical mammalian muscle fiber has a diameter of 50 μm to 100 μm and length of 2 cm to 6 cm. It is also composed of hundreds of thousands of independent contractile elements arranged in parallel and, in longer muscles, in series.

Efferent axons (α -motor neuron) leave the spinal cord through spinal-nerve ventral

2. ANATOMICAL AND ELECTROPHYSIOLOGICAL BACKGROUND

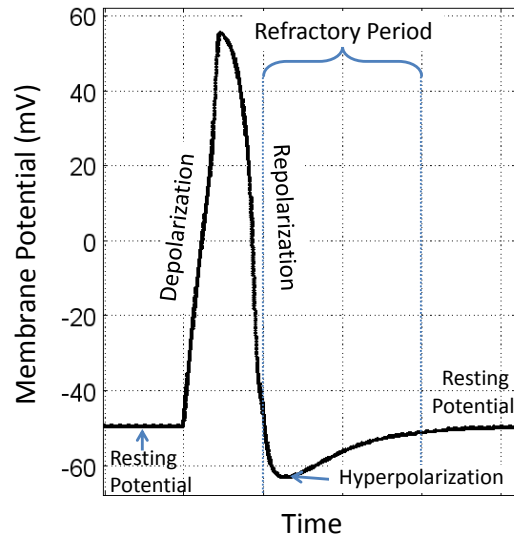


Figure 2.2: Action potential. The AP and its different phases are presented. It is obtained from the HH model (53).

roots (or through a cranial nerve from the brain stem) and projects out to muscle through peripheral nerve trunks. The myelinated nerve fiber derives from α -motor neuron and innervates, one or more, skeletal muscle fibers by a synapse called neuromuscular junction (or motor end plate). When the AP reaches its terminus at the end plate, a chemical neurotransmitter is released across the nerve/muscle gap, which causes depolarization of the muscle cells. The result is that the muscle membrane is excited, and a depolarization wave (i.e., AP), is propagated in the muscle away from the end-plate region.

Each muscle fiber is normally innervated by only one motor neuron in only one place, usually near its midpoint. Motor unit is composed of an α -motor neuron and the skeletal muscle fibers innervated by the motor neuron. Contractions of a muscle are often coordinated by groups of motor units that work together.

There are different types of motor units: slow (S) motor units, fast fatigable (FF) motor units, and fast fatigue-resistant (FR) motor units. Small α -motor neuron innervates small muscle fibers that contract slowly, generate small forces, and resist fatigue. Larger α -motor neuron innervates larger fibers that contract rapidly, generate more force, and fatigues faster. The third class of motor unit is not as fast as FF units but sustain more force and are more resistant to fatigue than FR units.

2.3 Artificial stimulation of the axon

AP of α -motor unit neurons are not only generated by given sufficient dendritic input to the its soma but also by a perturbation in the potential around the cells' membrane. This potential perturbation can trigger a sudden change in the membrane voltage, affecting adjacent portions of the membrane and evoking an AP.

An electric field that is introduced by electrodes can generate a change in the extracellular voltage around the nodes of Ranvier of myelinated fibers. This variation can depolarize the membrane voltage and evoke an AP that will propagate along the axon towards the muscle. The most excitable part of a neuron is its axon (90).

The selection of the stimulus scheme (amplitude, duration, frequency, waveform, etc.) to cause an AP depends on a number of variables: location of the electrodes (motor points), geometry of the tissues, and its electrical characteristics, which are investigated in subsequent sections. Some parameters that influence the effect of the stimulation are discussed bellow.

The most often applied waveforms are rectangular and sine. These waveforms have a certain pulse amplitude, pulse duration, rise time, and pulse repetition frequency. In order to reverse the modified charge distribution after the pulse a balancing pulse can be applied, which is a bipolar waveform. The applied pulse influences the potential difference of axons. An increase of the pulse repetition frequency does not recruit more axons but increases the frequency of AP in the activated axons; thus, increase of generated force.

Cathode electrode and anode are the negative and positive reference of the applied stimulation, respectively. The axon is depolarized under the cathode and hyperpolarized under the anode electrode. If the depolarization is large enough to drive the membrane potential above about -55 mV, an AP is generated. The hyperpolarization under the anode drives the membrane potential to lower values (70 mV) and suppresses the generation of AP. However, when the stimulation current is switched off the potential difference returns to its resting membrane potential of about -70 mV. Generally, stimulation with anodic currents (positive) needs stronger signal (91)

Motor point is the stimulation location on the skin surface where the muscle is activated at the minimum possible amplitude of the stimulation because the corresponding region is close to a major concentration of motor end-plates. The stimulation at this

2. ANATOMICAL AND ELECTROPHYSIOLOGICAL BACKGROUND

point makes more selective the activation of specific nerves and muscles. In clinical practice, the cathode is placed on the motor points. However, the motor point is dependent on anatomical properties of the underlying muscle; therefore, the location of a motor point will shift during a shortening or lengthening of a muscle contraction. In addition, the low selectivity of surface electrode does not contribute in a focal stimulation to have a fix motor point location.

2.4 Dielectric properties of the human tissues

Tissue is a very inhomogeneous material because the cells are of uneven size and with very difference functions. Also, from an electrical point of view, tissue cannot be regarded strictly as a homogeneous material. Therefore, the electrical conductivities of different biological tissues constitutes a variable influence to the electric potential distribution. An useful presumption is that tissues are anisotropic; however, isotropic conductivities should be considered too. Moreover, due to the capacitance of cell membranes the conductivity of biological tissues varies with the frequency content of the electric signal (92, 93, 94, 95).

As the fat layer has a high resistance and is between two high capacitance layers (skin and muscle), a capacitance is developed. Therefore, fat layer behaves as a filter that alters the waveform arriving to the muscle (70). In the case of the muscle layer, it consists of well defined long fibers, which results in notable differences between transversal and longitudinal conductivities. The longitudinal conductivity is lower than the transversal conductivity.

Chapter 3

Implementation of the Bioelectrical Based Computational Model

3.1 Overview

This chapter explains how the computational model of the thigh was implemented. The computational model is based on an two-step method, Fig. 3.1. The first step comprehends a finite element model to calculate the potential distribution within the tissues produced by the external stimulation; it involves two tasks:

- Modeling: formulation of the partial differential equation (PDE) for the computation of the potential distribution, $V_e(x, y, z)$. One part is to determine the material properties for various tissue types (hence PDEs), and the other part focuses on defining the geometry of organs (i.e., the boundary of the PDE's domain).
- Solving the PDE: requires a discretization method, such as FEM. After FEM discretization, the object's configuration (shape) is described entirely by a finite number of nodal points.

The second step calculates the occurrence and propagation of an AP along the nerve. It employs a mammal nerve model (CRRSS) to obtain the AP due to potential distribution, calculated in the first step. The advantages of this approach is that it provides a good overview on the potential distribution, structural relations, and geometric effects that are difficult to obtain by in vivo measurements.

3. IMPLEMENTATION OF THE BIOELECTRICAL BASED COMPUTATIONAL MODEL

To solve these equations, a FE model is implemented. Finally, the quantification indexes to compare between different stimulation schemes and validate with experimental data are introduced (activation volume, activation depth, and selectivity).

Finally, the fabrication and measurement of the dielectric properties of tissue-equivalent phantom are introduced. They offer the possibility to adjust their dielectric properties to systematically study their effects in muscle contraction by implementing a human-phantom coupling experiment. The work presented here was published in (13, 42, 96, 97).

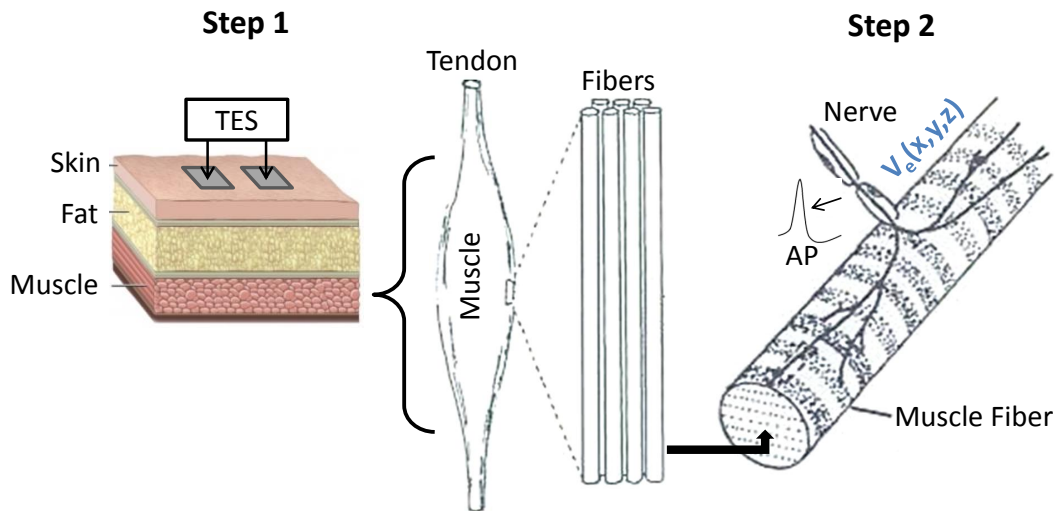


Figure 3.1: Two-step solution for nerve activation. Step 1 calculates the potential distribution within the tissues, $V_e(x, y, z)$, produced by the external stimulation. Step 2 calculates the occurrence and propagation of an AP along the nerve.

3.2 Model

A two-step method was implemented to calculate activation in the muscle (57). In the first step, the voltage within the tissues, $V_e(\text{V})$, could be computed according to a dispersive model to account for the dispersive dielectric properties of the tissues when a non-harmonic waveform is employed as stimulation or the quasi-static approximation, which requires certain conditions that are introduced below. The second step was to obtain the voltage at each point of the nerve to calculate its motor threshold (MT). A detailed model of the nerve can be used to obtain the temporal-spatial behavior of the AP.

3.2.1 First step: voltage distribution

Governing equation

The potential distribution obeys equations the Laplace equations 3.1 and 3.2 for time-domain and frequency-domain, respectively

$$\nabla \cdot \left[\left(\sigma + \epsilon_0 \epsilon_r \frac{\partial}{\partial t} \right) \nabla V_e \right] = 0 \quad (3.1)$$

$$\nabla \cdot [\sigma(\omega) + j\omega\epsilon_0\epsilon_r(\omega)] \nabla V_e = 0 \quad (3.2)$$

where ω denotes the angular frequency (rad/s), the dispersive conductivity σ (s/m), and ϵ_r the dispersive relative permittivity, j the imaginary unit, $\nabla \cdot$ and ∇ denote the divergence of a vector function and the gradient of a scalar function, respectively. It is possible to view equation 3.2 as the Fourier transform of equation 3.1.

If the governing equation is used in time-domain, boundary conditions of the stationary current field problem in the frequency-domain are expressed as sine functions. Considering that the electrical properties of the considered biological tissues are dispersive. Then, if a non-harmonic stimuli is employed, a Fourier transform of the stimuli and the consideration of a large number of harmonics (and the corresponding solution of the stationary current field problem) is required to obtain the time-dependent voltage distribution within the tissues. If the governing equation is used in time-domain,

3. IMPLEMENTATION OF THE BIOELECTRICAL BASED COMPUTATIONAL MODEL

the remaining issue would be the dispersive electrical properties of the considered biological tissue types, which would require a transformation of the conductivity from frequency-domain into time-domain.

We used the Fourier transform approach. First, definition of the applied stimulus in time domain (square wave stimulus current) in Fig. 3.2a. Next, discrete Fourier transform is used to convert the stimulation waveform from time-domain to frequency-domain to obtain its amplitude and phase, $Input(\omega)$ in Fig. 3.2b. Third, equation 3.1 is computed at each frequency component with a normal current density crossing the surface of the electrode at 1 A/m^2 for current stimulation and 1 V for voltage stimulation to obtain the transfer function $H(\sigma(\omega), \epsilon(\omega), x_0, y_0, z_0)$ in Fig. 3.2c. Fourth, $V(\omega, x_0, y_0, z_0)$ was obtained by multiplying $Input(\omega)$ and $H(\sigma(\omega), \epsilon(\omega), x_0, y_0, z_0)$. Finally, the resulting waveform is converted back to time-domain, $V(t, x_0, y_0, z_0)$ in Fig. 3.2d, as explained in (78, 80).

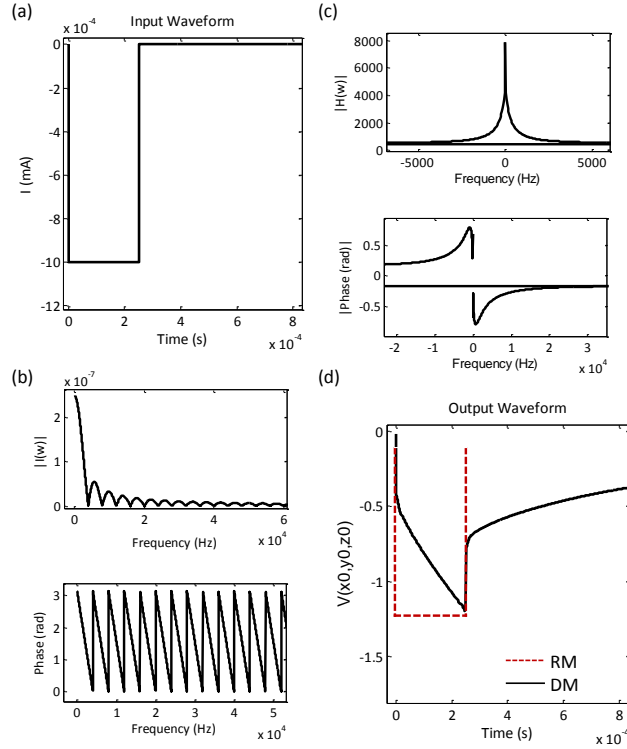


Figure 3.2: Solution steps of the dispersive model. (a) $Input(t)$, (b) $Input(\omega)$, (c) $H(\sigma(\omega), \epsilon(\omega), x_0, y_0, z_0)$, (d) $V(t, x_0, y_0, z_0)$. In this case, the transfer function is the impedance of the system as the input waveform is a current signal.

Quasistatic-approximation

$V_e(V)$ was computed according to the non-dispersive resistive model (quasi-static approximation) 3.3:

$$\nabla \cdot [\sigma(f_c) \nabla V_e] = 0 \quad (3.3)$$

where f_c is the frequency used to calculate the conductivity σ (s/m). The conditions required are the following:

$$kR_{max} \ll 1 \quad (3.4)$$

Capacitance effects

$$\frac{\omega\epsilon}{\sigma} \ll 1 \quad (3.5)$$

Inductive effects

$$(kR_{max})^2 \ll 1 \quad (3.6)$$

Leakage to outside air

$$\frac{\omega\epsilon_0}{\sigma_n} \ll 1 \quad (3.7)$$

$$k^2 = \omega^2 \mu \epsilon \left(1 + \frac{\sigma}{j\omega\epsilon} \right) \quad (3.8)$$

where R_{max} is the maximum length corresponding to the overall dimension, ϵ and σ are the permittivity and conductivity of tissue, and ϵ_0 is the permittivity of free space.

Although the stimulation waveform is not harmonic (square pulse), the dispersive nature of the conductivity and permittivity of the biological tissue is omitted to improve computation time. This is because that the quasi-static approximation can be used to approximate a dispersive model considering an appropriate value of conductivity (77, 78). We confirmed that the appropriate conductivity that approximates the dispersive model for our simulation models' geometry is f_c equal to 2 kHz. The Dirichlet and von Neuman boundaries were imposed to control current values at the electrode surface to confine current flow within the model. The outer region (air) is not included as a specification of the problem (77, 98).

3. IMPLEMENTATION OF THE BIOELECTRICAL BASED COMPUTATIONAL MODEL

Model implementation for potential computation

A discretization method is required for solving the PDEs equations, such as Finite Element Method (FEM). After FEM discretization, the object's configuration (shape) is described entirely by a finite number of nodal points. The advantages of FEM models are: 1) coping with detailed geometries, 2) analysis can be done both in the frequency domain and the time domain, 3) modeling of anisotropic materials, 4) Maxwell's equations can be used, 5) visualization of the whole electric potential field distribution. However, there is a trade-off in computational cost for detailed FEM models.

The model was constructed, discretized, and solved using COMSOL Multiphysics 4.4. The models were discretized into an average of 704×10^3 tetrahedral elements for parallel models (PM) and 1.7×10^6 for anatomical and cylindrical models (AM, CM, respectively). As result, an average of 986×10^3 and 2.2×10^6 degrees of freedom were computed in the system matrix for PMs and the rest of the models, respectively. The quasi-static model was solved using an iterative linear solver (conjugate gradients) at each point within the tissues domain to determine the potential distribution; it took 200 s for the AMs to be solved using a quad-core INTEL Core i7 -960 processor at 3.2 GHz and 24.0 GB of RAM memory. The PMs were three times faster than CMs, which were three times faster than AMs.

3.2.2 Dielectric parameters of the tissues

The dielectric properties of the tissues are strongly related to the frequency and are subject to variation due to physiological conditions such as water content of the tissue. Gabriel et al. (92, 99, 100) provided a reliable database for several tissues. The sources of the materials were excised animal tissue, human autopsy materials, and human skin and tongue in vivo. The model of the frequency dependence of the dielectric properties was obtained by 4-Cole-Cole (equation 3.9) to include main dispersions. The results obtained by the model is shown in Fig. 3.3 that are implemented in the model using frequency as a input parameter.

$$\varepsilon^* = \varepsilon_r - \frac{j\sigma}{\omega\varepsilon_0} = \varepsilon_\infty + \sum_{m=1}^4 \frac{\Delta\varepsilon_m}{1 + (j\omega\tau_m)^{1-\alpha_m}} + \frac{\sigma_i}{j\omega\varepsilon_0}, \Delta\varepsilon_m = \varepsilon_{s,m} - \varepsilon_{\infty,m} \quad (3.9)$$

where ε^* is the complex relative permittivity, ω the angular frequency, ε_s for static values, and ε_∞ for frequency tending to infinity.

The tissues are considered isotropic except for the muscle. The conductivity of the muscle was described by the diagonal tensor, where σ_{ij} describes the flow in the i -direction due to an applied field on the j -direction in equation 3.10.

$$\sigma = \begin{pmatrix} \sigma_{l(\omega)} & 0 & 0 \\ 0 & \sigma_{t(\omega)} & 0 \\ 0 & 0 & \sigma_{t(\omega)} \end{pmatrix} \quad (3.10)$$

3.2.3 Second step: nerve activation

A compartment model for the nerve was used to explain the influences of externally applied electric fields in target neurons. The analysis of compartment models helps to explain the influences of applied electric or magnetic fields in representative target neurons.

McNeal (57) developed a compartment model for a myelinated nerve fiber and its sub-threshold response to external point source stimulation. He represented the myelinated nerve using an equivalent circuit of the node of Ranvier and assumed that the myelin sheath was a perfect insulator. The Chiu-Ritchie-Rogart-Stagg-Swenney (CRRSS) model (55, 56) was used to calculate the ionic current on the node of Ranvier and described the nonlinear gating of ion channels across the unmyelinated neuronal membrane. The internodes were assumed to be a passive membrane (constant membrane conductance).

Activation threshold or MT is the lowest stimulation intensity necessary to propagate an AP for a given nerve. An AP was considered elicited when the trans-membrane potential exceeded a threshold of 80 mV. The current stimulation amplitude was modified by using a binary search algorithm to find the activation threshold until the error was lower than 10 μ A. We confirmed convergence of the activation threshold solution by increasing the number of degrees of freedom twice for each iteration. The iterations stop until the error of the activation error was lower than 0.1% with a minimum of four times starting from 2×10^5 degrees of freedom.

3. IMPLEMENTATION OF THE BIOELECTRICAL BASED COMPUTATIONAL MODEL

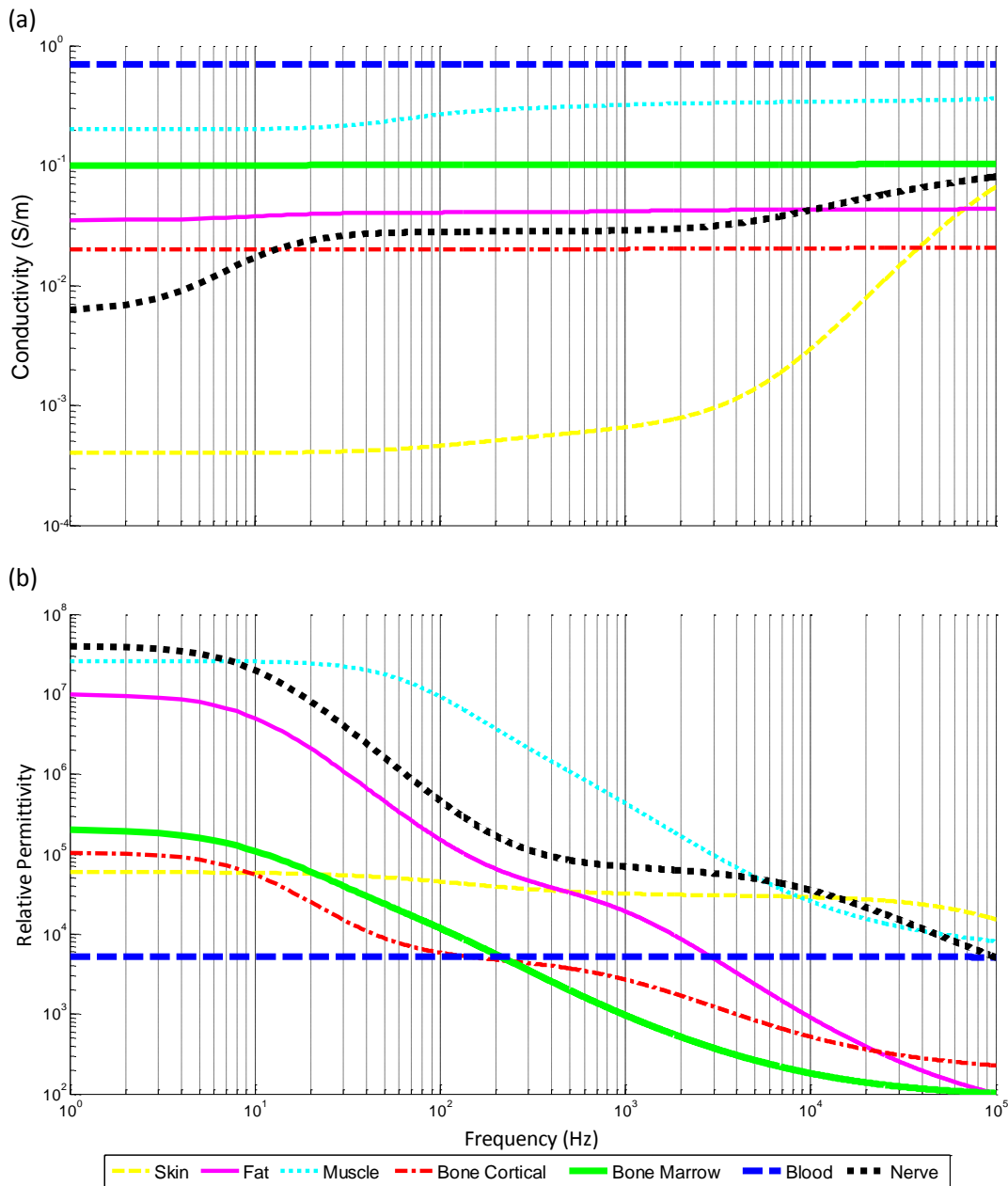


Figure 3.3: Dispersion of the tissues employed in the models calculated by 4-Cole-Cole equation. (a) Dispersive conductivity and (b) relative permittivity.

Compartment model of the nerve

The compartment model of the nerve is shown in Fig. 3.4 (42). The membrane voltage v_n of equation 3.11 is obtained by applying Kirchoff's current law at each node (90). (Appendix A presents the detail of the derivation of the equations.)

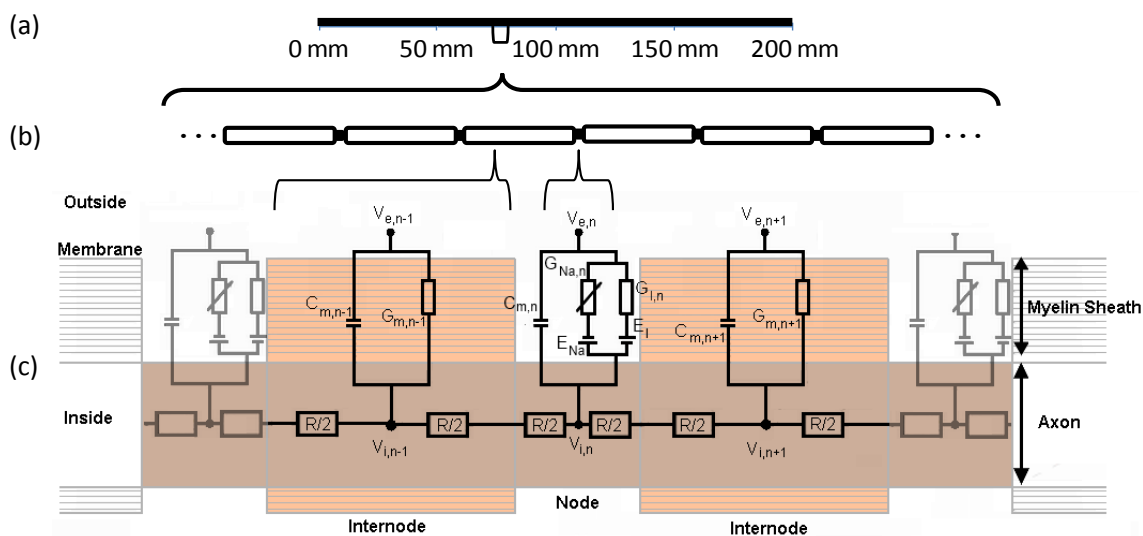


Figure 3.4: Compartment model of the myelinated fiber. (a) Axon of 20 cm of length, (b) it is composed of 124 nodes and internodes, (c) nodes are modeled as active membranes (CRRSS model), and internodes are represented by single compartments with constant membrane conductance.

$$c_m \frac{\partial v_n}{\partial t} = -I_{ion,n} + \frac{v_{n-1} - 2v_n + v_{n+1}}{R} + \frac{v_{e,n-1} - 2v_{e,n} + v_{e,n+1}}{R} \quad (3.11)$$

where c_m is the membrane capacitance, $I_{ion,n}$ the ion current, R the intra-axonal resistance between the centers of two adjacent compartments, and v_e is obtained from first step.

It is necessary to compute $I_{ion,n}$ to solve the membrane voltage. In the case of the internodes, they are considered as passive membranes and are assumed to have a constant membrane conductance $G_{m,n}$. In contrast, the nodes of Ranvier present non-linear activity; therefore, additional differential equations are included (membrane model).

3. IMPLEMENTATION OF THE BIOELECTRICAL BASED COMPUTATIONAL MODEL

Membrane model

The ionic membrane current of the internode can be formulated with equation 3.12, which is a linear relationship. Variables $C_{m,n}$ and $G_{m,n}$ can be approximated with the values assumed for the specific capacity c_m and the conductivity g_m , and the number N of layers of myelin wrapped around the internodal cylinders with diameter d and length l_n , equations 3.13 and 3.14.

$$I_{ion,n} = G_{m,n}V_n \quad (3.12)$$

$$C_{m,n} = c_{m,n}d\pi l_n/N \quad (3.13)$$

$$G_{m,n} = g_{m,n}d\pi l_n/N \quad (3.14)$$

In the case of non-linear activity of the membrane, the first model (HH model) was developed by Hodgkin and Huxley (53). They formulated and experimentally validated a mathematical model of the voltage gated ion channels that describes that neural signals propagates as membrane voltage along a nerve fiber (axon) based on the intracellular and extracellular ionic concentrations. The model was obtained from a non-myelinated squid axon using a space clamp experiment (stimulation without propagation). A subsequent models was FH model (Frankenhaeuser-Huxley) (54) which was the first myelinated fiber model on the frog axon node. The potassium current was found to be very important in the HH model and to a lesser degree in FH model in contrast to mammalian nerves.

CRRSS model (55, 56) is used to describe the nonlinear gating mechanism of ion channels across the unmyelinated neuronal membrane to calculated $I_{ion,n}$ in a rabbit node of Ranvier. It incorporates sodium and leakage currents but omits voltage-dependent potassium currents as it was found to be almost absent in the excitation process of myelinated fibers in the sciatic nerve of the rabbits. Thus, sodium current is responsible for the initial fast depolarization, and leak current is entirely responsible for the repolarization during the AP. The parameters of the model are listed in Table A.1 in the Appendix A.

$$I_{ion,n} = G_{Na,n}m^2h(V_n - E_{Na}) + G_{l,n}(V_n - E_l) \quad (3.15)$$

$$G_{Na,n} = g_{Na}d_n\pi l_n \quad (3.16)$$

$$G_{l,n} = g_l d_n \pi l_n \quad (3.17)$$

where E_{Na} and E_l are the sodium and the leakage equilibrium potentials caused by different ionic concentrations at the inside and outside of the fiber. $G_{Na,n}$ and $G_{l,n}$ are the sodium channel and leakage channel conductance, g_{Na} and g_l are the maximum conductivities per square unit area. m and h are probabilities of the gating of the sodium channel that reduce its maximum conductance (equations are presented in Appendix A).

The activation process of the channels and resulting current for the AP generation is shown in Fig. 3.5.

Other mammalian nerves have been developed: 1) SE model (Schwarz-Eikhof) (101) is a FH type from voltage clamp experiments on the rat nodes with a similar ionic currents as the CRRSS models. 2) SRB model (Schwarz-Reid-Bostock) (102) is derived from human nerve fibers where slow and fast potassium currents have little effect in the repolarization of the AP. However, omission of slow potassium current might induce an increase and sustain a repetitive firing and response during long stimulus. Also, it should be considered for axonal signaling at the internode or block conduction mechanism (103). CRRSS model suffices for the experiments in this work. Appendix A presents a more detail comparison of the nerve models.

Activation function

The activation function explains the principle of external stimulation without formulating the ion-channel dynamics (91) and is a term used for driving function for external potential (equation 3.18, see Appendix A). It explains that 1) cathodic currents generates nerve activity easier than anodic currents with small extracellular electrodes, 2) thick fibers are easier to activate, 3) activation threshold is influenced by the curvature of a target fiber (104).

$$f_n = \frac{d}{4\rho_i c_m} \frac{v_{e,n-1} - 2v_{e,n} + v_{e,n+1}}{\Delta x_n^2} \quad (3.18)$$

where a positive activating function presents the possibility of spike initiation, and a negative activating function produces hyperpolarization.

In the case of a long homogeneous fiber, the activating function (AF) is proportional to the second derivative of the extracellular potential (omitting the endings of the fiber).

3. IMPLEMENTATION OF THE BIOELECTRICAL BASED COMPUTATIONAL MODEL

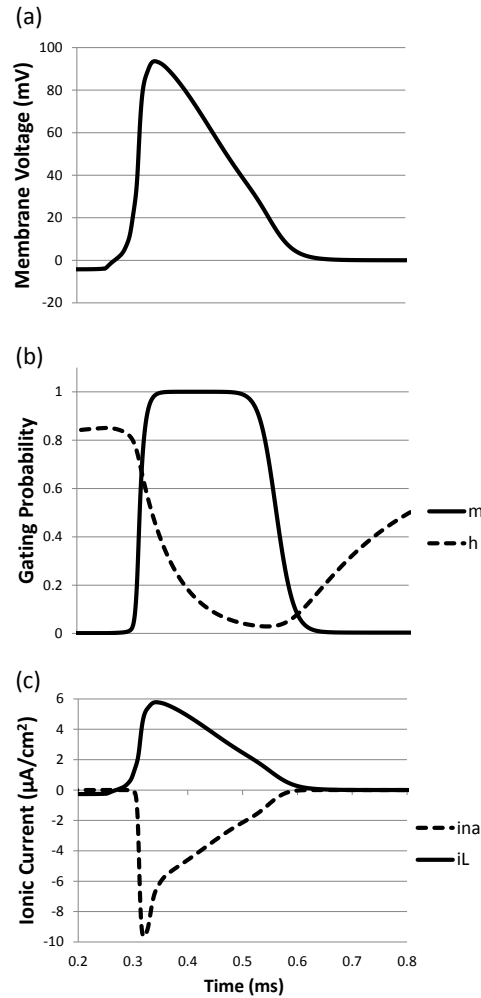


Figure 3.5: Dynamics of the CRRSS model for a given node of Ranvier. (a) AP, (b) gating process probabilities for the sodium channels: m is activation probability and h is inactivation probability, (c) resulting sodium current i_{na} and leakage current i_L , which cause depolarization and repolarization, respectively.

$$f_n = \frac{d}{4\rho_i c_m} \frac{\partial^2 V_e}{\partial x^2} \quad (3.19)$$

In summary, the two-step method is presented in Fig. 3.6.

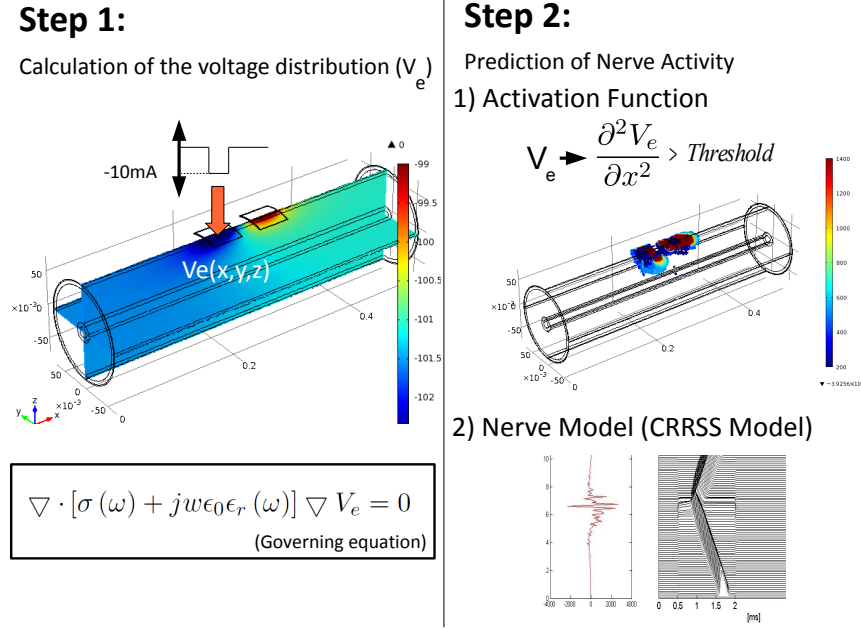


Figure 3.6: Two-step method summary. The equation to solve step 1 is a derivation of the Maxwell's equations. The step 2 is obtained from activation function or nerve model.

3.3 Geometry

The Anatomical models (AM) of the thigh was constructed by segmenting the MRI data sets using our pulse-coupled neural network segmentation and bottom-up saliency method (105), region competition and edge in ITK-SNAP (Insight ToolKit-SNake Automatic Partitioning is an open source image segmentation software, www.itk-snap.org), which also reconstructed the 3D tissues. MeshLab (open source geometry processing software, <http://meshlab.sourceforge.net>) was used to smoothed the 3D tissues. Finally, they were opened with SolidWorks (Dassault Systmes, Vlizy, France) and imported into COMSOL Multiphysics using the LiveLink module as shown in Fig. 3.7.

The average transverse area of each tissue of the AMs and average data found in literature (106) were used to set the tissues' thickness used in the cylindrical and parallel models, Fig. 3.8. The length of the model was chosen to neglect the effect of the borders and avoid errors that would be introduced in the simulation. In addition, the external corners of the electrodes are rounded to reduce singularities in the solution and the thickness of the interface electrode-skin is 1 mm (hydrogel). Single square and circular electrodes with different areas were investigated. Moreover, the inter-electrode

3. IMPLEMENTATION OF THE BIOELECTRICAL BASED COMPUTATIONAL MODEL

distance was varied to study its effect in the stimulation.

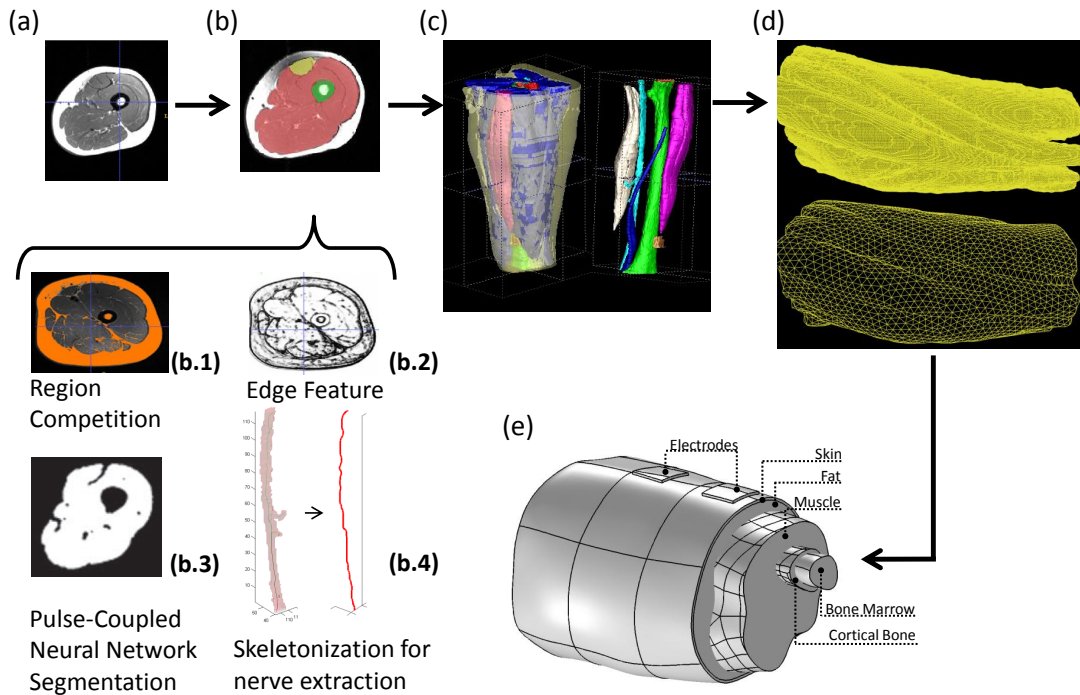


Figure 3.7: Geometry extraction process. (a) Original data, (b) segmented data, (c) 3D reconstruction, (d) smoothed tissues for numerical stability, (e) resulted geometry for simulation.

3.3.1 Semitendinosus muscle

The selection of the muscle to study its recruitment was chosen based on two criteria: innervation location and geometry of the end-plate zone. First, muscle activation may be initiated near the endplates, far from the endplates, at combination of both, or directly in the muscle fibers in the case of an innervated muscle. For this study, the case of muscle activity initiated at the nerve axons near the endplates was implemented to simplify the model by avoiding the time-partial activation from distal points of innervating nerves; thus, the muscle under study should be superficial and innervated on its deep or lateral surface. Three muscles met these requirements in the thigh: the rectus femoris, biceps femoris long head, and semitendinosus muscle (ST) (107, 108). Second, endplates zone geometry depends on the configuration of the muscle fibers (109). ST muscle was selected because of the straightforward shape of its endplate

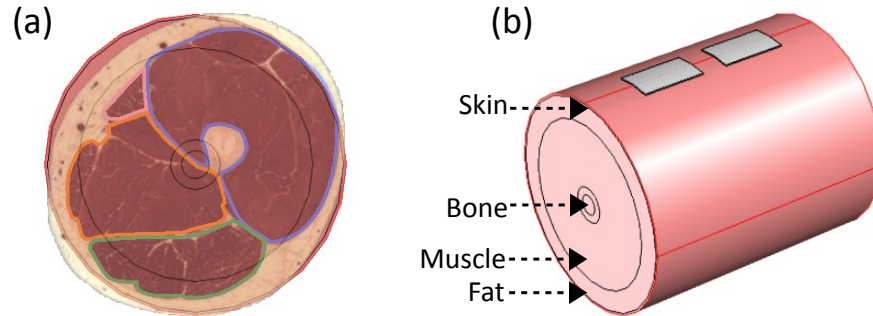


Figure 3.8: Cylindrical simplification of the thigh. (a) Average thigh approximation, (b) cylindrical representation.

zone (band) and the motor entry point (MEP) location corresponded to the zone of the endplates. Finally, for simplification only one MEP at the middle of the muscle was considered in the present study; however, the ST muscle has two MEPs. A simplified geometry of the ST muscle was implemented based on experimental average values of the muscle length and cross-section area at the MEP (107, 110) as shown in Fig. 3.9 (13), and a bimodal distribution of the nerve axon diameters with peaks at $6\ \mu\text{m}$ and $12\ \mu\text{m}$ was obtained from a morphometry study of the sciatic nerve (108), Fig. 3.10 (96). The minimum and maximum nerve axon diameter were $3\ \mu\text{m}$ and $17\ \mu\text{m}$, respectively. This distribution was used in the model, except that the gamma efferent and secondary afferent fibers were excluded, (84) resulting in a final distribution range from $7\ \mu\text{m}$ to $17\ \mu\text{m}$. The nerve axons near the vicinity of the endplate band were located randomly and parallel with each other at different depths within the muscle as shown in Fig. 3.11 (13). Because the model is symmetric, the recruitment was computed for only half of the ST muscle seeded with nerves that innervate the endplates. The recruitment of another half could be mirrored. The length of the nerve axons ($6.30\ \text{cm}$) was limited by the band that corresponds to the endplates zone (107).

The feasibility of the proposed model of the nerve activation in the vicinity of the endplates was carried out by simulating recruitment-duration curves, Fig. 3.12 (13). The recruitment percentage refers to the percentage of activated fibers out of the total population. A plateau was observed after $0.3\ \text{ms}$ and nerve population composed of more than 500 fibers converged to the same solution. A duration time of $0.5\ \text{ms}$ was chosen for the subsequent simulations. These results agreed with the recruitment curves (76).

3. IMPLEMENTATION OF THE BIOELECTRICAL BASED COMPUTATIONAL MODEL

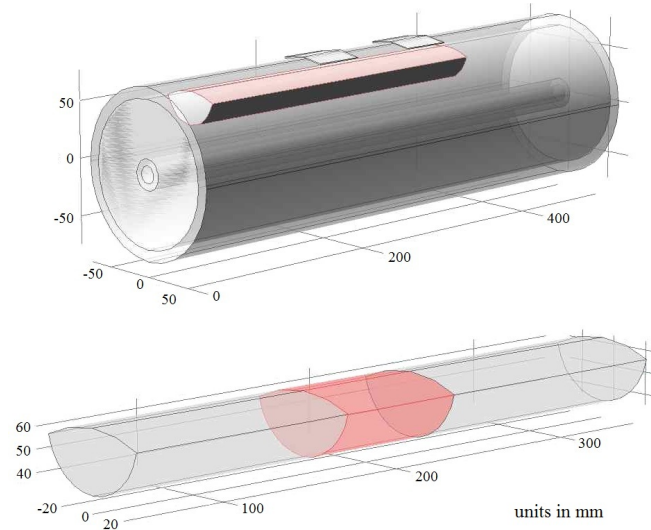


Figure 3.9: A simplified geometry of the semitendinosus muscle was embedded in the muscle layer. It had a cross-section area of 9.50 cm^2 and length of 30.10 cm . The cathodic electrode was centered above the end-plate zone (highlighted). Units are in mm.

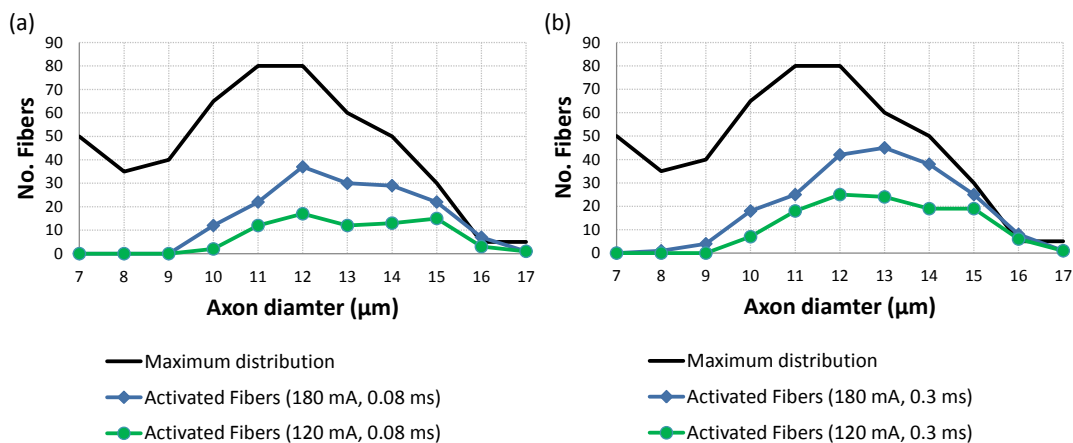


Figure 3.10: Diameter distribution of the motor nerve axons in the sciatic nerve. Activation of the nerve axons at different pulse durations and stimulation amplitudes (a) 0.08 ms and (b) 0.3 ms . Thin fibers are difficult to activate in our simulation model.

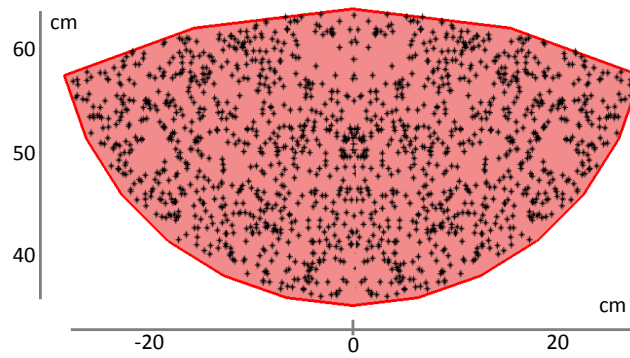


Figure 3.11: Endplates band. Frontal view of the random distribution of the myelinated motor axon nerves innervating the endplates band (750 axons).

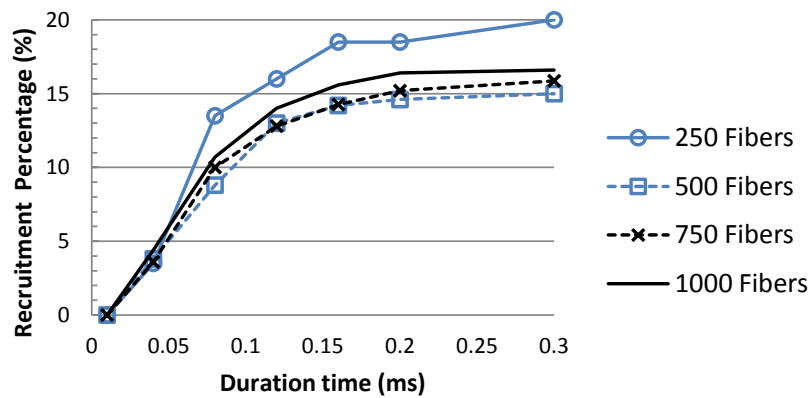


Figure 3.12: Recruitment-duration curve for 4 nerve axon populations (250, 500, 750, and 1000) in the vicinity of the endplates of the ST muscle for a cathodic stimulation of 120 mA.

3. IMPLEMENTATION OF THE BIOELECTRICAL BASED COMPUTATIONAL MODEL

3.4 Model analysis

The evaluation methods to investigate the effect of different TES parameters in the nerve activation are activation volume (AV), activation depth (AD), selectivity and MT.

The AV is defined as the region inside the muscle where AP may occur (111). It is useful to study how much portion could be activated using high intensity stimulation, where selectivity is not the main concern. The AV is limited by the AF over a threshold and the boundaries of the muscle domain, as shown in Fig. 3.13 (42). The threshold value for activation depends on the fiber diameter and stimulation pulse duration (112). The calculation of volume of the activation volume is called, in this work, VAV.

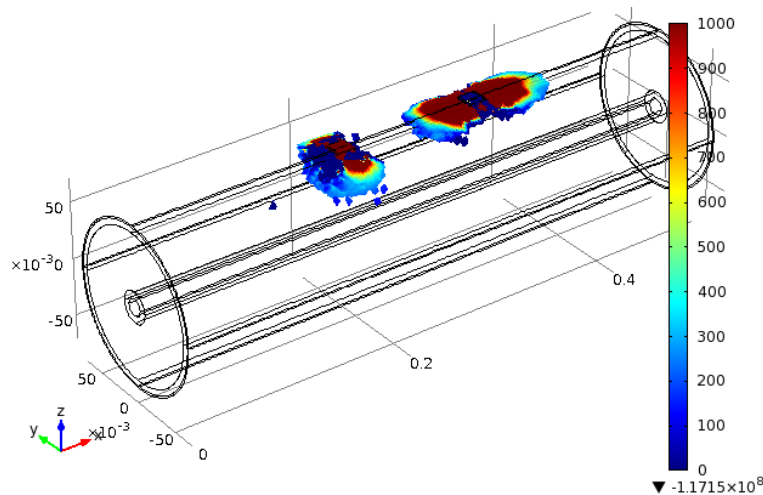


Figure 3.13: Activation volume in the CM. The AV in the CM of the skin, fat, muscle and bone layers using two superficial electrodes of area of 2.25 cm^2 located with an inter-electrodes distance of 11 cm. The magnitude of the stimulation current is 20 mA. The AV region is limited by the AF and within the boundaries of the muscle domain.

AD is the distance between a point at the fat-muscle interface and the farther point to activate a fiber with a specific diameter. Both points are in a line normal to the center of the stimulation electrode, Fig. 3.14. The AD is an index of the penetration within the muscle (without considering fat thickness), and calculated for a specific fiber using the AF (41).

The selectivity of muscles indicates how focal is the activation, i.e., nerve activity without excitation of the surroundings (41). It considers the deeper penetration (AD)

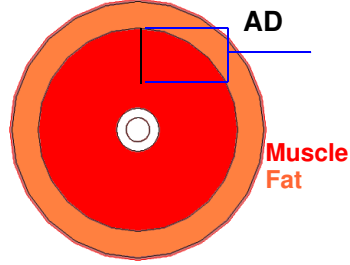


Figure 3.14: Activation depth. AD is the distance between a point at the fat-muscle interface and the farther point where a fiber with a specific diameter may be activated.

and the narrower volume under the electrode. The estimation of the narrower volume was done by calculating the inverse of the average of the transversal area of the volume, which is the quotient of VAV and AD. The resulting expression is equation 3.20

$$Selectivity = \frac{AD}{\frac{V_{AV}}{AD}} = \frac{AD^2}{V_{AV}} \quad (3.20)$$

In Fig. 3.15, two different AVs are presented to compare selectivity. Figure 3.15a presents a better selectivity because its AV is more focal. The effect of the TES parameters in the selectivity is a subject of study in next chapters.

MT is the nerve activation at the lowest stimulation intensity. One myelinated fiber is placed under the electrode to investigate its MT. The cathodic stimulation current was increased until the transmembrane potential exceeded a threshold of 80 mV, i.e., and a AP propagation is elicited using the CRRSS model, Fig. 3.16. The convergence was verified for MT calculation, as shown in Fig. 3.17.

For instance, Fig. 3.18a shows that voltage at a fixed input current followed the expected results for different pulse duration. Figure 3.18b shows that AP generation needed larger voltage at short pulses and smaller voltage until saturation at larger pulse durations, as expected from strength-duration curve studies (37, 38).

3.5 Phantom experiments

3.5.1 Phantom materials

The tissue-equivalent phantom has a relative dielectric constant and conductivity similar to biological tissues, primarily in the study of the effect of electromagnetic field for

3. IMPLEMENTATION OF THE BIOELECTRICAL BASED COMPUTATIONAL MODEL

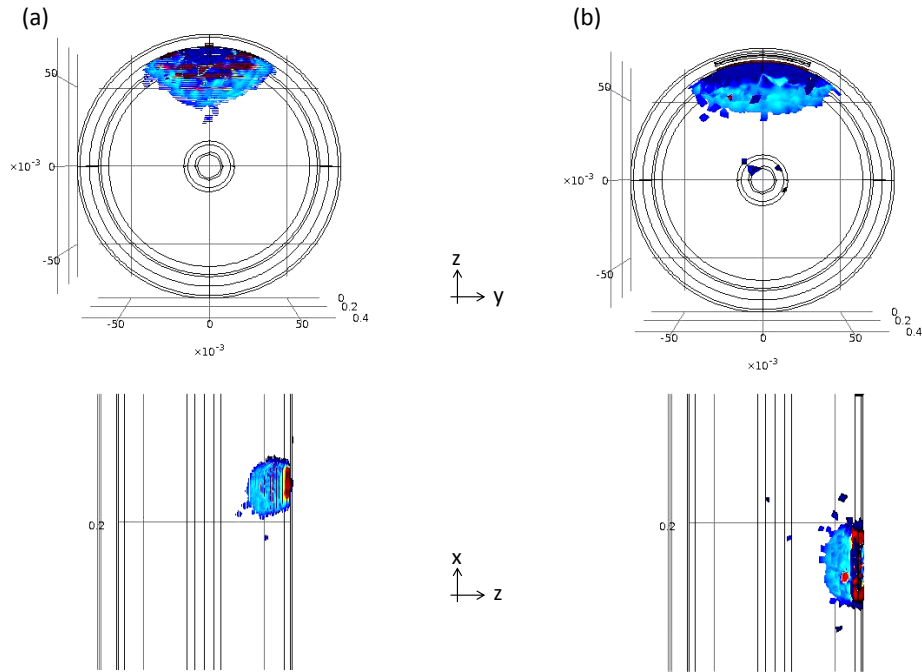


Figure 3.15: Example of the selectivity of two different TES configurations. (a) Selectivity is 30.15 and (b) selectivity is 10.15.

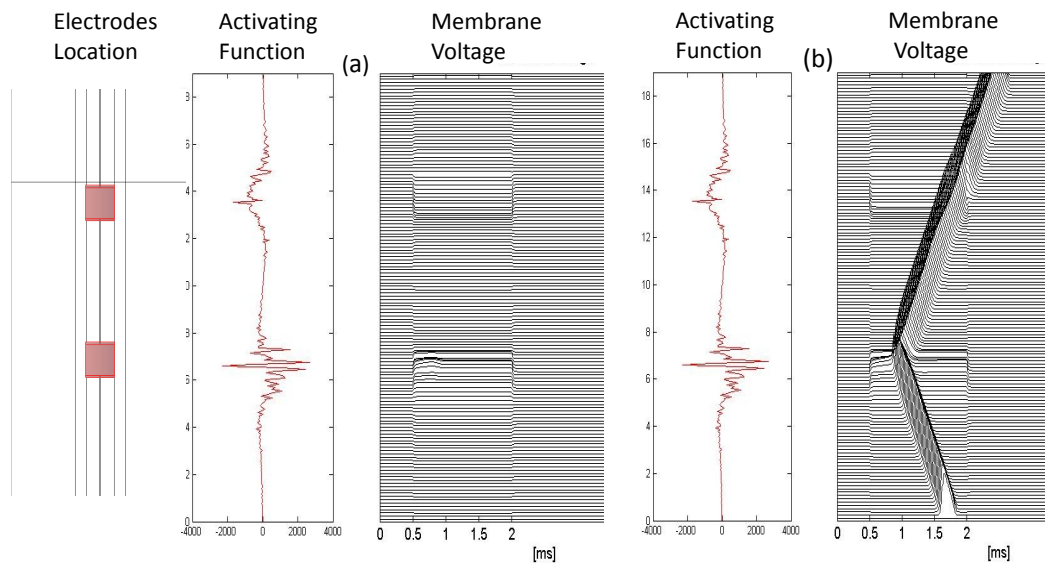


Figure 3.16: Example of MT before and afterwards an action potential is elicited. (a) Subthreshold stimulation using an intensity of 8.81 mA, (b) AP along the nerve fiber using a stimulation intensity of 8.82 mA.

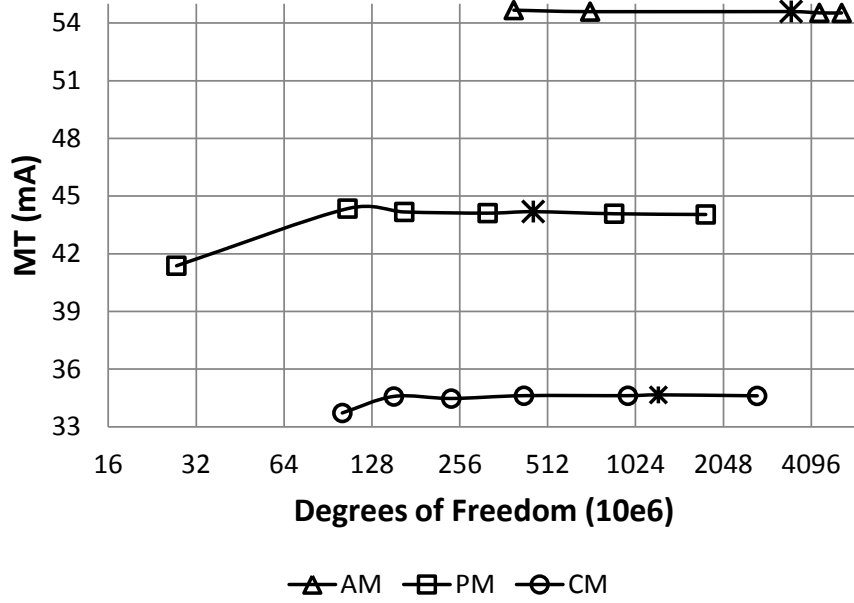


Figure 3.17: Convergence of the MT solution for different volume conductor geometries. PM and CM use symmetry property along the geometry. Also, PM needs less DOF than CM. The asterisk points correspond to the selected discretization for each model.

high-frequencies (113, 114, 115). However, they have not been used and at low-mid-frequencies (kHz) for studies of electrical stimulation.

A muscle-equivalent phantom and a customized fat-equivalent phantom to match low-mid-frequency were fabricated, Table 3.1, based on (116). The muscle equivalent phantom consists of deionized water, agar, sodium dehydroacetate, and sodium chloride and the fat equivalent phantom of deionized water, glycerine, polyethylene powder, agar, and sodium chloride. The deionized water was used as a base for the muscle as it has a high water content which is reflected in its high permittivity. The deionized percentage was reduced for the fat as it has a lower relative permittivity because of its low water content. The agar was added for maintaining the shape of the phantoms. The relative permittivity was dependent on the concentration of the glycerol, and conductivity was dependent on the concentration of the sodium chloride. In addition, the polyethylene powder controlled the relative permittivity and conductivity and helped to keep the phantom dry for the human-phantom coupling experiments. Finally, three different conductivity dispersions were defined for the fat-equivalent phantom: σ_L , σ_M ,

3. IMPLEMENTATION OF THE BIOELECTRICAL BASED COMPUTATIONAL MODEL

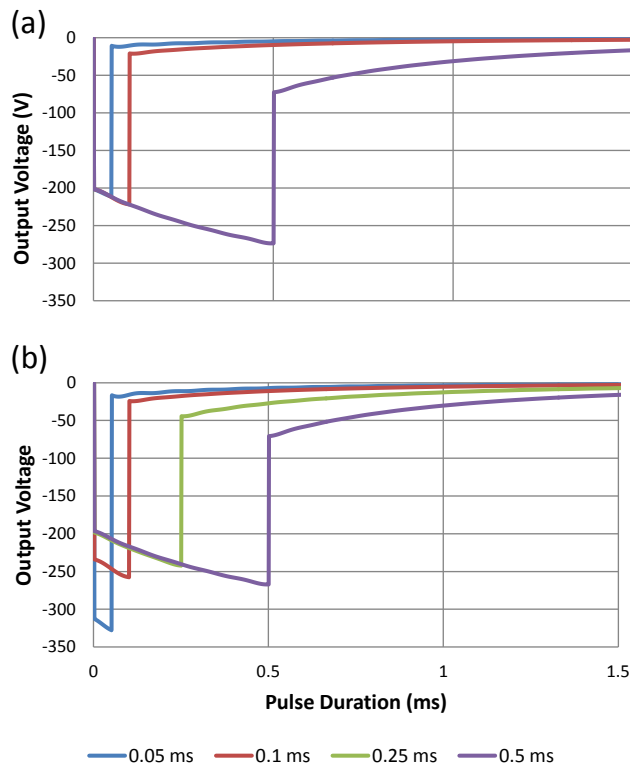


Figure 3.18: Output voltage of the DM for constant amplitude and MT conditions. Effect on the voltage at one point under the cathode of the CM for an input current fixed at (a) -40 mA and (b) MT for different pulse durations.

and σ_H .

3.5.2 Phantom measurements

The admittance ($Y = G + iB$) was measured using the two electrode method by an LCR meter (HIOKI, IM3533-01, Nagano, Japan) from 1 Hz to 200 kHz, Fig. 3.19. The calculation of the conductivity and permittivity is according to equations 3.21 and 3.22

$$\sigma = \frac{S}{G \cdot L} \quad (3.21)$$

$$\epsilon_r = \frac{B \cdot L}{\omega \epsilon_0 S} \quad (3.22)$$

3.5 Phantom experiments

Table 3.1: Materials for the fat-equivalent and muscle-equivalent phantoms

Material	Muscle-equivalent phantom (g)	Fat-equivalent phantom (g)	Effect
Deionized Water	800	400	Base Material
Agar	24	24	Form
Sodium Dehydroacetate	0	NA	Preservative
Glycerol	NA	400	Permittivity
Polyethylene Powder	NA	80	Permittivity
	NA	0	Conductivity (σ_L)
Sodium Chloride	0.4	0.8	Conductivity (σ_M)
	NA	3.2	Conductivity (σ_H)

where S is the surface area of the electrodes, L length of phantom sample, and ω angular frequency.

Deionized water was used as standard sample to verify the measurement results by comparing the results with an additional impedance analyzer (Wayne Kerr, 6500P). As shown in Fig. 3.20, the two measurements had similar results in their common frequency region.

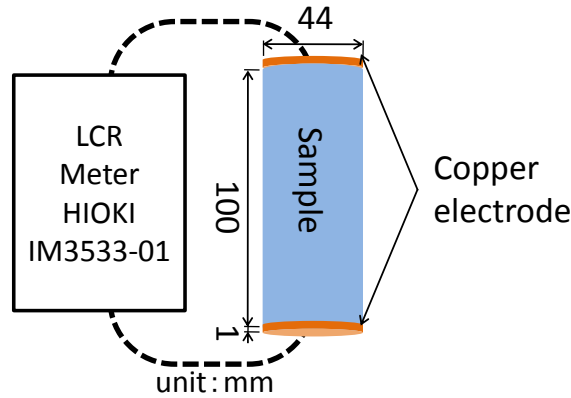


Figure 3.19: Measurement set up of the dielectric properties of the phantom tissues and deionized water samples using an LCR meter.

A sample from the fat-equivalent phantom and another from the muscle-equivalent phantom were prepared to measure the relative permittivity and conductivity. Figures 3.21 and 3.22 show that the dielectric properties of the phantom tissues agreed with

3. IMPLEMENTATION OF THE BIOELECTRICAL BASED COMPUTATIONAL MODEL

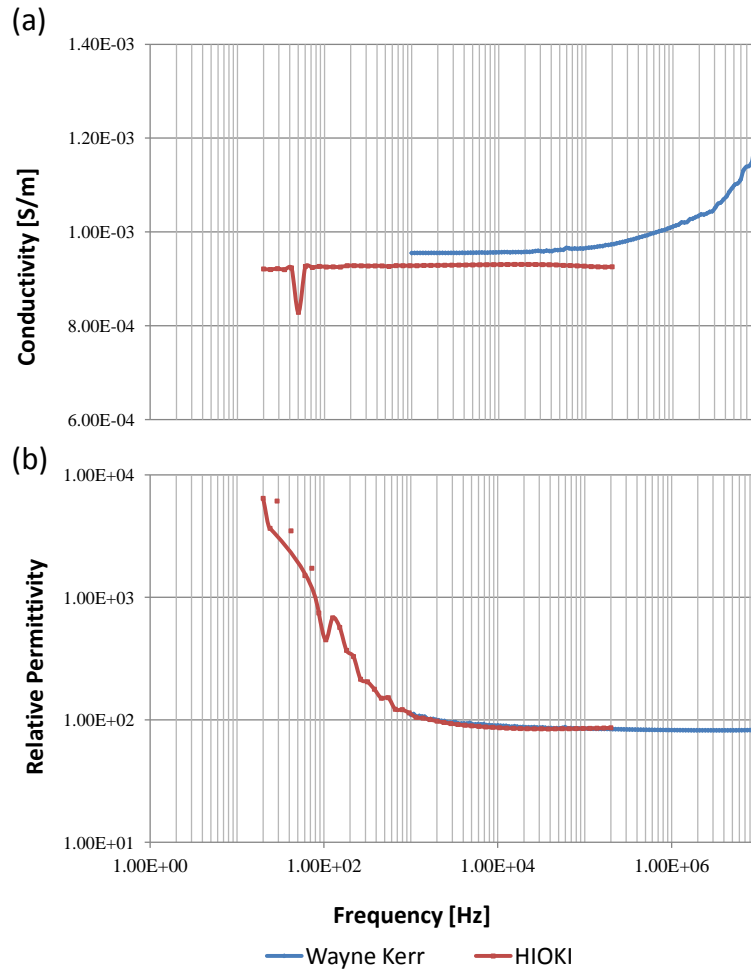


Figure 3.20: Verification of the phantom measurement experiment. The measurement of (a) conductivity and (b) relative permittivity of deionized water using two different impedance analyzers.

literature values (92, 117). In addition, measurements of the dielectric properties in multiple phantoms confirmed the robustness of the recipe. Storage in a refrigerator and measurements during one week showed that the phantom retained its dielectric properties across one week.

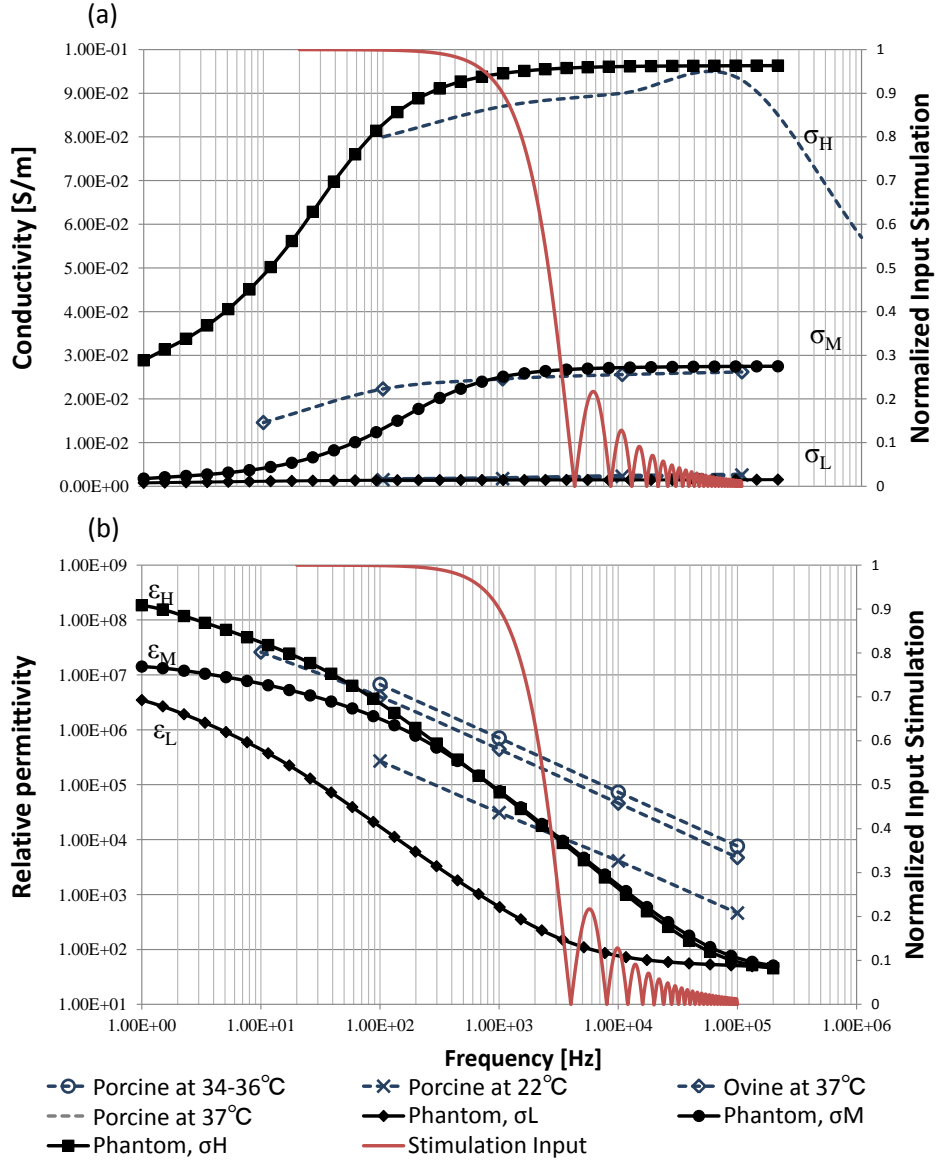


Figure 3.21: Dispersion of fat-equivalent phantom. (a) Conductivity and (b) relative permittivity of porcine tissue at 22 °C in (118), porcine tissue at 34-36 °C in (119), and the others in (92). Frequency response of a impulse stimulation signal of 250 μ s is shown as reference.

3. IMPLEMENTATION OF THE BIOELECTRICAL BASED COMPUTATIONAL MODEL

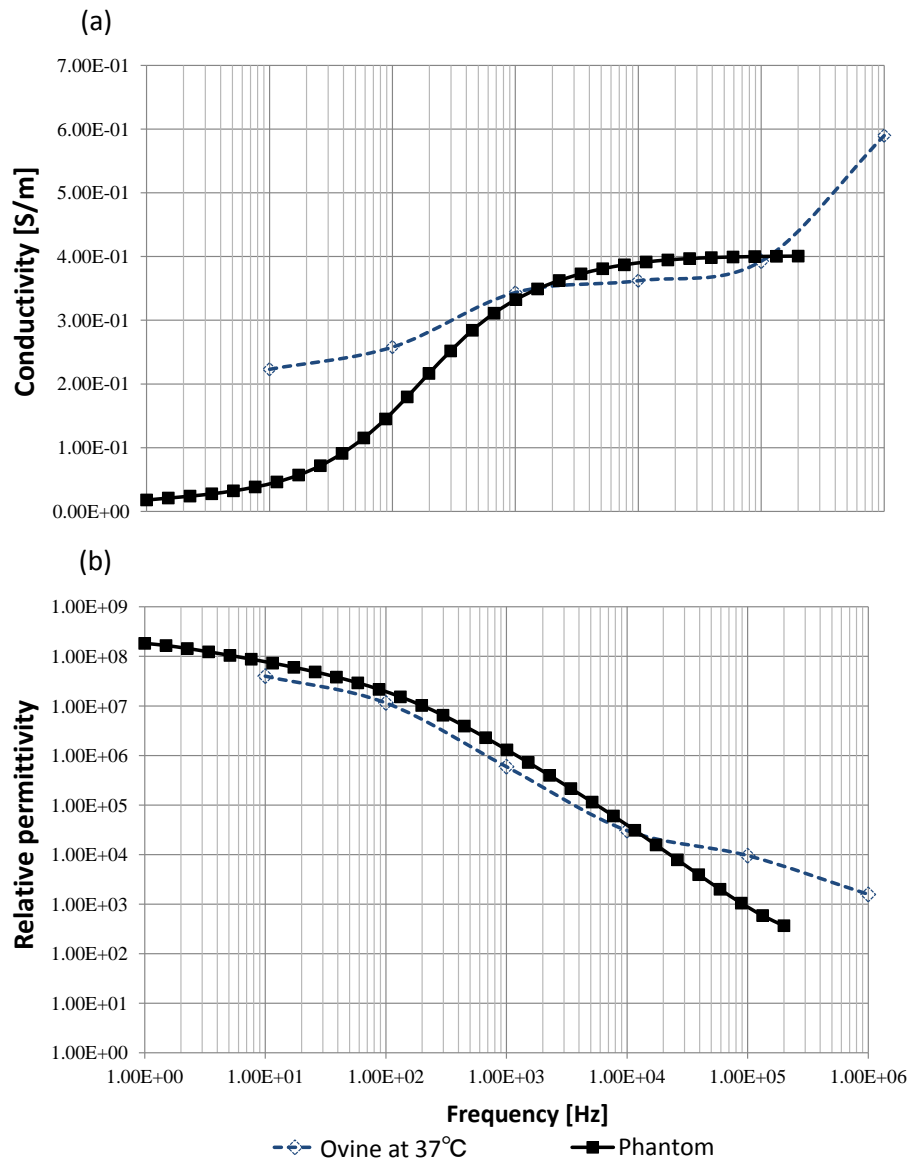


Figure 3.22: Dispersion of muscle-equivalent phantom. (a) Conductivity and (b) relative permittivity of ovine muscle at 37 °C in (92)

3.5.3 Human-phantom coupling

A semicircular fat-equivalent phantom with a thickness of 8.5 mm was coupled with subjects' thigh as shown in Fig. 3.23 (97). So that, skin, fat, and muscle of thigh were considered as one block-tissue under the fat-equivalent phantom. The location of the distal edge of the phantom was decided to be 10 cm from the knee for each subject, and an inter-electrode distance of 30 mm and 70 mm was chosen. An accelerometer was placed on the proximal electrode to measure the current or voltage stimulation amplitude necessary to detect the smallest thigh motion, which is referred as MT. It provides the advantage of adjusting the electrical properties of the phantom and studying, at the same time, muscle contraction.

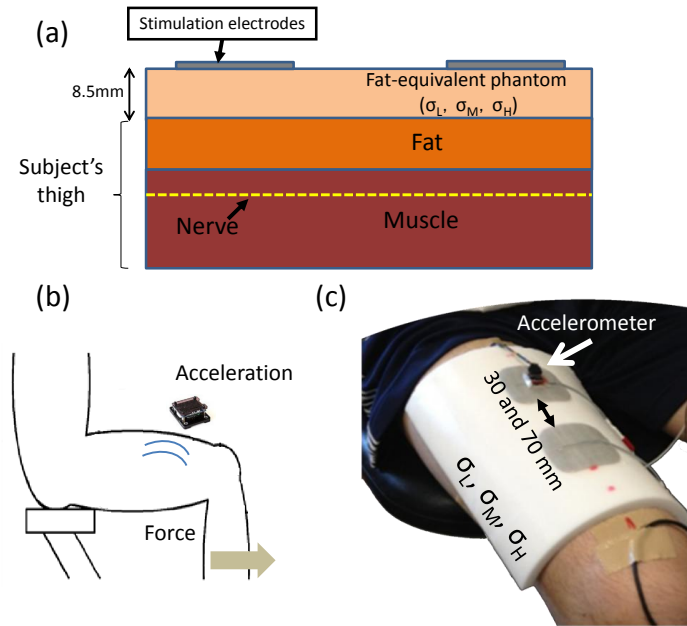


Figure 3.23: Human-phantom coupling experiment. A semicircular fat-equivalent phantom was couple with subjects' thigh (thickness of 0.85 cm, length of 20 cm, and three different conductivity dispersions: σ_L , σ_M , and σ_H). The phantom was tightly adjusted to the thigh using two straps at the level of the electrodes without causing a major stress in the thigh volume (the straps were omitted for clarity in the picture). An accelerometer was employed to detect MT. (a) Human-phantom coupling diagram, (b) MT detection, (c) experiment set-up.

Chapter 4

Validation and Simplification of the Quasi-Static Approximation For Neural Stimulation

4.1 Overview

Validation of the models is a fundamental step. The validation could be verified by measuring potential (needle or surface electrode for in vivo tissues) and nerve activation (strength-duration and recruitment-duration curves). Transient model and static models have shown good results for non-harmonic and harmonic input signals, respectively (71, 72, 73). Moreover, transient and quasi-static models have predicted experimental measurements of strength-duration and recruitment-duration curves to validate the computation of the nerve activation (76). If dielectric dispersion of the tissues under study are included in the models, a more realistic calculations could be achieved for non harmonic stimulation. However, there are not any experiment study that had validated the dispersive model. In the first part of this chapter, a validation experiment is introduced for this issue.

From a valid model of the dispersive tissues, quasi-static approximation is evaluated to determine the condition to approximate the dispersive model. Quasi-static approximation is valid if capacitive, inductive, and wave propagation conditions can be ignored (77). In the case of neural stimulation, short pulse duration with higher frequency components could invalidate the capacitive condition given by the dispersive

4. VALIDATION AND SIMPLIFICATION OF THE QUASI-STATIC APPROXIMATION FOR NEURAL STIMULATION

effect of the conductivity and permittivity (79). In addition, dielectric dispersion of the tissues presents a filtering effect in the potential distribution, which in turn, affects the neuronal excitation. It has been suggested that dispersion may be approximated by resistive and capacitive models (RM and CM) by selecting an optimal frequency. The previous simulation studies investigated it for over-simplified geometries and focused on brain electrical stimulation and no experimental validation has been conducted for the dispersive model (DM) and optimal frequency (71, 72, 78, 80, 81). In addition, most of the simulation studies of TES don't incorporate the dielectric dispersion of the tissues (120); they used the quasi-static approach (11, 41, 60, 121), as well as other application such as magnetic stimulation (85) and electromyography (5, 122).

Therefore, the difference of the extracellular potential computed by quasi-static approximation and DM and its effect in neuronal activity are examined in a realistic geometry for surface electrical stimulation. The optimal frequency for the conductivity parameter is investigated. Also, tissues-like phantoms with known dispersions are used for experimental validation of DM and the existence of an optimal frequency.

In this chapter, the DM is validated using tissues-like phantom. Then, the difference of the extracellular potential computed by quasi-static approximation and DM and its effect in neuronal activity are examined in a realistic geometry for surface electrical stimulation. The optimal frequency for the conductivity parameter is investigated. Also, tissues-like phantom with known dispersion are used to validate the existence of the optimal frequency in an experimental study.

4.2 Method

4.2.1 Formulation

The electric scalar potential (V_e) of the system was governed by the Laplace equation in frequency-domain (equation 4.1) to incorporate the dielectric dispersion of the tissues or phantoms. This dispersive model equation is referred as DM in this study.

$$\nabla \cdot [\sigma(\omega) + j\omega\epsilon_0\epsilon_r(\omega)] \nabla V_e = 0 \quad (4.1)$$

To obtain the time-dependent voltage distribution within a dielectric dispersive tissues using a non-harmonic stimulus (pulse waveform), the stimulus is converted to frequency-domain using discrete Fourier transform. Next, equation 4.1 is computed at each frequency component to obtain the transfer function in a specific location in the volume conductor with the normal current density to the surface of the electrode at 1 A/m² for current stimulation and 1 V for voltage stimulation. Then, the voltage is obtained by multiplying the input and transfer function and converting back to time-domain as explained in detail in section 3.2.1.

Grant et al. (123) showed that dispersion in the MHz and GHz frequency ranges had negligible effect on the voltage waveform in most tissues. So, in this study, the frequency components was truncated until 500 kHz, and sampling rate was 10 times higher (5 MHz) to avoid aliasing.

The RM or quasi-static approximation only accounts for the non-dispersive conductivity given by next equation 4.2:

$$\nabla \cdot [\sigma(f_c) \nabla V_e] = 0 \quad (4.2)$$

for a fixed f_c .

4.2.2 Tissue-like phantom experiment

Tissue-equivalent phantom has shown to have similar relative dielectric constant and conductivity to biological tissues. A muscle-equivalent phantom and a customized fat-equivalent phantom (20 × 2 × 10 cm) were fabricated to match low-mid-frequency for electrical stimulation applications as introduced in detail in section 3.5.

4. VALIDATION AND SIMPLIFICATION OF THE QUASI-STATIC APPROXIMATION FOR NEURAL STIMULATION

The validation of the DM was investigated by comparing potentials obtained experimentally and numerically at different points of interest in the tissue-like phantom and its model. The potentials were measured using a needle electrode mounted in the head of a purpose-built device, as shown in Fig. 4.1. The head of device allows to locate the needle in a desired position with a precision lower than 1 mm in 3D space.

The significant locations were picked up for the regions with larger voltage variability. A simulation study was employed to determine those regions. Figure 4.2a showed that the middle line between the electrodes was half of the input voltage, and the inner borders of the electrodes had a larger voltage variation along a plane parallel to the electrodes. By contrast, Fig. 4.2b presented a small voltage variation under the inner border of the electrodes and no variation in middle line between the electrodes for perpendicular planes to the electrode. Moreover, partial derivatives were calculated in Figs. 4.2c, 4.2d, and 4.2e for $|V_x|$, $|V_z|$, and $|V_y|$, respectively. The locations around the inner border of the electrode (along the y-axis and z-axis), and around the inner corners of the electrode (along the x-axis) had higher possibilities of variation. Thus, Fig. 4.3 shows the measurement points selected.

In addition, other conditions were considered to validate equation 4.1: tissue-like phantom (muscle and fat) and waveform (voltage or current, monophasic or biphasic, and pulse duration).

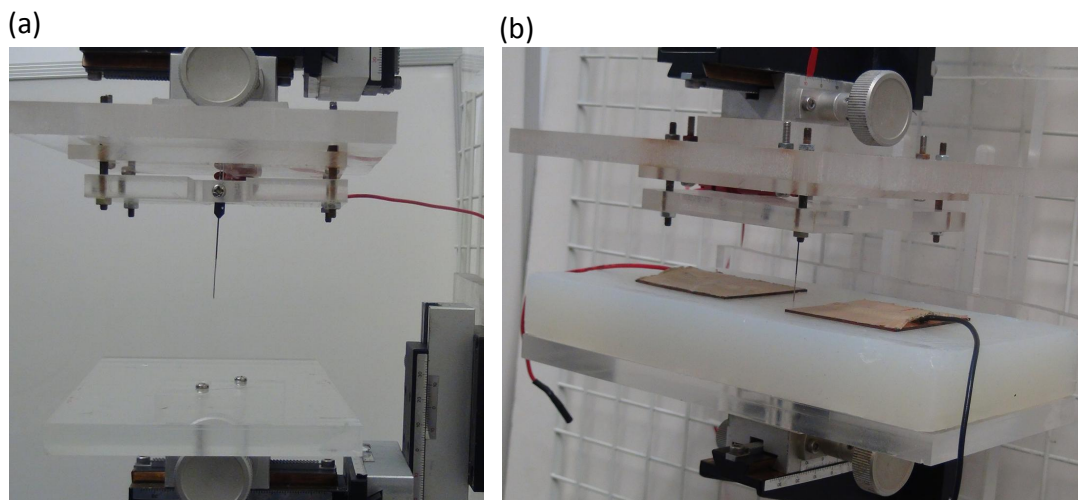


Figure 4.1: Experimental set up to measure the voltage in the tissue-like phantom. (a) Purpose-built device to pierce the phantom with the needle electrode at the desired location. (b) Measurement of the muscle-like phantom.

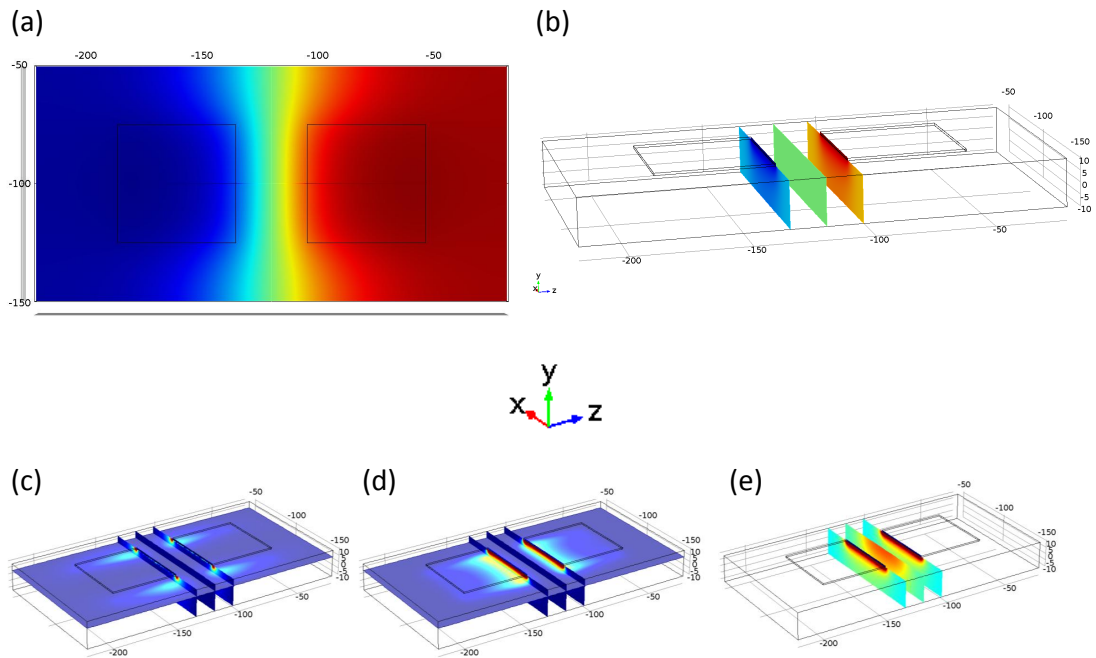


Figure 4.2: Voltage distribution in the phantom at 2 kHz to pick up significant points for validation of DM: Voltage distributions (a) and (b). Partial derivations of the voltage (c) $|V_x|$, (d) $|V_z|$, and (e) $|V_y|$ calculated for muscle-like phantom using current source. (A similar potential distribution was obtained for the fat-like phantom.) Units are in mm.

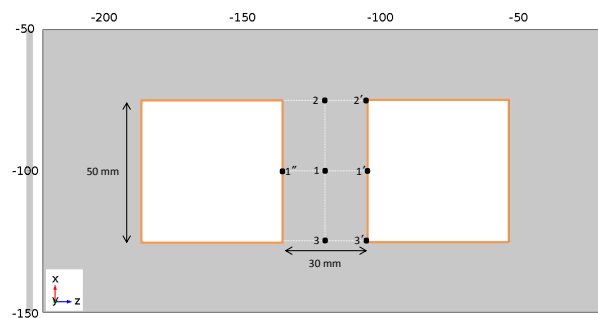


Figure 4.3: Selected locations for potential measurement in the phantom. Units are in mm.

4. VALIDATION AND SIMPLIFICATION OF THE QUASI-STATIC APPROXIMATION FOR NEURAL STIMULATION

4.2.3 Measurement locations for the validation of the dispersive model

Quasi-static approximation under-estimates or over-estimates the potential as a result of the conductivity choice. In addition, these errors could yield different neuron responses as potential and neural activation does not follow a linear relationship. For instance, Fig. 4.4 illustrates the output voltage using DM and RM calculated at some representative frequencies. The absolute values of the output voltage goes to zero when frequency decreased. Therefore, if pulse duration increased, RM at lower frequency would have a closer approximation to DM results.

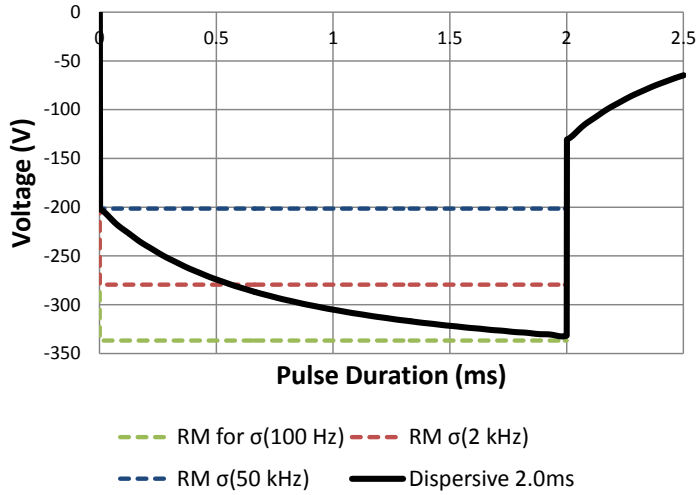


Figure 4.4: Output voltage obtained from the DM and RM for different frequencies using a pulse current of -40 mA in the CM.

Equations 4.1 for DM and 4.2 for RM were compared using equation 4.3 to find the conductivity that reduced the error of the extracellular potentials (optimal frequency or optimal conductivity). In addition, a compartment model of a myelinated nerve fiber (CRRSS model) was implemented to describe the temporal-spatial behavior of the AP due to the externally applied electric fields calculated to investigate the optimal frequency for neural activation by computing the motor threshold error by equation 4.4 at a given point within the model. The results presented were computed using a CM at a representative point located under the center of the electrode: 22.69 mm from the electrode-skin electrode interface and 8.22 mm from the fat-muscle interface.

$$V_{MeanError}(PW, f) = \frac{100}{PW} \sum_{t=1}^{PW} \left| \frac{DM(t) - RM(t, \sigma(f))}{DM(t)} \right| \quad (4.3)$$

$$MT_{Error}(PW, f) = \frac{MT_{DM(PW)} - MT_{RM(PW, \sigma(f))}}{MT_{DM(PW)}} \quad (4.4)$$

Figure 4.5 presents the flow diagram that summarizes the process of validation of the DM and the simplification of the quasi-static model.

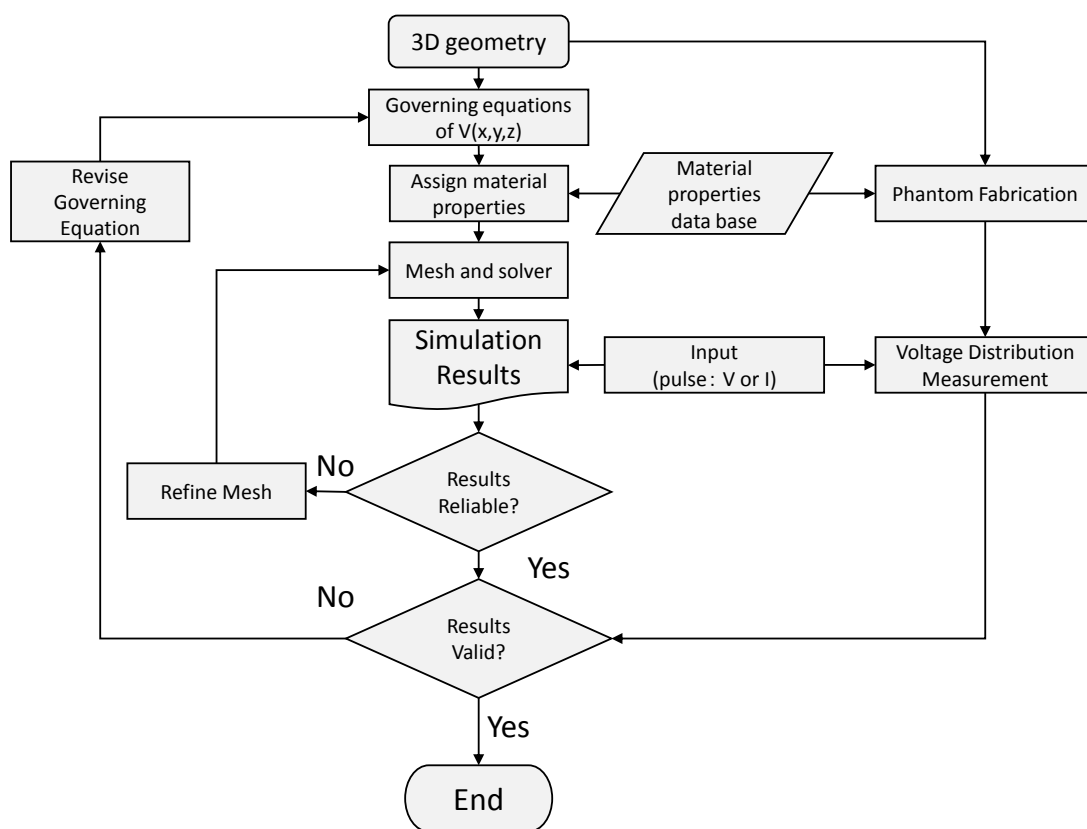


Figure 4.5: Flow diagram for the validation and simplification of the formulation.

4.3 Results

4.3.1 Validation of dispersive model by tissue-equivalent phantom

We validated the dispersive model by employing tissue-equivalent phantoms in significant locations using current stimulation, Fig. 4.3.

4. VALIDATION AND SIMPLIFICATION OF THE QUASI-STATIC APPROXIMATION FOR NEURAL STIMULATION

First, there was no variation of the measurements of voltage along depth distance (y-axis) between 1 mm and 20 mm, as predicted by the simulation (Fig. 4.6). The only difference is that the simulation showed a small difference between 5 mm and the other depths at 1' and 2' locations with a root mean square error (RMSE) of 70 mV and 89 mV, derived from Fig. 4.6c considering that the measurement error was 20 mV. Next, experiment and simulation had consistent potential results along the x-axis, which showed no voltage variation between potentials along the x-axis, Fig. 4.7. Finally, we revised the variation along z-axis (Fig. 4.8) for fat-like phantom. The experimental result showed that voltage varied significantly in this direction and simulation had the same outcome.

In addition, different conditions were investigated along z-axis for having higher variation: waveform and tissues-like phantom type conditions. Figure 4.9 confirmed that monophasic and biphasic waveforms are valid, and Fig. 4.10 showed that the model is also valid for different pulse durations (0.10, 0.15, 0.20, 0.25 ms) at a fixed position in the muscle-like phantom for current stimulation. Finally, the normalized RMSE shows a good agreement between simulation and experimental measurements of the voltage (Table 4.1).

Table 4.1: Estimation error of the voltage using the DM

Parameter	Normalized RMSE (%)	Note
X-axis	5.58(0.89)	
Y-axis (all positions)	7.25(2.13)	Different depths for the same insertion point increases the error
Z-axis	8.32(2.48)	Voltage-controlled signal has higher error due to the double layer effect
PW	6.44(1.94)	

4.3.2 Optimal frequency for quasi-static approximation

Optimal frequency was investigated to predict the results of the DM from the RM. Two comparisons were made: difference of the voltage profile ($V_{MeanError}$, equation 4.3) and difference of motor threshold (MT_{Error} , equation 4.4) at a given point within the model.

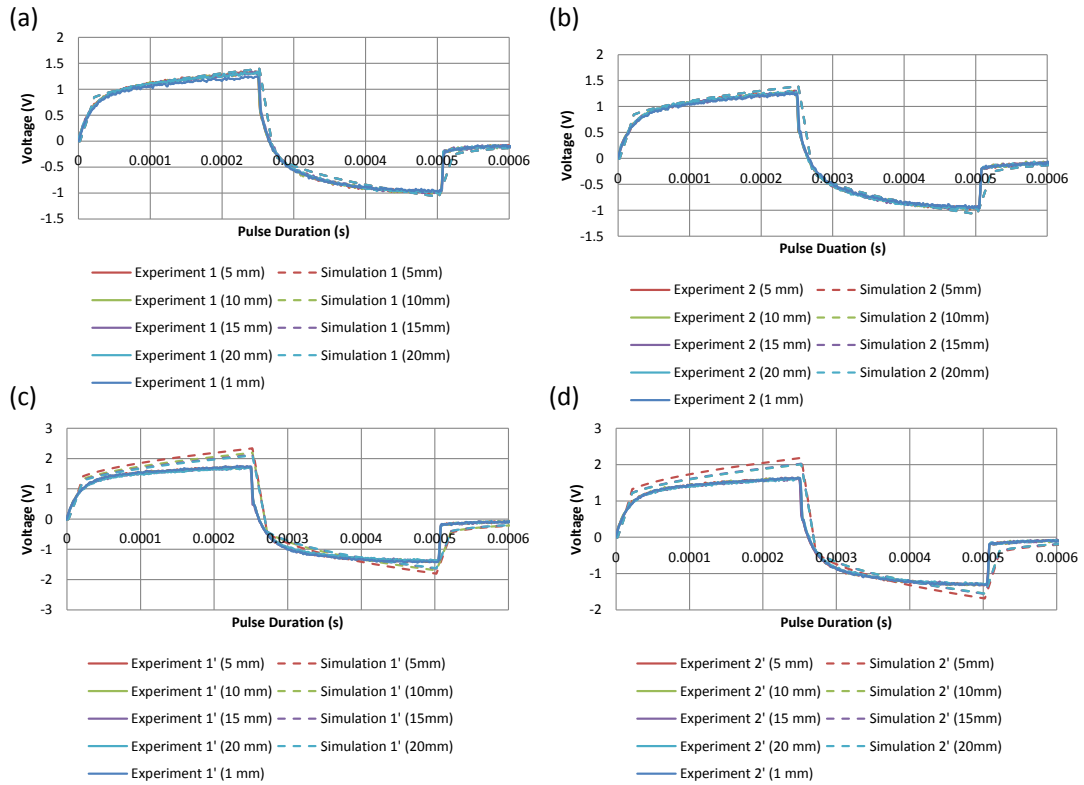


Figure 4.6: Voltage at different depths using current stimulation in a muscle-like phantom at positions (a) 1, (b) 2, (c) 1' and (d) 2', shown in Fig. 4.3.

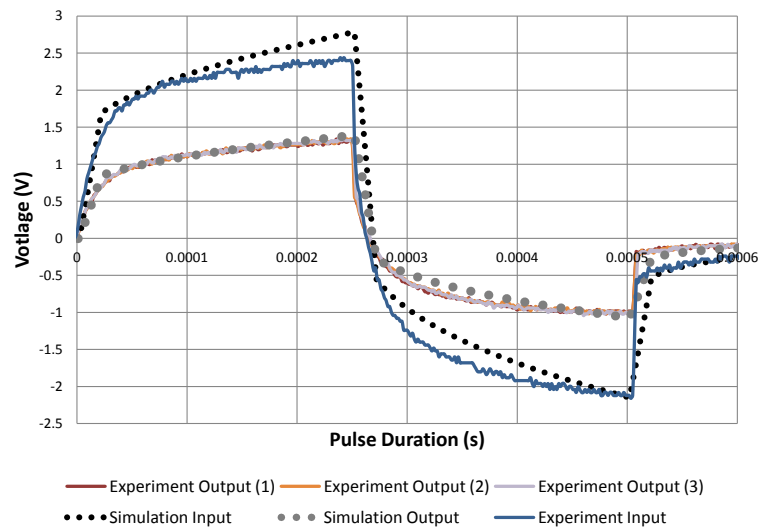


Figure 4.7: Voltage along x-axis locations using current stimulation in a muscle-like phantom at locations 1, 2, 3.

4. VALIDATION AND SIMPLIFICATION OF THE QUASI-STATIC APPROXIMATION FOR NEURAL STIMULATION

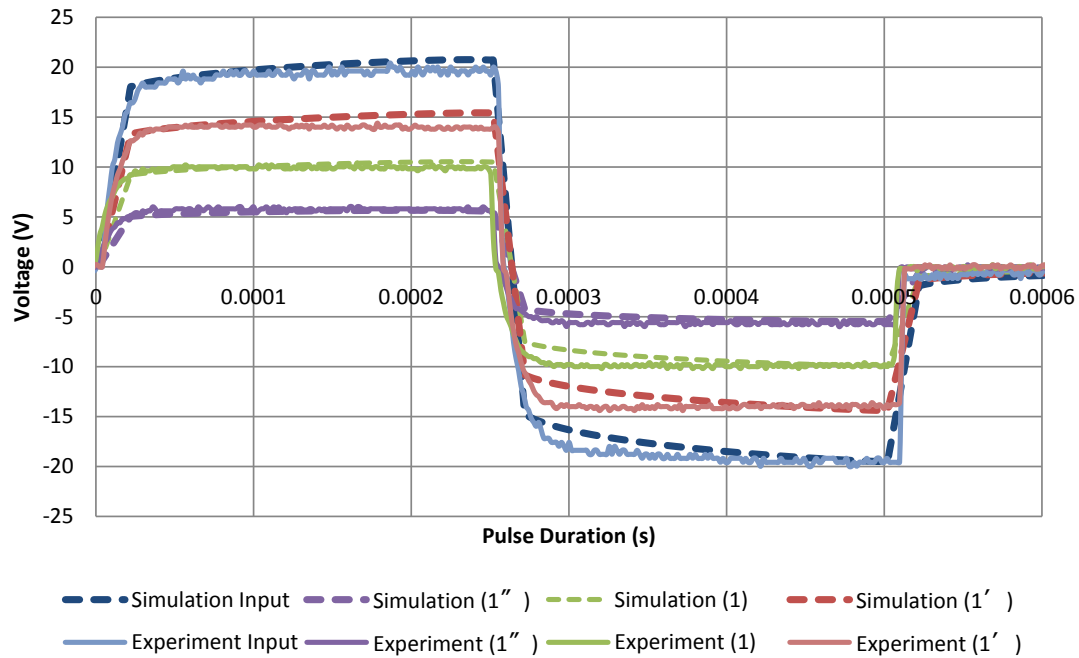


Figure 4.8: Voltage along z-axis locations using current stimulation in a fat-like phantom.

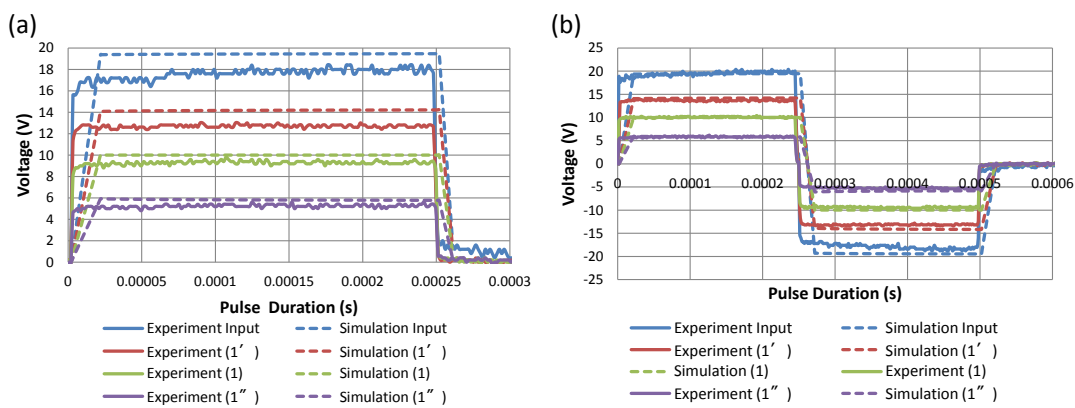


Figure 4.9: Voltage along z-axis locations using voltage stimulation in a fat-like phantom using (a) monophasic and (b) biphasic waveforms.

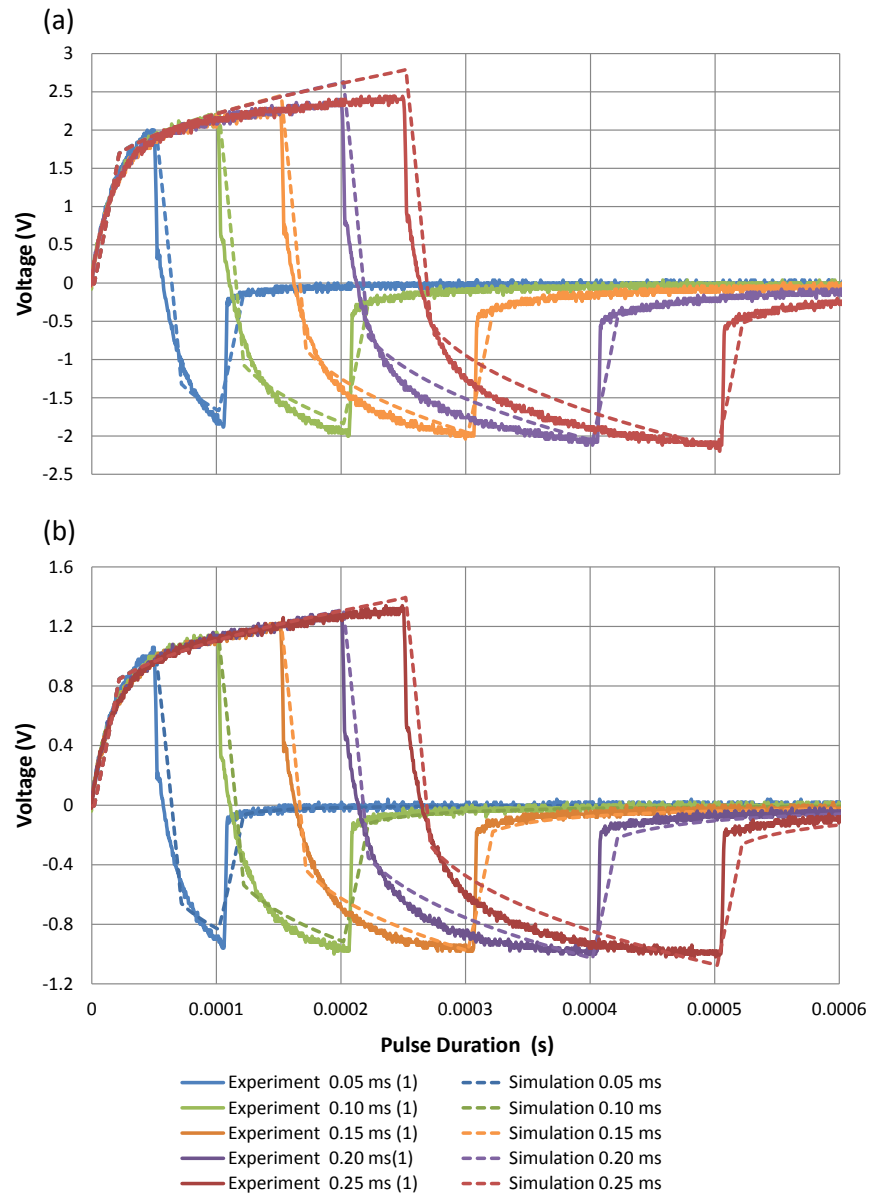


Figure 4.10: Voltage at different pulse durations in a muscle-like phantom using current stimulation. (a) Input and (b) output.

First, error of the voltage profile reported that RM approximates DM using low frequencies at large pulse durations. Conversely, RM approximates DM using high frequencies at small pulse duration, as shown in Fig. 4.11. Second, error of the MT reported that 1) RM approximates DM using middle frequencies at large pulse durations because of the saturation effect, which is a different response to the one exhibited by

4. VALIDATION AND SIMPLIFICATION OF THE QUASI-STATIC APPROXIMATION FOR NEURAL STIMULATION

voltage profile error, and 2) RM approximates DM using high frequencies at small pulse duration, as shown in Fig. 4.12.

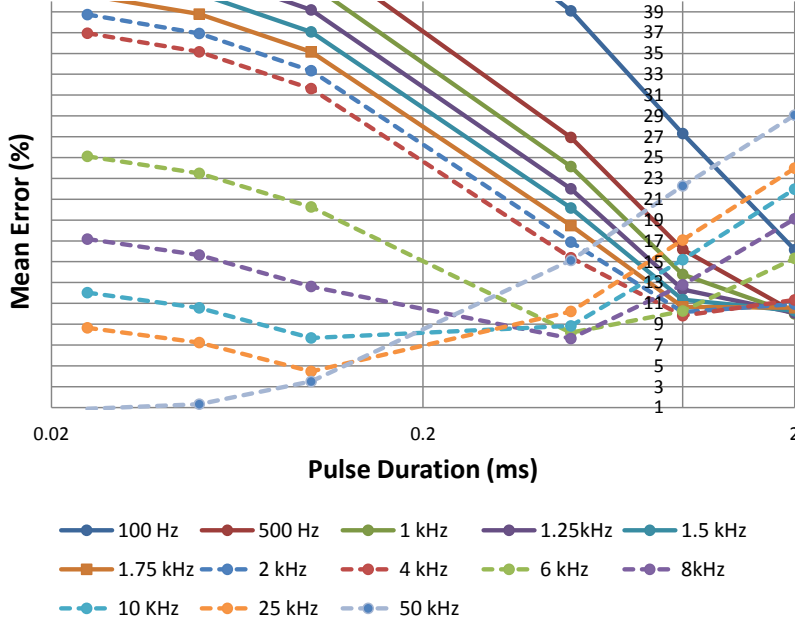


Figure 4.11: Mean error of the voltage calculated between DM and RM using a stimulation of -40 mA for a given point under the center of the cathode.

4.4 Discussion

The measurement of the potential distribution in vivo and force generation have been conducted for model validation. For potential distribution, the models have shown a similar transient response as experimental measurements (71, 72), where the good selection of the parameters resulted in a better approximation. However, there are no validation studies for DMs. For that, it is necessary to know the dispersion of the tissues which is not possible by in vivo experiments. Therefore, we used a tissue-like phantom with known parameters to validate the DMs. The first part of the experiments showed that the DM was valid.

In the second part, we were interested in finding an optimal frequency that approximates RM to DM by evaluating two aspects: voltage profile within the tissues and neural activation. From those experiments, the error minimization is achieved by low frequencies at large pulse duration (Fig. 4.11) and high frequencies at small pulse

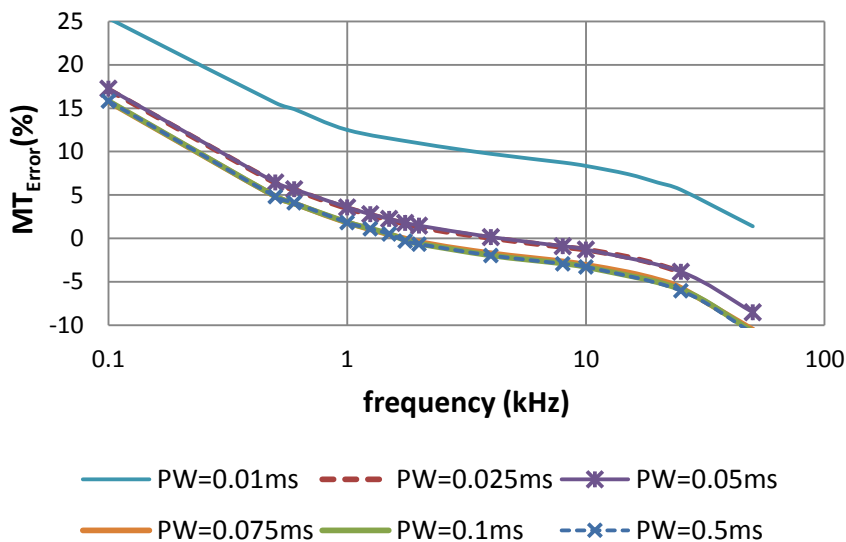


Figure 4.12: Error of the MT between DM and RM considering the pulse duration and frequency in the CM for a point under the center of the electrode.

duration (Fig. 4.12). The difference is that the saturation of the MT generated a lower limit of the optimal frequency at large pulse durations, which differed to the error minimization of the voltage profile, as summarized in Table 4.2.

This study confirmed that the quasi-static approximation is also valid if the conductivity is appropriately selected for realistic geometries. Previously, Bossetti et al. (78) showed that depending on the duration of the stimulus pulse, the error could change from 3% to 16% in threshold duration curves.

The optimal frequency converged to a lower limit as pulse durations increased. Grant et al. (81), in a study of deep brain stimulation, also showed that RM provides a good approximation of the voltage distribution for pulse duration larger than 0.5 ms, where voltage distribution calculated with the RM had a RMSE of 10% with respect to the dispersive capacitive model (model with dispersive permittivity and fixed conductivity). However, their study is limited to an infinite, homogeneous, isotropic volume conductor using a point current source stimulus. In addition, Butson et al. (80) showed the difference in the time course and volume activation for different values of permittivity in a study of deep brain stimulation. Although their method could be used to solve a dispersive capacitive model, they fixed the conductivity to 0.3 S/m and the solution became a non-dispersive capacitance model. They showed that the

4. VALIDATION AND SIMPLIFICATION OF THE QUASI-STATIC APPROXIMATION FOR NEURAL STIMULATION

capacitive effect causes a difference in nerve activation, but it is negligible during current stimulation for pulses larger than 0.5 ms. In addition, other studies have confirmed that the capacitive effect is negligible for mid-range material properties (76, 79). The pulse duration of the experiments through this study are at 0.5 ms (typical for FES), which is in the range of saturation where RM is a good approximation of DM.

Table 4.2: Summary of the optimal frequencies to approximate DM by RM

Conditions	Voltage profile	Nerve Activation
Higher PW	PW > 2 ms:	PW > 0.075 ms (saturation): 1 kHz < f < 3 kHz
	f < 1.25 kHz	
	1 ms < PW < 2 ms: 1.25 kHz < f < 4 kHz	
Middle PW	0.12 ms < PW < 1 ms:	PW > 0.075 ms (saturation): 1 kHz < f < 3 kHz
	6 kHz < f < 25 kHz	
	0.075 ms < PW < 0.12 ms 25 kHz < f < 50 kHz	
Lower PW	PW < 0.12 f ~ 50 kHz	PW < 0.075 ms (no saturation): f > 2 kHz

4.5 Conclusions

For first time, this chapter validated a DM by employing tissue-like phantom with known dispersive response of its conductivity and permittivity. The capacitive condition of the quasi-static approximation was investigated as it could be invalid for short pulse duration input signals with high frequency components in the case of neural stimulation. For that, optimal frequency was inspected in order to observe whether quasi-static approximation could approximate a DM on two aspects: voltage profile within the tissues and neural activation. The minimization of the error was achieved by low frequencies at large pulse duration and by high frequencies at small pulse duration. The difference is that optimal frequency converged to a lower limit as pulse durations increased for neuronal activation. The pulse duration of the experiments through this study are at 0.5 ms (typical for functional electrical stimulation), which is in the range of saturation where RM is a good approximation of DM.

Chapter 5

Geometric Representations of the Volume Conductor on Nerve Activation

5.1 Overview

Volume conductor models with different geometric representations, such as the parallel layer model (PM), the cylindrical layer model (CM), or the anatomically based model (AM), have been employed during the implementation of bioelectrical models for electrical stimulation (FES). Evaluating their strengths and limitations to predict nerve activation is fundamental to achieve a good trade-off between accuracy and computation time. However, there are no studies aimed at clarifying the following questions: 1) Does the nerve activation differ between CM and PM? 2) How well do CM and PM approximate an AM? 3) What is the effect of the presence of blood vessels and nerve trunk on nerve activation prediction? 4) What is the effect of nerve curvature? This chapter addressed these questions by comparing nerve activation between CM, PM, and AM models by FES. The MT was used to evaluate the models under different configurations of superficial electrodes (size and distance), nerve depths, and stimulation sites. Additionally, non-homogeneous tissues were inspected for a human thigh. The results showed that the CM and PM had a high error rate, but the variation of the MT followed the same tendency for electrode size and inter-electrode distance variation as AM. The work presented here was published in (124, 125).

5. GEOMETRIC REPRESENTATIONS OF THE VOLUME CONDUCTOR ON NERVE ACTIVATION

5.2 Method

Three models with different geometric representations were implemented to compare their nerve activation at different stimulation sites, electrode size, and targeted nerve depth. The models were cylindrical, parallel, and anatomically based. The AMs of the thigh were constructed by segmenting the MRI data sets of two subjects (S1 and S2) using our pulse-coupled neural network segmentation and bottom-up saliency method (105).

Models composed of skin, fat, muscle, cortical bone, bone marrow, sciatic nerve, femoral artery, and femoral vein were defined as the reference models for each subject (AM1-R, AM2-R). In addition, AM1-(VN)' and AM2-(VN)' were obtained from AM1-R and AM2-R by excluding the sciatic nerve and blood vessels to inspect the absence of these tissues. Conductivity was assumed to be isotropic for all tissues with the exception of the muscle tissue, which was considered anisotropic (transversal and longitudinal conductivities) (92, 117). The geometry and electrical parameters of the models are shown in Table 5.1.

Table 5.1: Geometry and conductivity parameters of the models

Tissue Layer	Thickness of CM1 and PM1 (cm)	Thickness of CM2 and PM2 (cm)	Conductivity (mS · m ⁻¹)
Skin	0.20	0.20	0.79
Subcutaneous Fat	1.24	1.73	42.27
Muscle	4.32	5.02	82.38 (transversal) 329.53 (longitudinal)
Cortical Bone	0.63	0.57	20.24
Bone Marrow	0.87	0.94	101.93
Blood	NA	NA	700.0
Sciatic Nerve	NA	NA	29.89

Square electrodes were modelled with areas from 1.00 cm² to 25.00 cm². The stimulation electrodes were placed in pairs on the posterior, anterior, lateral, and medial locations. Both electrodes were moved by an inter-electrode distance (edge to edge) from 1.00 cm to 6.00 cm, with the centerline of the two electrodes unchanged. Three

fibers thickness of the targeted nerves ($8\ \mu\text{m}$, $12\ \mu\text{m}$, and $16\ \mu\text{m}$) were considered. The middle of one straight myelinated fiber with length of 63 mm was placed below the center of the proximal electrode and was oriented parallel to the z axis. In sections 5.3.1 to 5.3.3, the depth of the nerve fiber was at the most superficial location within the muscle domain of each site in the AM (Fig. 5.1a) (124). For the case of the CM and PM, the depth was determined with an average distance between the nerve and fat-muscle boundary for all sites in the AM. In section 5.3.4, deeper depths were employed to consider the effect of the nonhomogeneities. A current square pulse with a duration of 0.5 ms was employed as cathodic stimulation, and amplitude was modified between 5 mA to 500 mA to obtain MT.

A two-step method was implemented to calculate activation in the muscle (57). In the first step, the voltage within the tissues, $V_e(\text{V})$, was computed according to a non-dispersive model. Although the stimulation waveform is not harmonic (square pulse), the dispersive nature of the conductivity and permittivity of the biological tissue is omitted to improve computation time. This is because that the quasi-static approximation can be used to approximate a DM considering an appropriate value of conductivity (77, 78). We confirmed that the appropriate conductivity that approximates the DM for our simulation models' geometry is f_c equal to 2 kHz.

The model was constructed, discretized and solved using COMSOL Multiphysics 4.4. The models were discretized into an average of 704×10^3 tetrahedral elements for PMs and 1.7×10^6 for the other models. As result, an average of 986×10^3 and 2.2×10^6 degrees of freedom was computed in the system matrix for PMs and the rest of the models, respectively. The quasi-static model was solved using an iterative linear solver (conjugate gradients) at each point within the tissues domain to determine the potential distribution; it took 200 s for the AMs to be solved using a quad-core INTEL@ CoreTM i7 -960 processor at 3.2 GHz and 24.0 GB of RAM memory. The PMs were three times faster than CMs, which were three times faster than AMs.

A detailed model of the nerve was to implemented to describe the temporal-spatial behavior of the AP at different configurations of electrode size, inter-electrode distance, and nerve depth. The AP generation was calculated from the voltage gradient around the target nerve using a compartment model of a straight mammalian nerve fiber (55, 56, 57).

5. GEOMETRIC REPRESENTATIONS OF THE VOLUME CONDUCTOR ON NERVE ACTIVATION

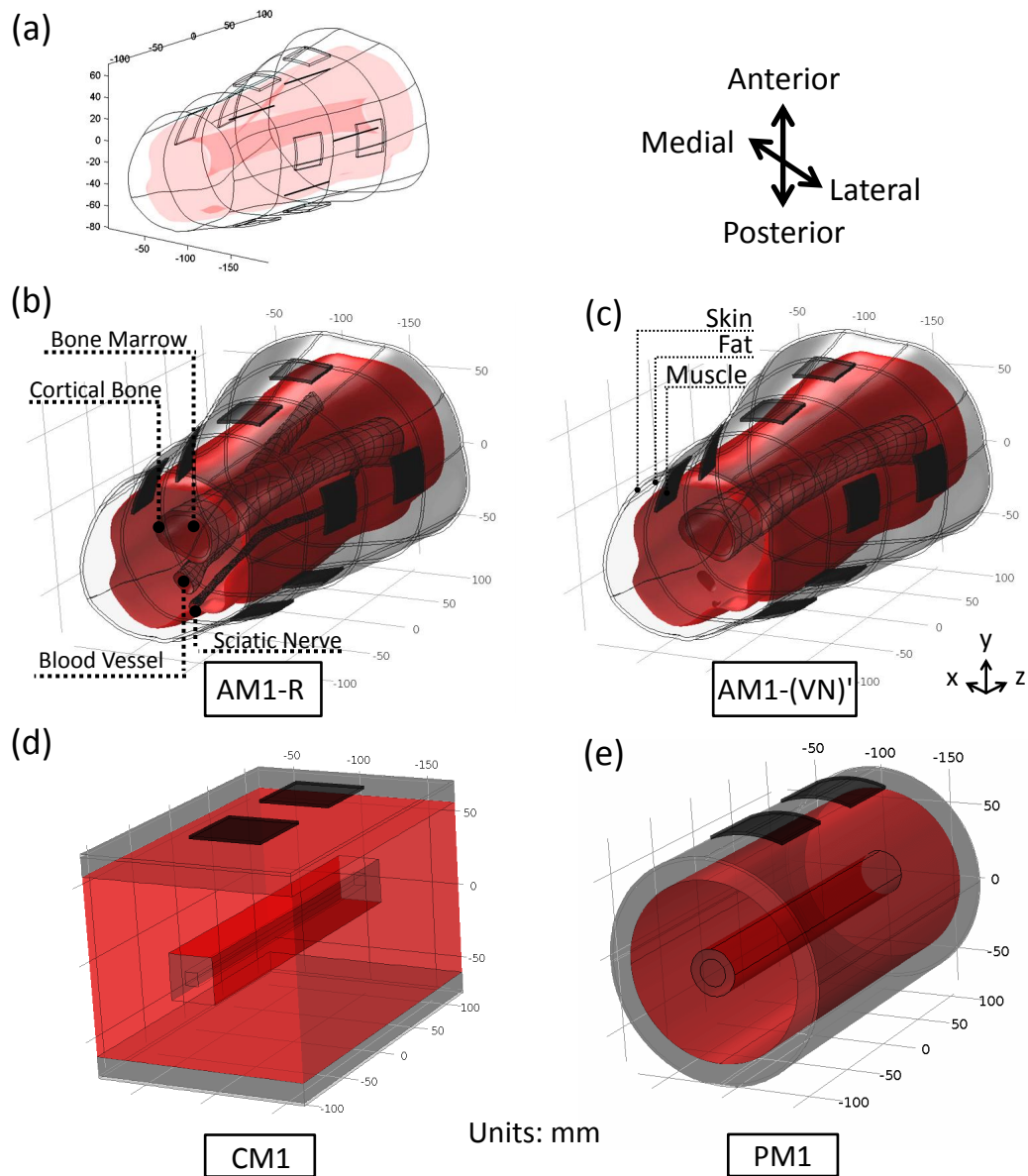


Figure 5.1: Different geometries of volume conductors derived from the thigh. AM1-R: reference model, AM1-(VN)': reference model without sciatic nerve and blood vessel, CM: cylindrical model, and PM: parallel model for S1. The location of the nerves is shown in (a).

The activation error was defined as the error between the MT calculated by the AM-R and the model under study. The current stimulation amplitude was modified by using a binary search algorithm to find the MT until the error was lower than $10 \mu\text{A}$.

Figure 5.2 presents the flow diagram that summarizes the process of verification of CM, PM, and non-homogeneities.

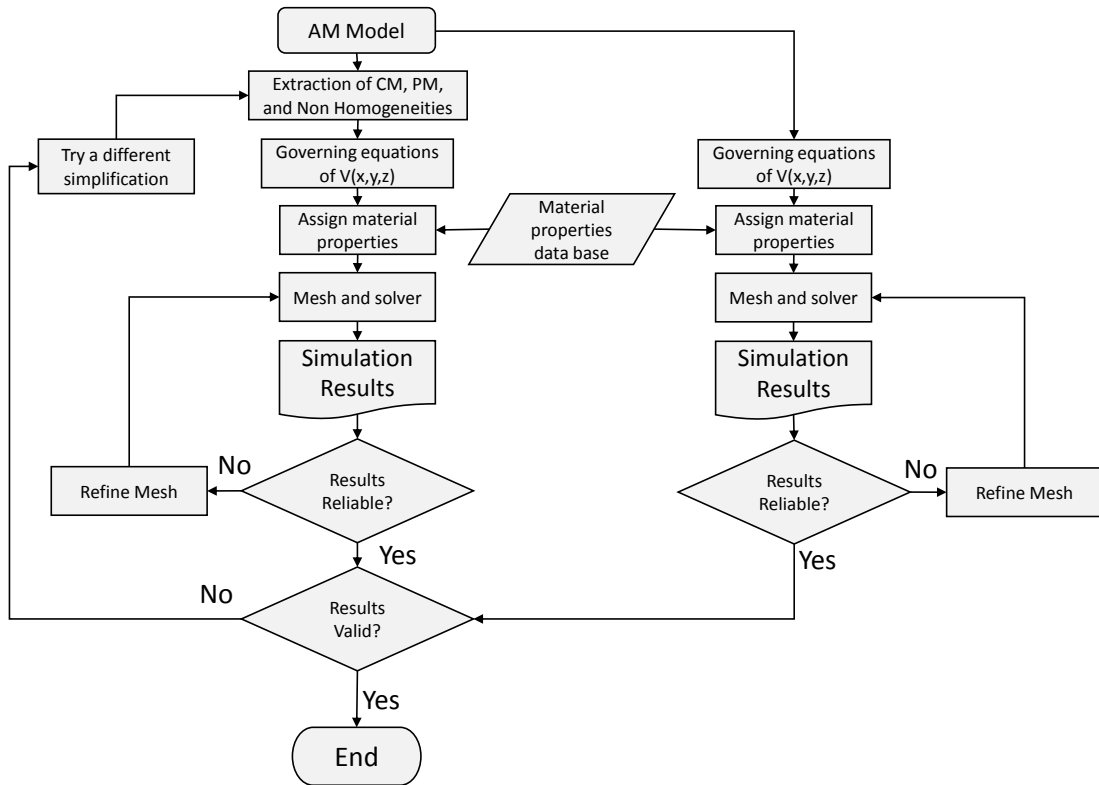


Figure 5.2: Flow diagram for the verification of simplified geometries.

5.2.1 Average fat thickness and bone-to-muscle distance

To interpret the difference between the results given by all the models and to adjust the fat thickness and bone location in Fig. 5.10a, the average fat thickness and average bone-to-muscle distance were calculated. First, the fat and bone boundaries were projected onto the xz -plane (medial and lateral sites) and yz -plane (anterior and posterior sites) as shown in Figs. 5.3a and 5.3b (124). Then, the average bone-to-muscle distance and fat thickness were calculated along z -axis within the range covered by variation of electrode size and inter-electrode distance for all sites (Figs. 5.3c and 5.3d).

5. GEOMETRIC REPRESENTATIONS OF THE VOLUME CONDUCTOR ON NERVE ACTIVATION

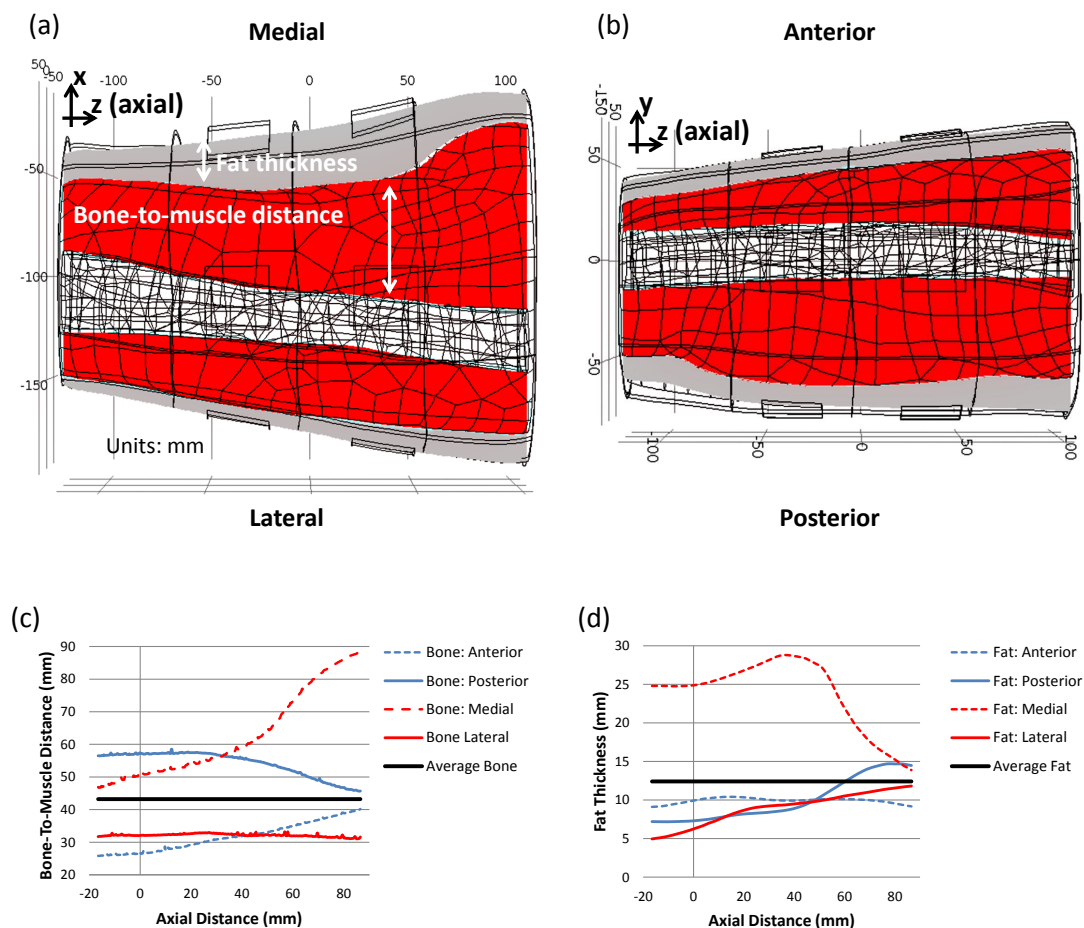


Figure 5.3: Projections of the tissues boundaries. (a) and (b) are boundaries of fat and bone tissues projected on a 2D plane. (c) and (d) are profiles of the bone-to-muscle distance and fat thickness obtained from the four stimulation sites.

5.3 Simulation results

5.3.1 Nerve activity prediction by the CM and PM

The CM and PM were obtained for two subjects. The electrodes were located at the anterior, posterior, medial, and lateral sites of the thigh (Fig. 5.1). Figure 5.4 (124) shows the distribution of the activation error. A two-way ANOVA test ($F(1,184)=4.78$, $p < 0.03$), followed by a Bonferroni post hoc test, showed a significant difference between CM and PM at the four stimulation sites. The activation error was different between sites because the bone depth and fat thickness at each site were different. To quantify

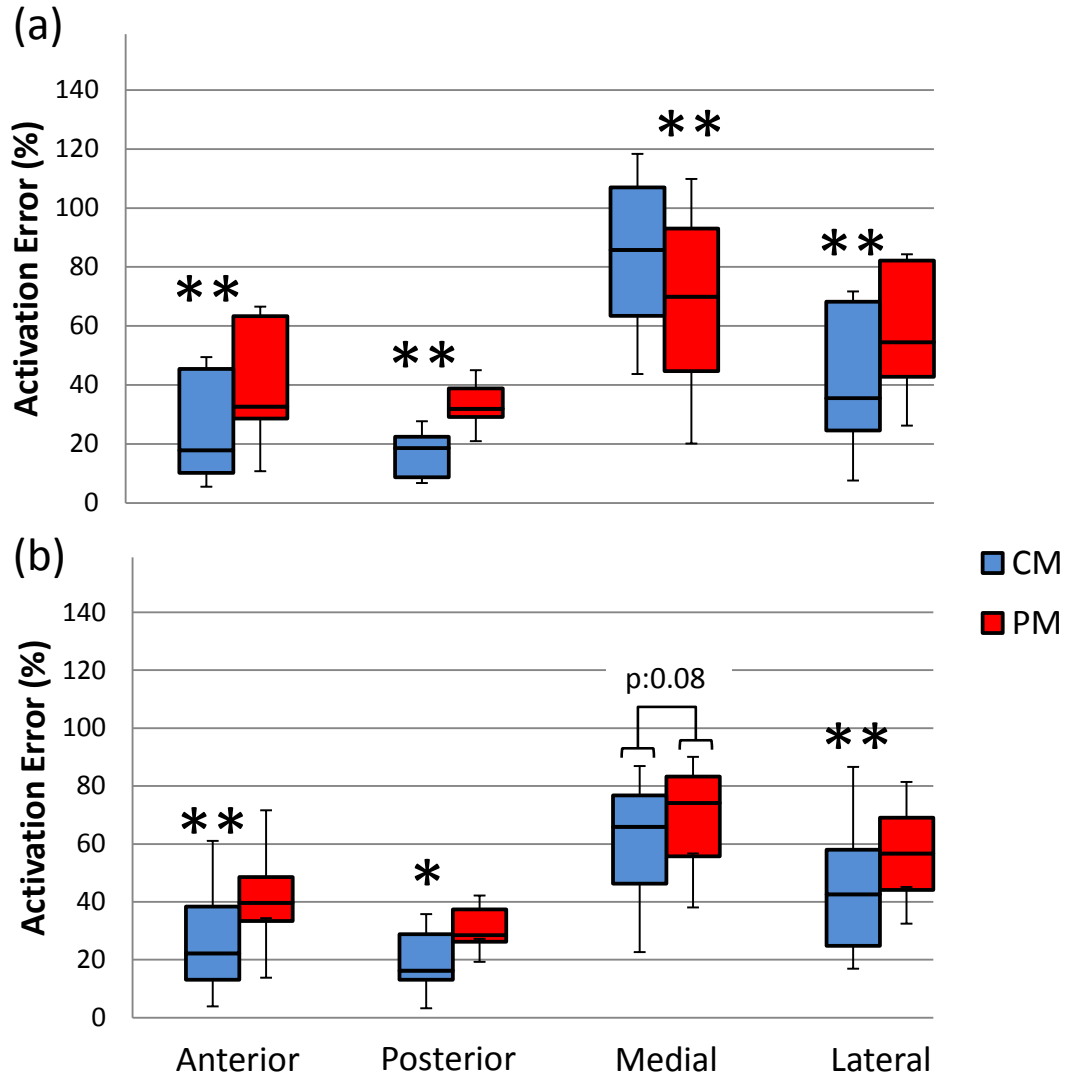


Figure 5.4: Distribution of the activation error of the PM and CM at the four stimulation sites for variations in electrode size (1.00 cm², 9.00 cm², and 25 cm²), inter-electrode distance (2 cm, 4 cm, and 6 cm), and fiber thickness of the targeted nerve (8 μ m, 12 μ m, and 16 μ m). *p<0.01 and **p<0.001 (two-way ANOVA followed by Bonferroni post hoc test, N=4 per group). (a) is S1 and (b) is S2.

the geometry difference between sites, the average fat thickness and average bone-to-muscle distance of the AM-R1, AM-R2, CM, and PM were calculated. Figure 5.5 (124) presents the discrepancy between the average fat thickness and average bone distance of the AM-R and CM or PM for each site. The discrepancy of the average fat thickness

5. GEOMETRIC REPRESENTATIONS OF THE VOLUME CONDUCTOR ON NERVE ACTIVATION

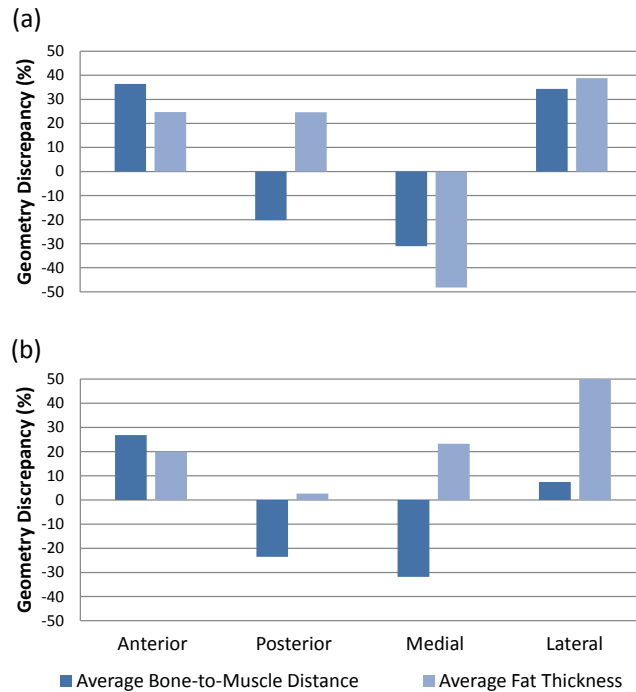


Figure 5.5: Geometry discrepancy of bone location and fat thickness between the AM-R and CM or PM at the four stimulation sites. A positive discrepancy means that the CM and PM have a larger average bone-to-muscle distance or average fat thickness than AM. (a) is S1 and (b) is S2.

followed a similar behavior of the activation error. However, the bone location is not significant as shown later in Fig. 5.10b.

5.3.2 CM and PM predicting AM-R nerve activation tendency

Cross-correlation was used to determine how well the PM and CM predict the MT of the AM-R when two parameter were under study: 1) inter-electrode distance variation (1 mm to 60 mm with steps of 5 mm, with a fixed electrode area of 25 cm²). 2) electrode size variation (1, 2.5, 4, 6.25, 9, 12.25, 16, 20.25, and 25 cm², with a fixed inter-electrode distance of 4 cm). Figure 5.6a illustrates that the MT between the models shows a similar tendency. In addition, cross-correlations between the models at the four stimulation sites are shown in Fig. 5.6b, indicating that the CM and PM can predict the behavior of the AM (124).

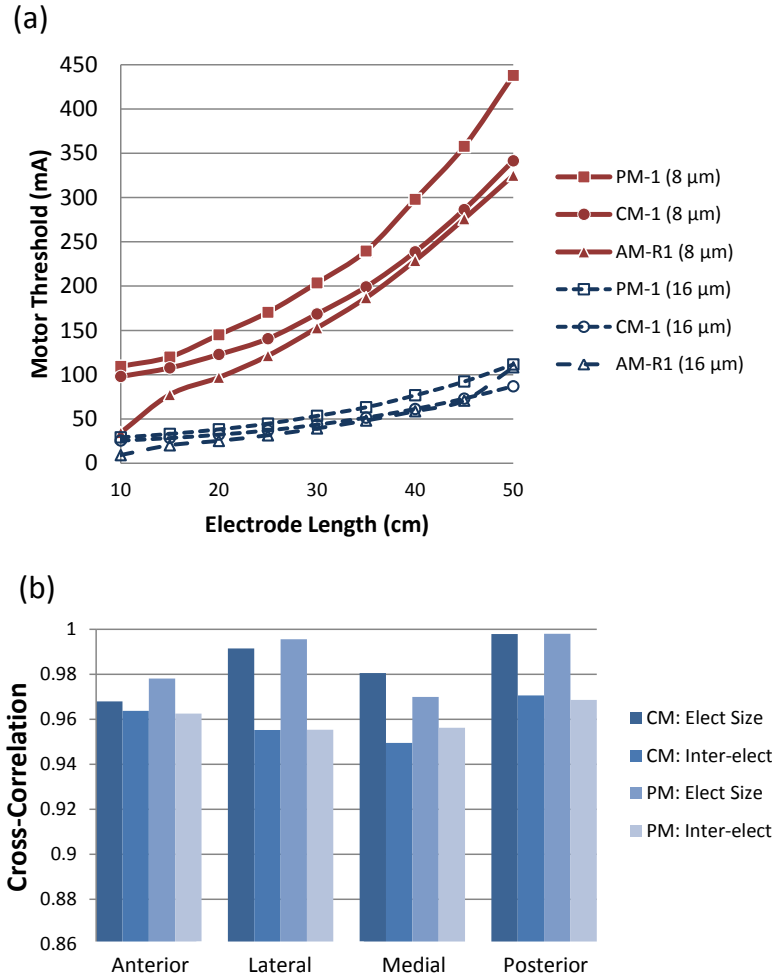


Figure 5.6: Cross-Correlation between models. (a) MT of CM1, PM1, and AM-R1 for electrode size variations at the anterior site. (b) Cross-Correlation of the MT between CM1 or PM1 and AM-R1.

5.3.3 Effect of non-homogeneities in the activation of superficial nerves

The non-homogeneities under inspection were the sciatic nerve and the femoral blood vessel tissues. For these, AM-(VN)' was compared to the AM-R to determine whether the absence of these tissues in AM-(VN)' was negligible. A one-way ANOVA test, $F(3,88)=4.98$ $p<0.01$ for S1 and $F(3,80)=3.53$ $p=0.018$ for S2 followed by a Bonferroni post hoc test, showed that there was no a significant increment of the activation error between the medial and anterior sites due to the absence of blood vessel and sciatic

5. GEOMETRIC REPRESENTATIONS OF THE VOLUME CONDUCTOR ON NERVE ACTIVATION

nerve, except for posterior-lateral (S1) and posterior-anterior (S2). However, we can observe that the error was higher at medial and posterior sites in S2 and posterior site in S1, Fig. 5.7 (124).

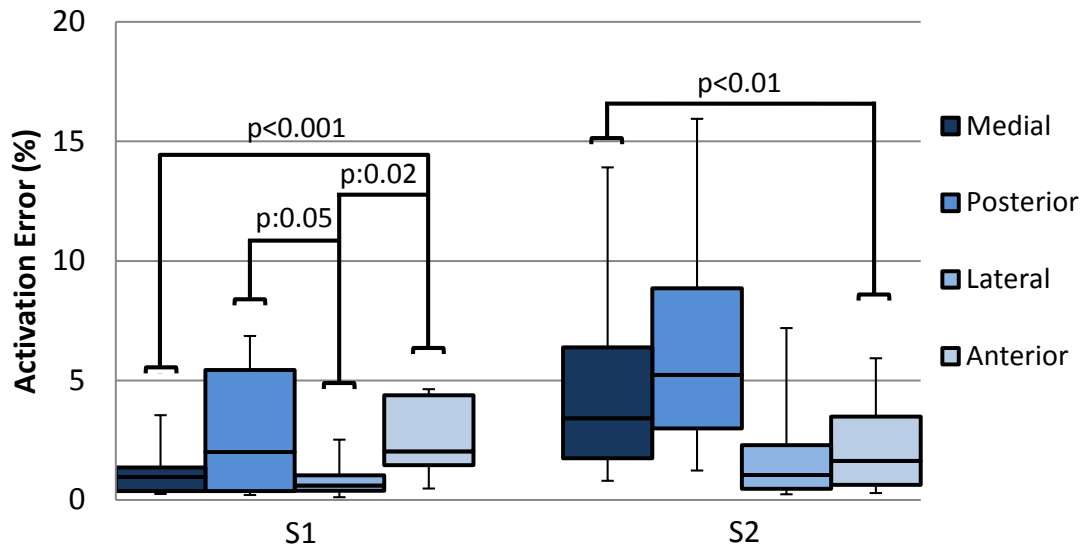


Figure 5.7: Distribution of the activation error of AM-(VN)' with respect to AM-R at the four stimulation sites for variations in electrode size (1.00 cm², 9.00 cm², and 25 cm²), inter-electrode distance (2 cm, 4 cm, and 6 cm), and fiber thickness of the targeted nerve (8 μ m, 12 μ m, and 16 μ m). One-way ANOVA followed by a Bonferroni post hoc test, N=6 per group.

5.3.4 Effect of nerve depth and curvature in the activation prediction

The targeted nerves were located at different depths to investigate the effect of the model geometry and depth. In addition, special attention was paid to the influence of the presence of a blood vessel and sciatic nerve trunk near targeted nerves. Two electrodes (9 cm² and 25 cm²) with an inter-electrode distance of 4 cm were located at the four sites of S1. In the case of the AM1-(VN)', Fig. 5.8 (124) shows that the activation error was lower (<5%) for the anterior and lateral sites. However, the activation error at the medial site increased dramatically and, to a lower extent, at the posterior site. The observed perturbations occurred near the blood vessel for the medial and nerve trunk for the posterior site. The average muscle-to-blood vessel and muscle-to-nerve trunk were 20.17 mm and 30.07 mm, respectively.

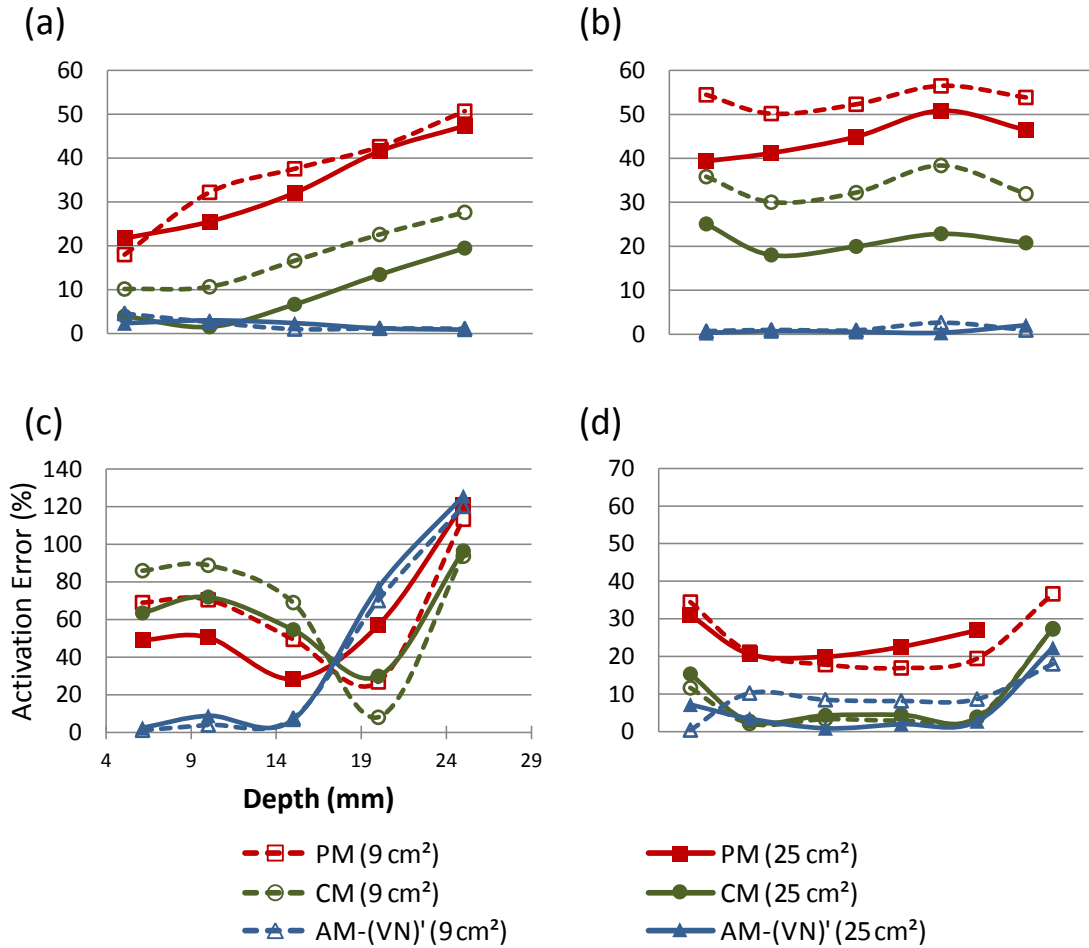


Figure 5.8: Effect of nerve depth. Prediction error of PM1, CM1, and AM1-(VN)' with respect to AM-R1 at the four stimulation sites. (a) Anterior, (b) lateral, (c) medial, (d) posterior.

Next, depth and curvature of a nerve were investigated around the middle thigh. The straight nerve was obtained from average of a curved nerve that was taken from the sciatic nerve. The starting point (activation point) of the AP at MT stimulation was indicated by a circle. In order to investigate only the effect of the curvature, the distance between the targeted nerve and the stimulation electrode had to be isolated. For that, a straight nerve was located 19 mm from the electrode, and the closest point of the curved nerve to the electrode was located at the same distance, as shown in Fig. 5.9 (125). Then, the other points of the curved nerve were in a deeper location than the straight nerve. That means that if the MT of the curved nerve was the same or

5. GEOMETRIC REPRESENTATIONS OF THE VOLUME CONDUCTOR ON NERVE ACTIVATION

higher than the straight nerve, the curvature of the nerve did not offer any advantage to reduce the MT; otherwise the curvature of the nerve helped to lower the stimulation to activate the nerve. The results showed that the MT of the curved nerve was (26.835 ± 0.039) mA, and the MT of the straight nerve was (30.117 ± 0.039) mA. Thus, the curvature of the nerve in the case of peripheral nerves had a significant influence in nerve activation for far field stimulation.

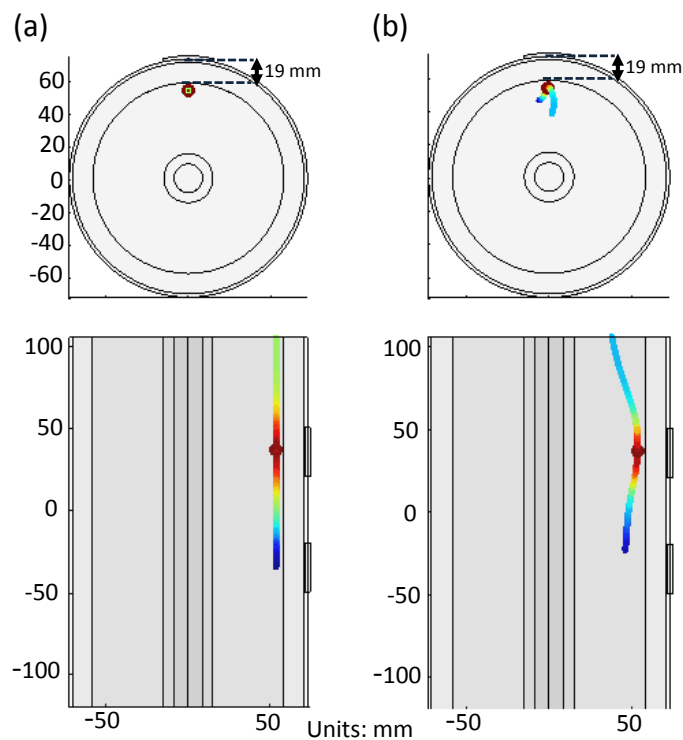


Figure 5.9: Influence of the curvature on the MT for a (a) straight nerve and (b) curved nerve of $15 \mu\text{m}$ using electrodes with area of 9 cm^2 . The closest point of the curved nerve was located under the electrode, as the most critical scenario, so the rest of the curved nerve was deeper than the straight nerve.

5.4 Discussion

Different parameters (electrode size, inter-electrode distance, and stimulation sites) that directly change the potential distribution within the tissues were selected to compare the MT calculated by the CM and PM. The comparison is made using AMs as reference (AM-R), which has been shown to have a potential distribution in agreement with

experimental data (73). The CM approximates MT better than the PM (Fig. 5.4) when its fat thickness is larger than AM. Evidence of this is that a targeted nerve requires higher MT in the PM than in the CM; consequently, the PM overestimates the MT of the AM-R (Fig. 5.6a). As the CM and PM are usually constructed with concentric cylinders and cubes (5, 41, 60, 82), the discrepancy of the fat thickness and bone location between the inspected models and the AM-R at each stimulation site could partly influence the activation error (Figs. 5.4 and 5.5). Thus, fat thickness and bone location were adjusted to match the average fat thickness and bone-to-muscle distance for the anterior and medial sites to observe whether the error could be reduced or not. Figure 5.10 shows that the activation error of the CM could be significantly reduced by only adjusting fat thickness (CMAdjFat) for the anterior and posterior sites. Furthermore, adjusting only the position of the bone (CMAdjBone) did not significantly reduce the error obtained by the CM. Even though the CM and PM had a high activation error (Fig. 5.4), this study showed that they could predict the tendency of nerve activation for studies of electrode size and inter-electrode distance variation similar to AM, as judged by the high cross-correlation between AM-R and CM or PM (Fig. 5.6). In addition, this result supports studies that use CM for electrode optimization (41, 60). Also, the electrical conductivities of the model tissues can be tuned to reduce the error (72, 76); nevertheless, the model needs to be retuned when simulation conditions change, such as stimulation site, inter-electrode distance, and electrode size. The omission of non-homogeneities can introduce misleading errors, as shown by Krasteva et al. (85) in a simulation study of peripheral nerve stimulation. However, they did not indicate which tissues should be considered or which could be neglected. Although the sciatic nerve trunk and blood vessel have an appreciable volume (blood vessel and sciatic nerve had an average of 16% and 6% of the bone size in our models, respectively), they are often omitted in studies of the thigh (4, 7, 60, 65, 82, 83, 84). Hence, AM-R was simplified into AM-(VN)' by omitting the sciatic nerve trunk and blood vessels tissues to inspect the MT variation. The sites closer to the omitted tissues are expected to have a larger prediction error: medial site for the blood vessel and posterior site for the sciatic nerve trunk. Figure 5.7 shows that the error at posterior site is larger in S1 and S2. In addition, the error in medial site is higher than in anterior and lateral for S2; however, the differences were not significant. Following that, the anterior and posterior sites are the most common stimulation locations for FES; the blood vessel and sciatic nerve

5. GEOMETRIC REPRESENTATIONS OF THE VOLUME CONDUCTOR ON NERVE ACTIVATION

tissues could be omitted without causing a significant increase in the error prediction of nerve activation for superficial muscles. Nerve activation also may be influenced by the targeted nerve's depth, because the electric field could change due to the presence or absence of inner tissues (e.g., nerves or blood vessels). The depth effect was inspected by locating the targeted nerves at different depths. Figure 5.8 shows an increase in the activation error prediction near the medial and anterior sites for AM-(VN)' because of the presence of the sciatic nerve and blood vessel. For simulation of deep muscles in the hamstring group, the AM should include the sciatic nerve; otherwise, the error increases from 7% to 22% for nerve activation near the sciatic nerve. In the case of the medial site, the error increased abruptly from 2.5% to 125% as the vessel (closer to medial site) has a larger volume than sciatic nerve (closer to posterior site). However, additional care should be pay in the curvature of the nerve because it was enough to reduce the MT for far field stimulation.

Human variability (shape, location, and electrical properties of the tissues) affects the MTs between different subjects. We were interested in the variability between model representations rather than human variability per se. Nevertheless, we can inferred from our results that the tendency of the nerve activation under different stimulation parameters holds for different model representations, even under different morphological variation of the tissues. Complex models might be necessary to better represent the human variability in fields such as the simulation study of transcranial magnetic stimulation and spinal cord stimulation. For instance, geometry of the brain (e.g., gyros) and posterior root fibers were characterized by strong curvatures and considerable conductivity variation between boundaries in the study of "hot spots" activation (9, 126). This should be further investigated, and in some cases, multi-resolution models could be used to trade-off the computation cost and prediction accuracy.

5.5 Conclusions

During the implementation of bioelectrical models, many assumptions and simplifications have been made. Although tissue geometry directly affects the electrical field, less effort has been spent to understand the cost of those simplifications and the circumstances where those assumptions are valid. This study was a contribution on the

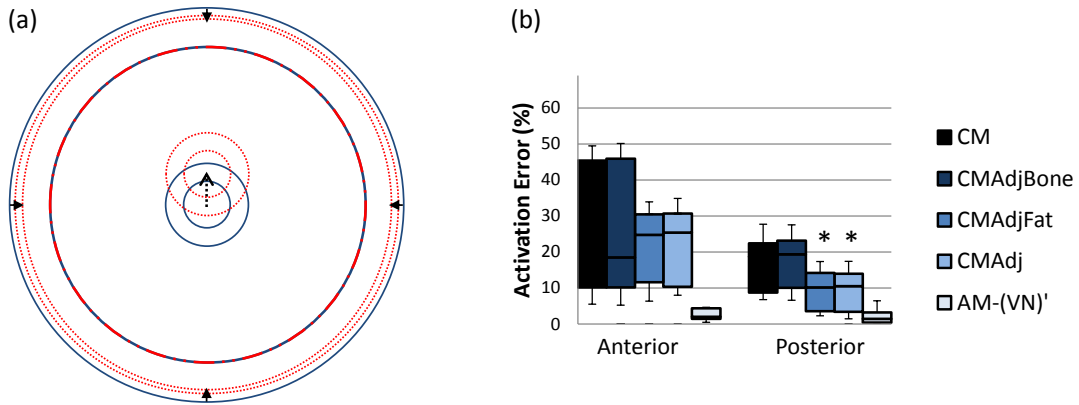


Figure 5.10: Optimization of CM geometry. (a) Fat thickness and bone location of the CM were adjusted separately (CMAdjFat, CMAdjBone) and together (CM-Adj) to match the average bone-to-muscle distance and fat thickness of AM-R for the anterior and posterior sites. Fat thickness was reduced 2.47 mm, and the bone was shifted upward 11.24 mm. (b) Activation error of the different models. * $p < 0.05$ (one-way ANOVA between models followed by Bonferroni post hoc test between CM and the other adjusted models, $N = 3$ per group). AM-(VN)' is shown as a reference (124).

evaluation of some common model simplifications on the computation of the nerve activation. For that, models such as the CM and PM were investigated, using an AM as reference. It was shown that even though they had a high error predicting the nerve activation, they could predict the tendency of the nerve activation for studies of electrodes optimization. Also, the error can be reduced by adjusting only the fat thickness corresponding to the stimulation site. In addition, the necessity of including the sciatic nerve trunk and blood vessels tissues was considered. Blood vessels and sciatic nerve should be taken into account in the model for studies of deep nerves, and they are optional for studies of superficial nerves. It is not necessary to include both tissues when stimulating the anterior and lateral sites. For future work, the same method presented here could be used to study the trade-off between computation cost and prediction accuracy of more complex tissues: curvature and path of the nerve fiber, boundaries between tissues, and electrical anisotropy.

Chapter 6

On the Dominance of the Tissues' Conductivity by Simulation Study and Human-Phantom Experiment

6.1 Overview

Variation of the dielectric properties of tissues could happen due to aging, moisture of the skin, muscle denervation, and variation of blood flow by temperature. Several studies used burst-modulated alternating stimulation to improve activation and comfort by reducing tissue impedance as a possible mechanism to generate muscle activation with less energy. Though, there is no consensus on which scheme and parameters have better force-generating capacity. Some researchers argued that by decreasing the impedance of the tissues the transfer of energy into the muscle increases, improving force.

The study of the effect of the dielectric properties of biological tissues in nerve activation presents a fundamental problem, which is the difficulty of systematically changing the morphological factors and dielectric properties of the subjects under study. Some studies have measured the current density distribution and transmission within the tissues, but the impedance reduction as a mechanism to improve force is still not clear. In addition, other studies have simulated the anisotropy and inhomogeneity

6. ON THE DOMINANCE OF THE TISSUES' CONDUCTIVITY BY SIMULATION STUDY AND HUMAN-PHANTOM EXPERIMENT

of the conductivity, showing that the conductivity can have a significant influence on the nerve activation by extracellular potentials. However, their models had some limitations: employment of point electrodes, muscle conductivity variation was omitted, and anatomical aspects were not considered in the geometry of the model.

This chapter tackles this problem by using a simulation and an experimental study. We investigated the effect of the conductivity of the tissues in muscle recruitment by implementing a 3D multi-layer thigh model coupled with a group of mammalian nerves that innervate a simplified semitendinosus muscle (ST). As a result, we made clear that skin impedance did not affect the recruitment and fat and muscle had a large influence on the muscle activation under normal operation conditions of the TES. The experimental study is a novel method that combines a fat tissue-equivalent phantom, with known and adjustable dielectric properties, with the human thigh. In this way, the dispersion of the tissue under study could be modified to systematically observe its effects in muscle activation. We found out that voltage and current stimulation have different behaviors for variation of the dielectric properties: current stimulation needs a larger magnitude to generate muscle activity for lower impedance, and voltage stimulation has increased nerve activation for lower impedance. The work presented here was published in (13).

6.2 On the dominance of the tissues' conductivity in muscle recruitment

6.2.1 Method

The activation given by the variation of V_e in a group of mammalian nerves innervating the ST was calculated by employing a compartment model. The values of the conductivity corresponded to the lowest, average, and highest for TES operating frequency range used in literature, Table 6.1. The values of the permittivity were set at constant value corresponding to 100 Hz as that as its variation is not significant in recruitment (76).

The following parameters were employed: skin (0.15 cm), subcutaneous fat corresponding to the ST (1.20 cm), thigh muscle (5.06 cm), including the ST, bone (0.60 cm), and bone marrow (0.76 cm). The cylindrical dimensions were obtained from cross section areas of MRI data for an average thigh (106, 107). The electrical conductivity for the tissues was assumed isotropic except for the muscle, which has a transversal and longitudinal conductivity. Square electrodes were modeled with an area of 20.25 cm² (4.50 cm × 4.50 cm) and separated by an inter-electrode distance of 6.00 cm. A cathodic square stimulus of 40 mA, 80 mA, 120 mA, 160 mA, and 200 mA and pulse width of 0.5 ms were employed for the simulation.

Table 6.1: Electrical parameters of the tissues and dimensions

Tissue Layer	Lowest Con- ductivity (10 ⁻⁴ S/m)	Average Conductivity (10 ⁻⁴ S/m)	Highest Con- ductivity (10 ⁻⁴ S/m)	Relative Permittivity
Skin	1.66	4.61	210.00	45 297.63
Fat	16.66	406.40	1000.00	151 523.28
Muscle (transversal)	666.67	666.77	2000.00	9 329 044.64
Muscle (longitudinal)	2455.00	2667.10	6666.70	9 329 044.64
Bone Cortical	160.00	200.60	250.00	5852.76
Bone Marrow	660.00	1013.30	1020.00	72 458.81

6. ON THE DOMINANCE OF THE TISSUES' CONDUCTIVITY BY SIMULATION STUDY AND HUMAN-PHANTOM EXPERIMENT

6.2.2 Simulation results

Effect of the conductivity in all tissues

Three models with different conductivities were investigated. The conductivities of the tissues of the low conductivity model (LC Model) and high conductivity model (HC Model) were set to the lowest and highest values, following Table 6.1. The conductivity values of the standard model (SM) were the average of common values in literature. The results showed that LC model exhibited higher recruitment than HC model. Also, SM model and LC model presented similar recruitment, as shown in Fig. 6.1 (13).

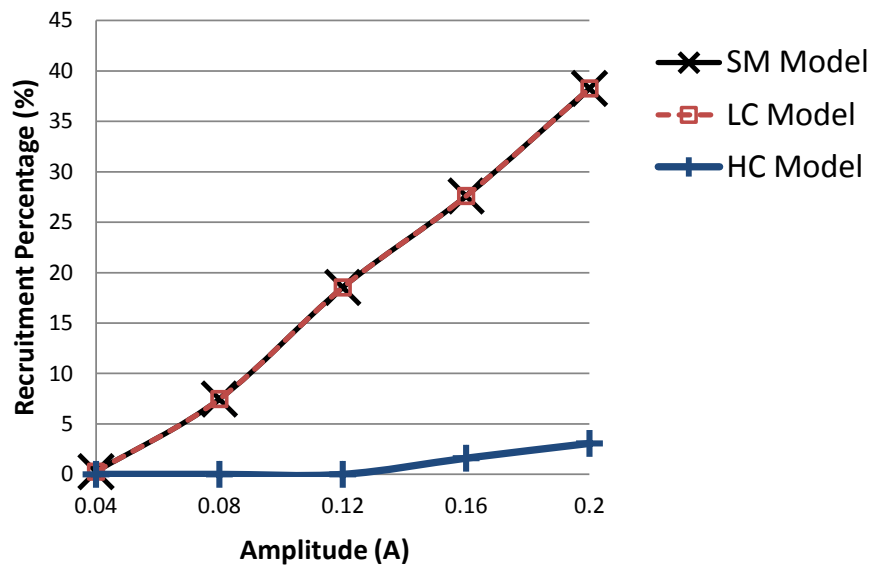


Figure 6.1: Recruitment of three models with different conductivity configurations

Dominance of the conductivity by tissue on the recruitment

The overall recruitment of the model was studied in the simulations for each tissue to determine how significant is the change of conductivity, Fig. 6.2 (13). Models with different conductivities were employed: 1) SM-LC fat, SM-LC skin, and SM-LC muscle had the same conductivities of the SM model with the conductivity of the tissue under inspection set to the lowest value. 2) SM-HC fat, SM-HC skin, and SM-HC muscle had tissue's conductivity under study set to highest values.

6.2 On the dominance of the tissues' conductivity in muscle recruitment

From Fig. 6.2, it is possible to observe that the recruitment was within two limits given by the LC model (upper limit) and the HC model (lower limit). Also, the recruitment of the SM-LC fat model was higher than SM-HC fat model (i.e., the recruitment decreased when the conductivity of the fat layer increased). Thus, the recruitment could be near the upper limit by only modifying the conductivity of the fat layer to lowest (SM-LC Fat). Furthermore, there was no difference between the recruitment of the lowest skin conductivity in the SM-LC model and the highest skin conductivity values in the SM-HC skin model. Lastly, the recruitment of the SM-HC muscle model was lower than SM-LC muscle model. As a result, the fat's conductivity was a key point to increase recruitment, and muscle's conductivity was dominant in reducing recruitment.

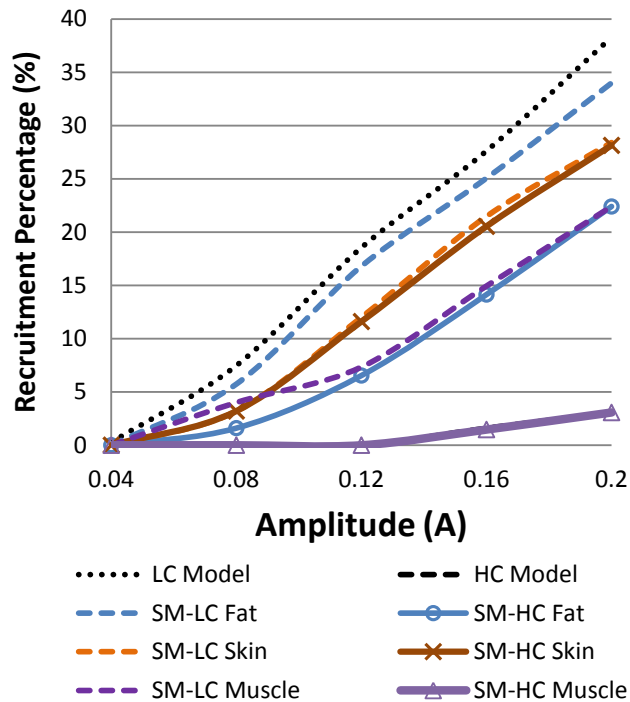


Figure 6.2: Comparison of the recruitment percentage between models to determine the conductivity dominance by layer. SM-TissueName had the similar electrical properties as the SM but with the conductivity of the respective tissue under study set to lowest or highest value.

6. ON THE DOMINANCE OF THE TISSUES' CONDUCTIVITY BY SIMULATION STUDY AND HUMAN-PHANTOM EXPERIMENT

Conductivity sweep for each tissue

The effect of the conductivity change of each tissue layer was further investigated by sweeping the conductivity between the lowest and highest values, Fig. 6.3. Recruitment kept almost constant for the skin's conductivity variation. The maximum recruitment change was 8.4% at 120 mA, and 4.9% and 1.4% for a stimulation of 160 mA and 200 mA, respectively. In the case of the conductivity sweep of the fat layer, the maximum recruitment occurred very near the minimum conductivity. The recruitment decreased steadily until a percentage of 61.4%, 44.9%, and 39.1% of its original maximum value, at an intensity level of 120 mA, 160 mA, and 200 mA, respectively. Accordingly, the maximum recruitment change was reduced as current increased. The recruitment vs. the conductivity difference was simulated for the muscle layer as well, resulting in a large influence. In contrast to skin and fat layer, muscle conductivity was represented by a difference between longitudinal and transversal component.

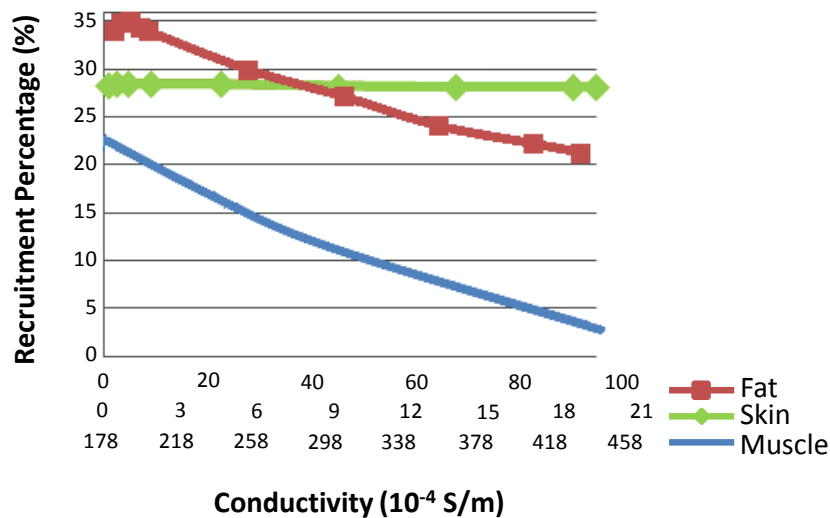


Figure 6.3: Recruitment vs. conductivity of skin, fat, and muscle layers at 200 mA.

6.2.3 Discussion

This study presented a simplified model of semitendinosus muscle to study the influence of the conductivity on the recruitment. Myelinated axons were located randomly at

6.2 On the dominance of the tissues' conductivity in muscle recruitment

different depths and parallel with each other within the endplates zone (band shape) at the middle of the muscle (96, 127). The distribution of the nerve axons was based on a sciatic nerve bimodal configuration of a cat with peaks at 6 μm and 12 μm (108). In other study (128), the sciatic nerve of a mouse had peaks at 3 μm and 7 μm . This difference may have an effect on the recruitment-duration curves; thus the sciatic nerve distribution of the cat was chosen because its muscles were more comparable with human muscle's size in the present study.

A duration time for the stimulus pulse of 0.5 ms was selected, which was larger than the stimulation time for plateau recruitment, shown in Fig. 3.12. However, the recruitment curve given by this model should be calibrated to correspond with experimental data by matching the geometry of the layers and modifying the electrical parameters (conductivity). This study employed models with different conductivity parameters to investigate the effect of the conductivity on the muscle activation. The conductivity parameters, for normal conditions, were obtained from experimental data.

More energy transferred to the nerves axons using higher conductivity would be expected. However, the simulations indicated the contrary (Fig. 6.1). A lumped model of the fat and muscle tissues is used to explain the results of the simulations without considering the capacitive properties, as shown in Fig. 6.4a. Firstly, the lumped model can be simplified for current stimulation by omitting the R_{FatL} . Then, the lowest and highest conductivities in the present study are replaced in the lumped model, Fig. 6.4b. As a result, the fat layer's impedance is higher than the muscle's impedance in the case of the lower conductivity; and the impedance of the fat and muscle layer are similar in the case of higher conductivity. Hence, the model with higher conductivities has less energy reaching the muscle than lower conductivity (i.e. lower recruitment). Petrosfky et al. (70) obtained experimentally that the subcutaneous fat's resistance was almost an order of magnitude higher than that of muscle and skin, which corresponds to our parameters for lowest conductivity in the lumped model. Also, transfer of current through the tissues was investigated to compare the efficiency between different waveforms (69, 70). Their results showed that more force is produced when more current was reaching the muscle for any stimulation schemes: interferential, sine or square stimulation. However, there are no experimental studies that investigate the role of tissues' conductivity in the recruitment because of the complexity of isolating

6. ON THE DOMINANCE OF THE TISSUES' CONDUCTIVITY BY SIMULATION STUDY AND HUMAN-PHANTOM EXPERIMENT

the effect of each tissue and comparing the same tissues with different conductivity values *in vivo*.

Section 6.2.2 studied the dominance of each tissue layer by isolating the conductivity variation for only one tissue. The simulations showed that the change of skin layer's conductivity did not modify muscle recruitment while the change of fat and muscle did, as shown in Figs. 6.2 and 6.3. Other studies have reported that skin impedance is highly affected by external factors: sweat, temperature, gel of the electrode, etc (67). The results of present study indicated that these variations in the skin impedance actually did not play an important role in muscle recruitment under the conductivity values reported in normal conditions. Though, the presented model of the skin did not take into account inherent non-linearity, caused by pores etc. Additionally, there are no available experimental studies that relate the change of skin impedance with force production to validate or reject the hypothesis of the skin influence.

In contrast to the skin layer's conductivity, fat conductivity significantly influenced recruitment. In addition to the influence of fat thickness in the stimulation (12), an increment of fat's conductivity up to the highest value decreased the recruitment, without reaching the lower limit (HC model), as shown in Figs. 6.2 and 6.3. A similar result was observed with the muscle layer, higher conductivities decreased the recruitment to the lower limit. Also, the change of recruitment over the change of conductivity was higher for the fat (e.g., 1076.93 at 16 mA) than the muscle (e.g., 350.97 at 16 mA); thus, a smaller change of fat's conductivity was more significant than the muscle. Furthermore, higher current intensities reduced the effect of the conductivity variation in the muscle because more fibers being stimulated over their threshold values. Ahad et al. (129) investigated the alteration of the muscle's conductivity after neurogenic injury, showing that the difference between the longitudinal and transversal conductivities increased (with longitudinal increasing more than the transverse) for a frequency lower than 10 kHz, and the crush muscle had a higher transversal and longitudinal conductivity than the normal one, which indicates less recruitment according to our model results and the loss of functionality of the muscle itself. Consequently, muscle and fat layer should be carefully selected in a model simulation to account for the electrical properties and fat thickness variation resulted from muscle denervation and obesity.

Livshitz et al. (87) simulated the effects of the conductivities of different layers in the current density within the muscle; however, the exact location inside the muscle

6.2 On the dominance of the tissues' conductivity in muscle recruitment

was not indicated. They showed that the current density decreased around 15% of the maximum by cause of fat's conductivity. Also, skin conductivity had a large effect in force production near 40%, contrary to the results of the present study. However, the range of conductivity values used in our simulations corresponds to the optimal conductivities range, which corresponded to only 5% of their range.

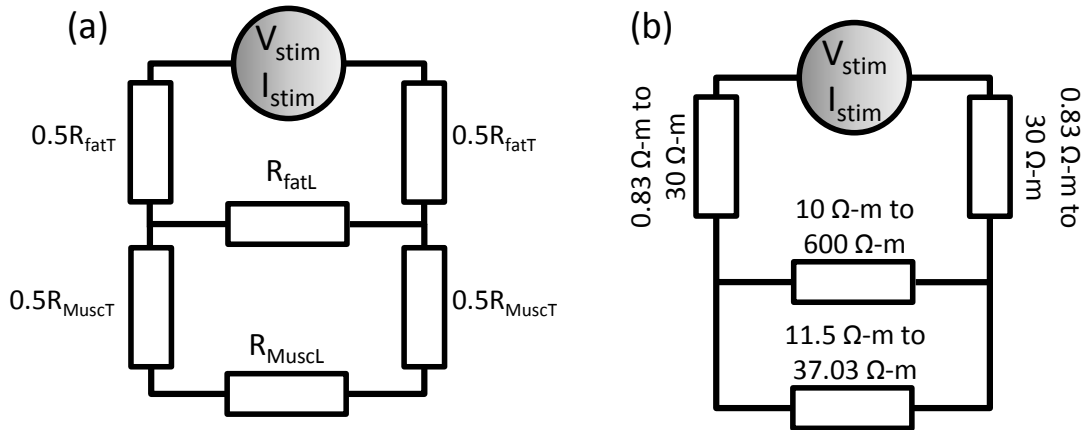


Figure 6.4: Lumped model. (a) Lumped model of the cylindrical model without considering the capacitive effects, (b) lowest and highest conductivities. R_{FatT} , R_{FatL} and R_{MusclT} , R_{MusclL} referred to the transversal and longitudinal impedance of the fat and muscle layer, respectively (13).

One application of the results of this study to improve TES is to modify the tissue conductivity. Some previous studies (45, 47) had shown that more energy was transferred to muscle and more force was produced at low frequency schemes (sine and square) than high frequency (Russian and interferential stimulation) for current stimulation. As argued in (43), skin impedance depends on the phase duration rather than the pulse frequency. Thus, if a low frequency pulse current has the same phase duration as a kilohertz-frequency signal, the impedance of the tissue is the same for both stimulation waveforms (43, 44). Therefore, it is still not clear whether by using frequency or pulse duration, the electrical properties can be used to improve force production; however, our model suggested that conductivity is an important factor and should be taken into account, at least, as parameters in the model simulations.

6. ON THE DOMINANCE OF THE TISSUES' CONDUCTIVITY BY SIMULATION STUDY AND HUMAN-PHANTOM EXPERIMENT

6.2.4 Conclusions

This study presented a simplified model of the semitendinosus muscle to assess the influence of the electrical properties of the tissues in muscle recruitment. The results showed that by using current stimulation the electrical configuration of the tissues with lower conductivity had higher recruitment, which was confirmed by using a lumped model. However, the skin conductivity did not have an important influence in the muscle activation in contrast to the muscle and fat layer. Consequently, fat layer and muscle layer should be carefully considered at least in simulation models because of their possible variability resulted from obesity (fat thickness) and electrical properties (muscle denervation).

6.3 Human-phantom experiment to study the variation of the dispersive dielectric properties on the tissues

6.3.1 Method

Experimental study

Eleven healthy subjects (age 23.7 ± 3.4 , height 174.3 ± 5.7 cm, weight 65.9 ± 10.9 kg, BMI 21.7 ± 3.2 , mean \pm SD) participated in the study. All subjects were informed of all experimental procedures and signed a statement of informed consent as approved by Chiba University.

In order to analyze the effect of the conductivity variation of the tissues in muscle recruitment, a semicircular fat-equivalent phantom, coupled with a human thigh, was used to mimic a variable tissue's conductivity during nerve activation as explained in detail in section 3.5.3. The area between the interfaces was cleaned, and we verified that the interface between two phantom tissues produced similar results.

A monophasic voltage-controlled and current-controlled stimulation was employed with a square pulse of $250 \mu\text{s}$ using a purpose-built device for voltage stimulation and a Trio 300 device (ITO Co., Ltd, Tokyo) for current stimulation. The duration of the stimulation pulse was chosen to be small enough to introduce high harmonics, to take into account the dispersion effect of the tissues, and because it is commonly used in electrical stimulators. 99 % of the power spectral density of the pulse signal is reached at 41 kHz for a bandwidth of 100 kHz, which shows that the frequency response of the

6.3 Human-phantom experiment to study the variation of the dispersive dielectric properties on the tissues

phantom covers the spectrum of the pulse. Stimulation voltage ranged between 17 V and 73 V and the stimulation current between 7 mA and 46 mA to generate muscle activation in the different experiments.

Simulation study

Two configurations for the model morphology were considered to model the thigh (Fig. 6.5): 1) a cylindrical model (CM), composed of skin (0.20 cm of radial thickness), fat (1.24 cm), muscle (4.32 cm), cortical bone (0.63 cm), and bone marrow (0.87 cm), was used; 2) a fat-equivalent phantom (0.85 cm) was added to the CM in a similar configuration to the human-phantom coupling experiment regarding the geometry and dielectric properties of the fat-equivalent phantom and human thigh (CMCoupling). Square electrodes were modeled with an area of 25 cm² separated by an inter-electrode distance of 3 cm and 7 cm from edge-to-edge. A monophasic voltage and current stimulation with a 250 μ s square pulse was simulated to investigate the effect of the dispersion variation.

Dielectric properties of the body tissues were dispersive and isotropic for all tissues with the exception of the muscle tissue, which was considered anisotropic (transversal and longitudinal conductivities). The dispersion was obtained from the works of Gabriel et al. (92, 117) for the human tissues and our measurements of dispersion of the phantom tissues. One straight myelinated fiber, 63 mm in length, was placed under the center of the electrode to investigate its motor threshold (MT).

6.3.2 Results

Human-phantom coupling experiment and simulation

Figure 6.6 shows the normalized MT using three different fat-equivalent phantoms for the human-phantom coupling experiment and simulation (CMCoupling). Figure 6.6a shows that MT is higher for the higher conductivity dispersion of the fat-equivalent phantom in current stimulation. On the contrary, Fig. 6.6b shows that MT is lower for higher conductivity dispersion in the case of voltage stimulation. The simulation results were congruent to the human-phantom coupling experiments.

6. ON THE DOMINANCE OF THE TISSUES' CONDUCTIVITY BY SIMULATION STUDY AND HUMAN-PHANTOM EXPERIMENT

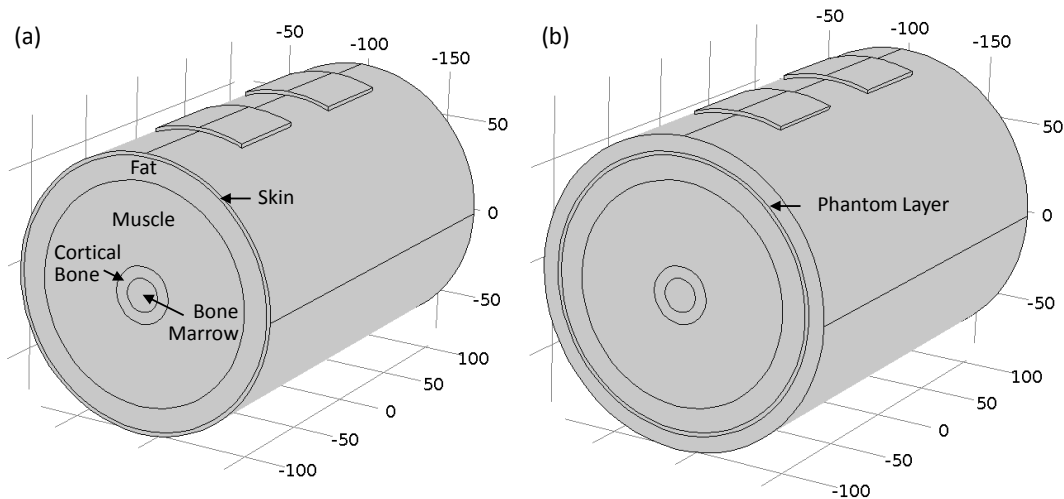


Figure 6.5: Geometry representation by concentric cylinders. (a) cylindrical model (CM) and (b) human-phantom coupling simulation (CMCoupling). Models are composed of bone marrow, cortical bone, muscle, fat, skin, and fat-phantom (only for b) from inner to outer cylinders.

Effect of the inter-electrode distance

Variation of the inter-electrode distance can affect the impedance seen from the electrodes that may influence the result of the human-phantom coupling experiment. Figure 6.8 shows no difference with respect to the trend in Fig. 6.6.

Simulation considering a larger dispersion variation

A larger dispersive variation than the experimental set-up was considered in order to observe its effect on muscle activation. Two different simulations were investigated: 1) variation of the dispersion of all the tissues by a scaling factor of the dielectric dispersion of the CM, from 0.5 to 8, and 2) variation of only the dispersion of the fat tissue by the same scaling factor in the CM. Figure 6.8 shows that the MT increased for both cases during current stimulation; MT first decreased and then increased during voltage stimulation.

6.3.3 Discussion

This study employed tissue-equivalent phantoms with different conductivity values to explain how variation of the dielectric properties of tissues might affect muscle re-

6.3 Human-phantom experiment to study the variation of the dispersive dielectric properties on the tissues

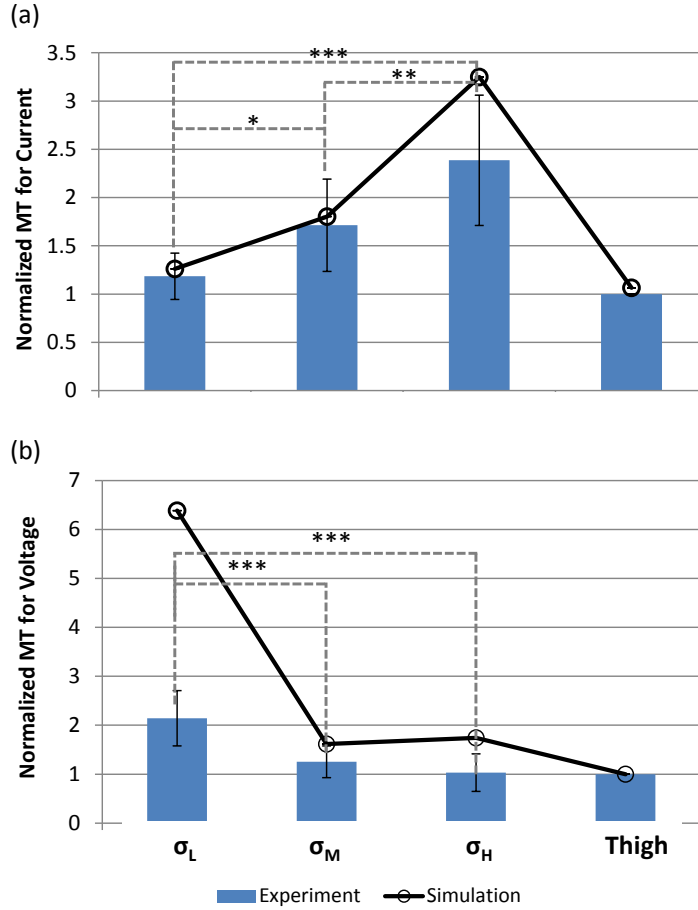


Figure 6.6: Normalized MT using fat-equivalent phantom with three different conductivities for the human-phantom coupling experiment and simulation. (a) Current simulation and (b) voltage stimulation (N=11, 3 cm of inter-electrode distance, MT of the thigh is the reference for normalization). * $p < 0.05$, ** $p < 0.01$, and *** $p < 0.001$ (One-way ANOVA followed by a Tukey-Kramer post hoc test).

recruitment during current and voltage stimulation. Petrofsky et al. (68) showed that increasing conductivity by skin blood flow resulted in higher MT for current stimulation. In addition, impedance could be altered by muscle denervation and obesity, as shown by Ahad et al. (4). Our hypothesis is that the effect of the impedance variation (positive or negative) on muscle activation depends on the stimulation type: voltage-controlled or current-controlled stimulation. In this study, a human-phantom coupling experiment was designed to observe the effect of dielectric dispersion variation in human muscle recruitment.

6. ON THE DOMINANCE OF THE TISSUES' CONDUCTIVITY BY SIMULATION STUDY AND HUMAN-PHANTOM EXPERIMENT

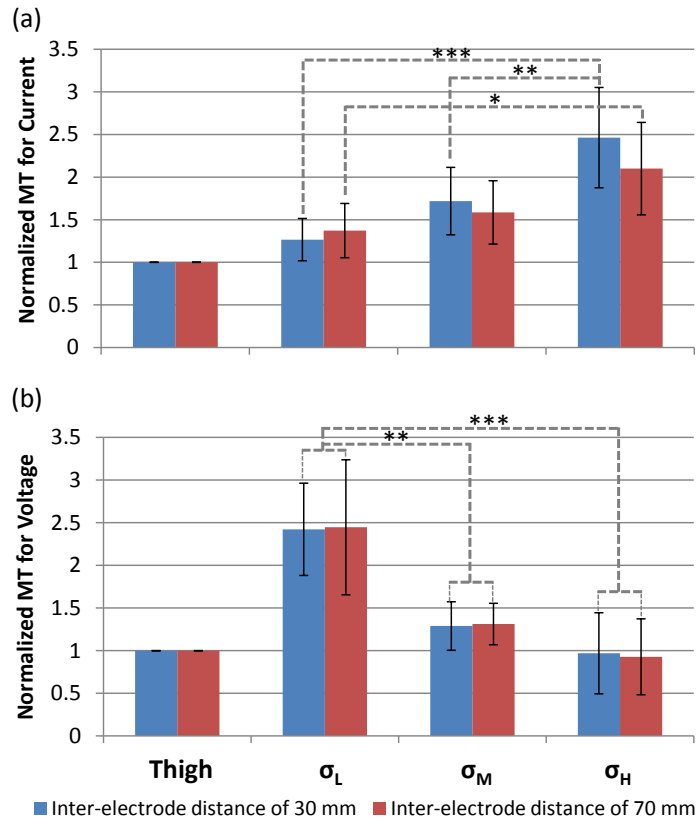


Figure 6.7: Effect of the inter-electrode distance in the human-phantom coupling experiment. (a) Current stimulation and (b) voltage stimulation. (N=6). *p<0.05, **p<0.01, ***p<0.001 (One-way ANOVA followed by a Tukey-Kramer post hoc test).

Figure 6.6a showed that the fat-equivalent phantom with higher conductivity had a higher MT during current stimulation, though more energy would be expected to be transfer to the nerves axons for lower impedance. In the case of voltage stimulation, Fig. 6.6b presents the opposite result to current stimulation. The simulations were in agreement with the results of human-phantom coupling experiment. In addition, the validity of the coupling between phantom and thigh was also indirectly supported by the fact the MT of the thigh experiment was similar to the human-phantom coupling experiment using a low impedance (lower voltage drop in the phantom) and high impedance (lower longitudinal current only flowing through the phantom) during voltage and current stimulation, respectively.

A wider variation of the dispersion was considered in the simulation in Fig. 6.8, where the same tendency of the experimental study was obtained in the simulation of

6.3 Human-phantom experiment to study the variation of the dispersive dielectric properties on the tissues

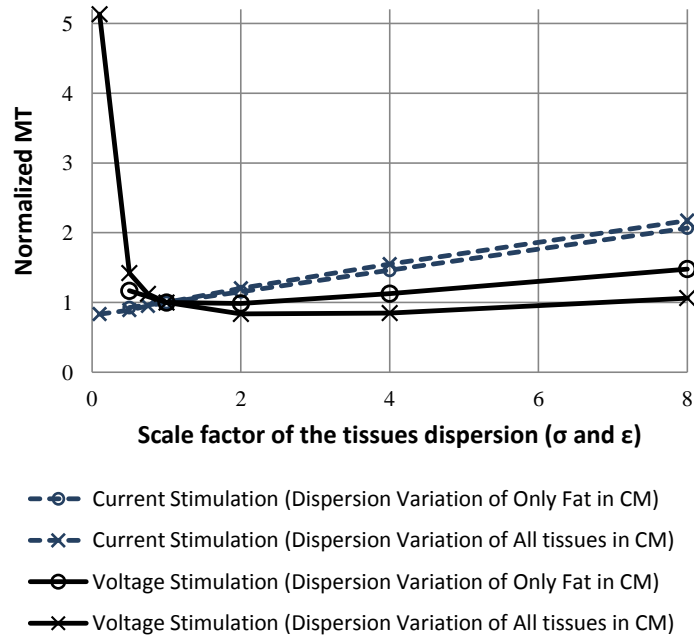


Figure 6.8: Simulation of the dispersive conductivity variation for current and voltage stimulation. Dispersive conductivity data (117) was scaled from 0.5 to 8 using two configurations: variation of the dielectric dispersion of all tissues and variation of only the fat tissue's dispersion.

the current stimulation. In the case of voltage stimulation, the MT first decreased and then increased for higher dispersive conductivities (after-increment effect); therefore, a future experimental study should investigate higher variations to verify this effect. In addition, as the inter-electrode distance may affect the amount of lateral and transversal current in tissues, its effect on the MT was investigated using inter-electrode distances of 30 mm and 70 mm. As a result, its variation didn't show any significant difference, as shown in Fig. 6.7.

The experimental and simulation results can be understood by simplifying the analysis of the fat layer's impedance as a resistor as Fig. 6.4. In the case of the current stimulation, a lower conductivity of the fat generates more current crossing directly to the thigh with small transversal currents in the fat layer; if conductivity of the fat increases, more transversal current will flow through the fat layer without going inside the muscle, and consequently, the MT increases. In the case of voltage stimulation, a lower conductivity has higher MT because more voltage drops at the fat layer and MT increases; if the conductivity increases, more voltage drops in the muscle layer and

6. ON THE DOMINANCE OF THE TISSUES' CONDUCTIVITY BY SIMULATION STUDY AND HUMAN-PHANTOM EXPERIMENT

MT reduces. If we, however, continue increasing the dispersive conductivity, the fat tissue behaves as a short circuit and increases the MT again. Analytically, the ratios V_{muscle}/V_{stim} and I_{muscle}/I_{stim} were calculated for voltage and current stimulation to predict the effect of the resistance of the fat layer on the muscle layer, Fig. 6.9. As a results, a lower resistance of the fat (higher conductivity) increases the voltage and decreases the current for voltage and current stimulation, respectively. Therefore, a lower MT for voltage stimulation and a higher MT for current stimulation are expected for higher fat conductivity, as the experimental results. Appendix B has the detail of the equation employ for these results.

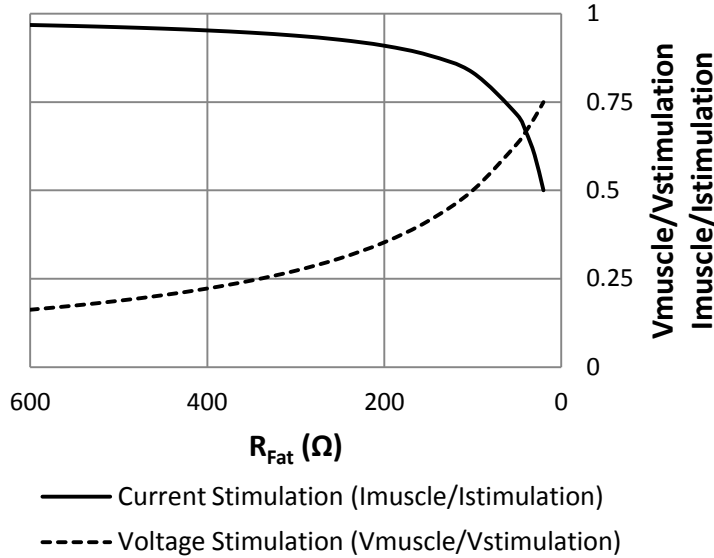


Figure 6.9: Effect of the current and voltage stimulation using the lumped model. $R_{FatL} = 600 \Omega m$ to $20 \Omega m$, $R_{FatT} = R_{FatL}/6$, $R_{Muscle} = 20 \Omega m$.

An increment of the conductivity of the electrode's hydrogel during the experiment was noticed by Copper et al. (82) during a long period of electrode usage. This variation offers an additional explanation for the attenuation (no after-increment effect) of the MT during voltage stimulation for larger dispersive conductivities in the human-phantom coupling experiment. The simulation in Fig 6.10 shows that the MT decreased for higher electrode conductivities; the combined effect showed an attenuation of MT for higher conductivities of the phantom-tissue during voltage stimulation.

Regarding the role of impedance and frequency of the stimulation waveform, currents in the kilohertz frequency (BMAC) range is related to the role of the impedance

6.3 Human-phantom experiment to study the variation of the dispersive dielectric properties on the tissues

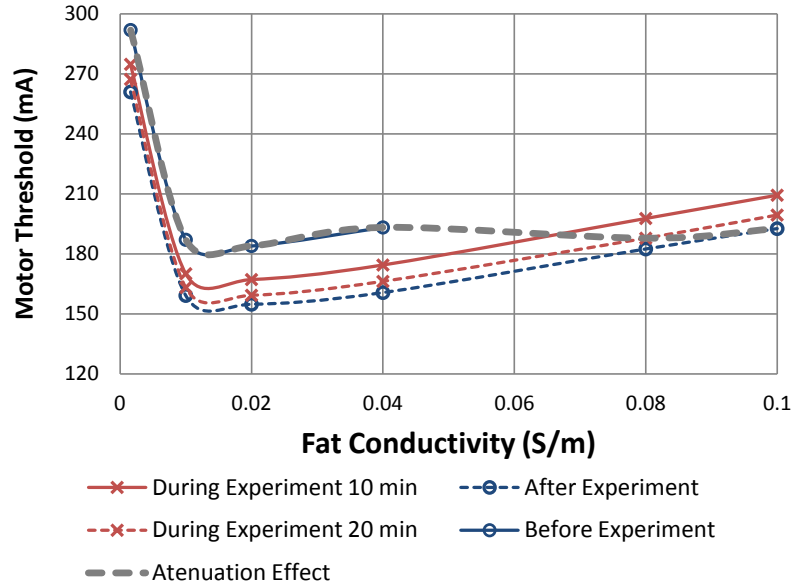


Figure 6.10: Simulation of the effect on the MT of the dispersion of the electrodes during the experiment. The dispersion of the electrodes is modified during the stimulation duration. The attenuation effect is similar to the human-phantom experiment during voltage stimulation.

in the energy penetration into the muscle. In the case of PC and BMAC stimulation, the impedance depends on the phase duration rather than the pulse frequency; thus, there is no advantage of BMAC over PC from the point of view of impedance variation if they have the same phase duration. The disadvantage of high frequency stimulation is that the absolute refractory period of the sarcolemma is exceeded so no new AP can be evoke for the muscle fibers (130). However, there are some mechanisms that explain the function of BMAC: threshold voltage decreases in accordance with an increase in the number of alternating current cycles per burst as determined by the burst duration (Gildemeister effect) (48). In our study, we observed that the voltage stimulation and current stimulation had different transfer functions; consequently, their phase duration would have different effects in the muscle activation. The voltage distribution in the muscle will be given by the transfer function that depends on the geometry, dielectric properties of the tissues, location, and frequency. The transfer function (Fig. 6.11) is a low-pass filter for current stimulation and band-pass filter for voltage stimulation. For PC stimulation, long pulses will have a larger voltage output for current stimulation and shorter pulses will have a higher voltage at the muscle for current stimulation. Pet-

6. ON THE DOMINANCE OF THE TISSUES' CONDUCTIVITY BY SIMULATION STUDY AND HUMAN-PHANTOM EXPERIMENT

rosfky et al. (45, 47) showed that sine wave stimulation produced significantly greater force and more comfort than square waveform, which was better than BMAC stimulation as demonstrated by the higher current transmission of the sine wave following the square wave and then the BMAC due to the low-pass filter given by the transfer function of the impedance using current stimulation.

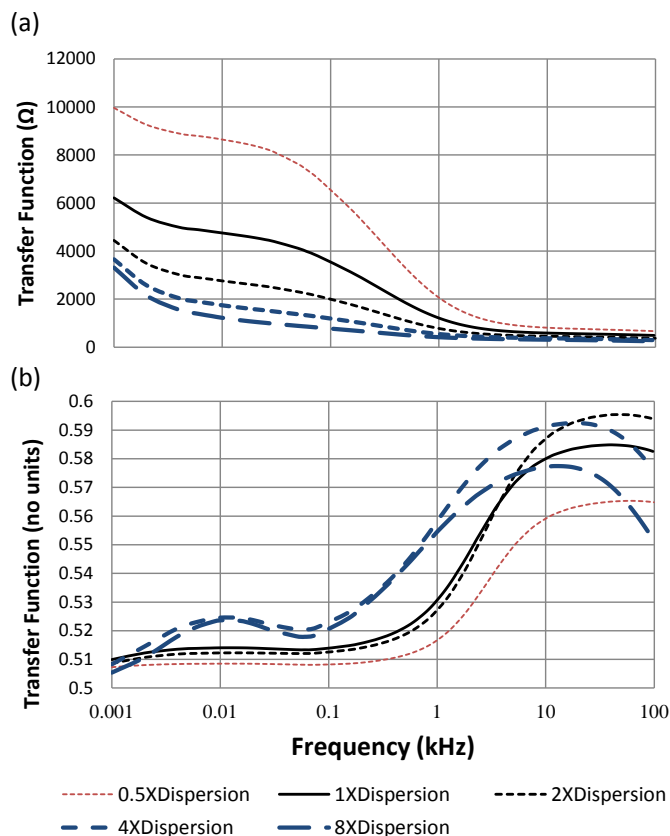


Figure 6.11: Transfer functions for (a) current and (b) voltage stimulation using an unitary voltage and current magnitude.

Long pulses (low frequency) have a larger voltage at the muscle for PC current stimulation, and shorter pulses (high frequency) have a higher voltage at the muscle for PC voltage stimulation. Petrosfky et al. (45, 47) also showed the low-pass filter of the transfer function during current stimulation, where PC (low frequency) was better than BMAC. However, there is no advantage of BMAC over PC from the point of view of impedance variation if they have the same phase duration. The disadvantage of high frequency stimulation is that it exceeds the absolute refractory period for the

6.3 Human-phantom experiment to study the variation of the dispersive dielectric properties on the tissues

sarcolemma (130). However, there are some mechanisms that explain the function of BMAC: threshold voltage decreases in accordance with an increase in the number of alternating current cycles per burst as determined by the burst duration (Gildemeister effect) (43).

6.3.4 Conclusions

The present study shows that the effect of the dielectric tissue variation behavior on muscle activation differs between voltage and current stimulation. The simulation and experimental studies showed that current stimulation needs a larger stimulation magnitude to generate muscle activity for lower impedance, which contradicts the studies that claimed that lower impedance increases the voltage transmission to the muscle. Voltage stimulation needs a lower MT for lower impedance; however, the simulation also showed that a larger increment of the dispersive dielectric properties of the tissues can increase its MT. Considering only the effect of phase duration under the same dispersive tissues using PC stimulation, a long pulse has a larger voltage output during current stimulation, and a shorter pulse has a higher voltage at the muscle during voltage stimulation, from the point of view of the impedance variation.

Chapter 7

Role of the fat thickness and electrodes

7.1 Overview

The physiological responses to different stimulus parameters, such as number of pulse repetition rate, current or voltage pulses, monophasic or biphasic stimulus, have been studied before (52, 131, 132). The waveform is mainly chosen for better selectivity and efficiency of energy transmission along depth direction (depth efficiency). A better depth efficiency contributes to a less energy loss through the path from the electrodes to the nerve. Energy loss refers to the energy that spreads to unwanted target regions.

The objective of this chapter is to investigate the effect of current density, fat thickness, frequency, inter-electrode distance, electrode area, and electrode shape in nerve activation. The work presented here was published in (12, 42).

7.2 Current density study

First, a 2D model was considered to inspect the effect of the tissues on the transmission of current from superficial electrodes until the muscle. Current densities beneath a stimulating electrode can be highly nonuniform and severe burns may occur. These current nonuniformities depend on a number of factors including electrode placement, quality and uniformity of the electrode-skin interface, and effective electrical and thermal conductivities of the tissue immediately beneath electrode contact (59).

7.2.1 Parameters

A multiple-layer geometry was developed in a 2D (parallel) model. The dielectric parameters were defined for each layer as an isotropic medium and frequency independent. The electrodes were modeled as a 1 mm electrode-skin thickness and 5 cm of length. The pair of electrodes were put on the skin separately by a distance of 4 cm. In addition, the external corners of the electrodes were rounded to reduce singularities in the solution. A current stimulation with amplitude of -100 mA (a monophasic square pulse of 1 ms) and fat thickness (5 mm to 60.0 mm) were selected, Table 7.1.

Table 7.1: Parameters to study the transmission of current

Parameter	Value
Electrode shape	Square (5 cm of length)
Current	-100 mA(monophasic), 1 ms
Inter-electrode distance	4 cm
Fat thickness	5 mm to 60 mm

7.2.2 Results

The y-component of current density was computed at the boundaries between each two layers (electrode-skin, skin-fat, fat-muscle) for 2 thickness (2 cm and 5 cm), presented in Fig. 7.1 (12). Current density at the electrode-skin and skin-fat boundary has a similar distribution. However, the current density at the fat-muscle boundary presents a reduction in amplitude and a larger distribution of the current outside the area under the electrodes when fat thickness increases.

For different fat thickness values (5 mm to 60 mm), the ratio of current density at each boundary between tissues to the total input current was computed, shown in Fig. 7.2 (12). The current density at the boundaries of the electrode-skin (not presented in the Fig. 7.2) and skin-fat are almost constant; in contrast, the fat-muscle boundary is influenced directly by fat thickness.

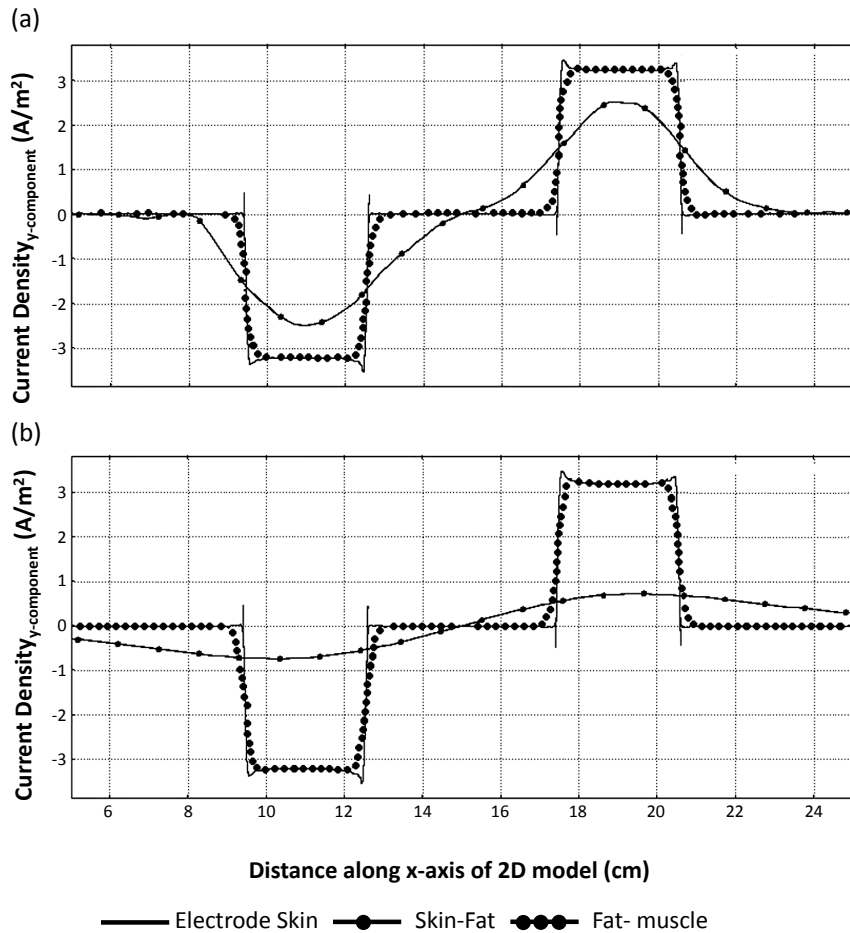


Figure 7.1: Current density at the boundary between different tissues. Current density at the boundary of the electrode-skin, skin-fat and fat-muscle at a fat thickness of (a) 1 cm and (b) 5 cm. Larger fat thickness brings a major dispersion in the current density.

7. ROLE OF THE FAT THICKNESS AND ELECTRODES

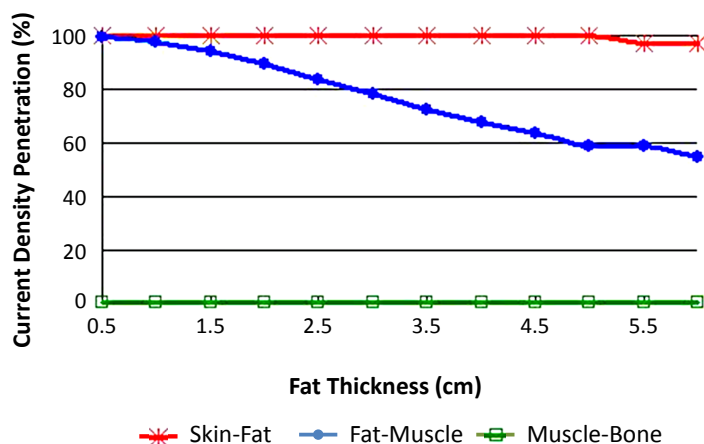


Figure 7.2: Percentage of the total input current density at the boundaries between the tissues. Percentage of current density at the skin-fat, fat-muscle and muscle-bone for different fat thickness (0.5, 1, 1.5, 2, 2.5, 3, 3.5, 4, 4.5, 5.5 and 6 cm).

7.2.3 Discussion and conclusion

A 2D isotropic model was considered first for its simplicity to study the effect of the tissues on the transmission of current down to the muscle. In this study, the y-component of the current density was analyzed to evaluate its penetration, and the fat thickness was included to evaluate its high variability in the thigh.

We observed that there are four peaks of the current distribution in the electrode-skin boundary corresponding to the position of the borders of the electrodes, as shown in Fig. 7.1. This non-uniformity of the current density has been reported before and may cause tissue damage or discomfort (133). Nevertheless, it may be due to singularities in the model produced by sharp edges formed by the electrode and the skin in the model; consequently, the edges of the electrodes with the skin were rounded to avoid the singularities. According to the simulation, the possibility of tissue damage is at the level of the skin layer, and these peaks are attenuated in the fat and muscle layer.

Livshitz (87) states that under constant current conditions, fat prevents the lateral spread of current from the electrode, forcing the current to flow along the shortest path, i.e., across the thickness of the fat layer. On the other hand, muscle tissue is a better conductor than fat, therefore allowing the current to spread laterally from the electrode. But, according to Fig. 7.3, the fat layer do not impede the lateral spread of

current from the electrode. Additionally, the increase of fat thickness increments the lateral current under the region beneath the electrode.

Clearly, fat thickness affects the current density that enter the muscle; thus, activation of the muscle, Fig. 7.1. According to Fig. 7.2, the current density showed a reduction of 45% at the fat-muscle boundary at 60 cm of fat thickness. However, muscle activation is not proportional to current density; therefore, a nerve model is necessary to study the nerve activation.

Moreover, the current density would change considerably in a 2D model compared with a 3D model because the current may be passed on to the muscle behind the bone without passing through the bone. Additionally, functional tetanic contraction of the quadriceps influenced by the co-contractions of the hamstrings can be investigated (134).

A 3D model of the thigh coupled with a 1D nerve model is used in the following sections to evaluate the underlying parameters of stimulation.

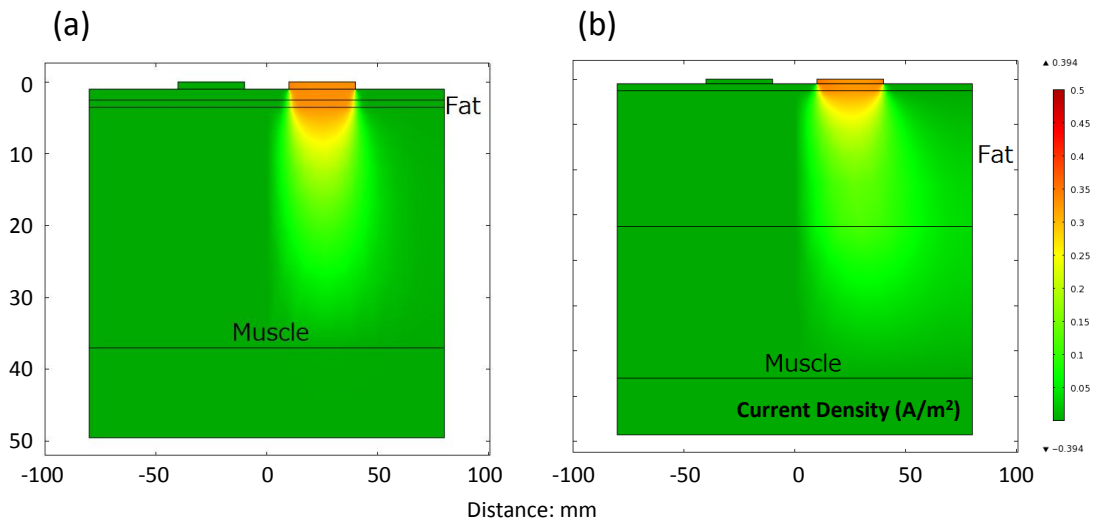


Figure 7.3: Effect of the fat thickness in the laterally distribution of the current. Current Density at (a) 1 mm and (b) 30 mm. An increase of fat thickness spreads the current density outside the region under the electrode.

7.3 Fat thickness study

The influence of electrode size and anode position on spatial nerve activation have been investigated before (49). However, the effect of fat thickness on selectivity needs to be further analyzed, using activation volume (AV). The aim of this study is to investigate the influence of fat thickness on the AV and activation depth (AD) for nerve fibers with different diameters, in order to quantify the selectivity of nerves.

7.3.1 Parameters

The thigh model is represented by a multiple-layer cylinder, composed of superficial stimulation electrodes, skin (1.5 mm), subcutaneous fat (2 mm to 60 mm), muscle (64.2 mm), and bone. For simplification, the electrical parameters are isotropic and frequency independent for each domain. The electrodes were modeled as a 1 mm thick electrode-skin boundary layer (hydrogel) with a square shape of 4 cm of length, and separated by a distance of 5 cm. Four fiber diameters (8 μm , 10 μm , 12 μm , and 14 μm) which corresponds to 336 mV/cm², 453 mV/cm², 643 mV/cm², 1143 mV/cm², obtained by using the activation function in (91, 135).

The effect of fat thickness (0.2 cm to 6 cm) was studied employing a current stimulation with an amplitude of -100 mA (a monophasic square pulse of 1 ms), Table 7.2.

Table 7.2: Simulation parameters to study the effect of fat thickness in nerve activation

Parameter	Value
Electrode shape	Square(4 cm of length)
Current	-100 mA(monophasic), 1 ms
Inter-electrode distance	5 cm
Fat thickness	2 mm to 60 mm
Fiber thickness	(8, 10, 12, 14) μm

7.3.2 Results

Figure 7.4a (12) shows the volume of the activation volume VAV vs. subcutaneous fat thickness, for different MT that corresponds to an specific fiber diameter. As

expected, VAV decreases as fat thickness increases. Figure 7.4b shows the AD for different subcutaneous fat thickness. Clearly, the AD shows a similar pattern as VAV.

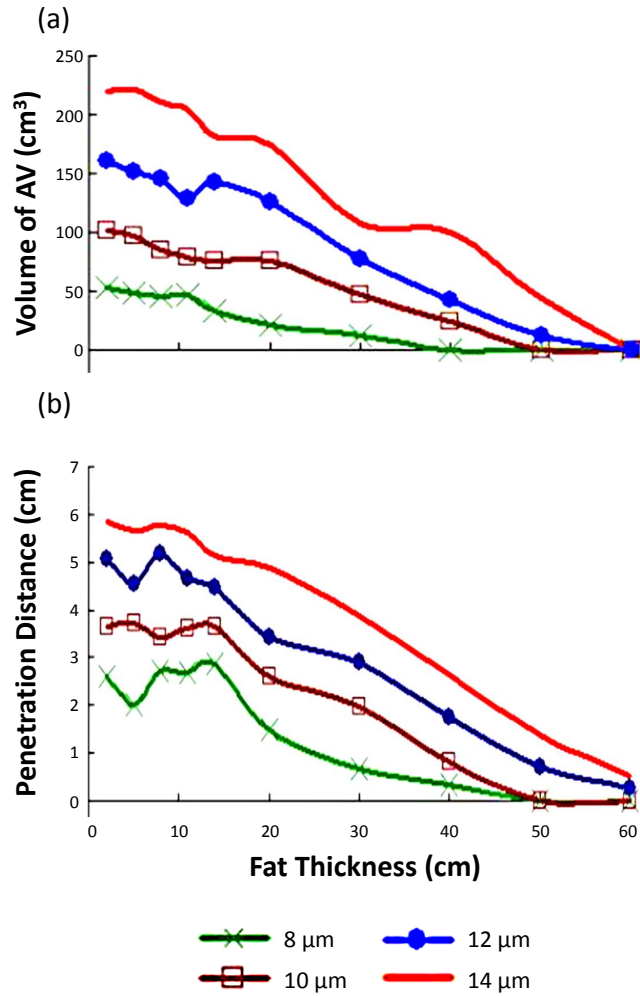


Figure 7.4: Effect of the fat thickness in VAV and AD. (a) VAV vs. fat thickness and (b) AD vs. fat thickness. Four fiber diameters (8 μm, 10 μm, 12 μm, and 14 μm) which corresponds to 336 mV/cm², 453 mV/cm², 643mV/cm², 1143 mV/cm² are evaluated.

7.3.3 Discussion and conclusion

We studied the effect of fat thickness on the AV and AD under the electrode. This investigation could contribute to the understanding of the exact location where nerves may be activated.

7. ROLE OF THE FAT THICKNESS AND ELECTRODES

According to Fig. 7.4, the VAV and AD on each fiber decrease when fat thickness increases, as expected. The reason is that the current density spreads over the fat domain, and part of it does not penetrate into the muscle domain when the fat thickness increases (136).

Also, small fiber (thinner) cannot be activated in deeper regions like larger fiber (thicker) at the same fat thickness. However, the selectivity under the electrode is better for smaller fiber because higher values of the activating function (AF) are concentrated near the electrode, and low values of AF spreads farther from the electrode (137). Therefore, forceful fiber (large) may be activated not only outside the electrode, but also in deeper regions than small fibers, which make more difficult control of fine motions using TES.

7.4 Inter-electrode distance and area of the electrode

The location, shape, and area of the electrodes have been a subject of analysis in many experimental and simulation studies. The objective is to find the optimal configuration to reach the best selectivity and comfort. In order to achieve this, experimental studies had measured the current and force to determine which configuration of electrodes requires less stimulation to achieve a MT or achieve a certain level of the maximum voluntary contraction. Comfort is assessed by questionnaires. On the other hand, computational simulation have the advantage of analyzing the activation inside the muscle, which helps to find not only the lowest current activation, but also the optimal selectivity.

In clinical application, larger electrode are used for stronger contraction with less current density in large muscles; therefore, more comfort on the skin compared with small electrodes. However, large electrodes is not selective for a desired movement. Small electrodes are used to stimulate the nerves near the surface and small muscles (138).

The effectiveness between small electrodes and large electrodes was studied by McNeal and Baker (139). They found no difference in stimulation effectiveness between using small electrodes (20 cm^2 , $4 \text{ cm} \times 5 \text{ cm}$) and larger electrode (36 cm^2 , $4 \text{ cm} \times 9 \text{ cm}$) in the force generation on the quadriceps and the hamstrings, but they reported that the large electrode is more comfortable for some subjects.

7.4 Inter-electrode distance and area of the electrode

Alon et al. (140) investigated the sensory, motor, pain, and maximal tolerable threshold on the gastrocnemius. He used two larger square electrodes of similar area to McNeal and Baker (30.25 cm², 40.3 cm²) and two smaller electrodes (2.25 cm², 9 cm²) and showed that large electrodes can generate larger force and more comfort than small size electrode. But, more likely that the stimulation intensity needs to be increased when large electrode is used (140, 141).

Lyons et al. (142) used two large round electrodes (19.63 cm² and 38.48 cm², similar to electrodes size used by Alon (140)) to investigate comfort. The smaller electrode was significantly more comfortable compared to the larger electrode on the gastrocnemius. They found that the optimum size of electrode depends on the stimulation location and the muscle under stimulation. Kuhn et al. (41) determined that the optimal size of the electrode for comfort and selectivity is a function of the depth of the activation required and fat thickness.

The effect of large subcutaneous fat thickness in the configuration of the electrode size and inter-electrode distance for the minimum stimulus current necessary for excitation was examined by Doheney et al. (60). The effect on the stimulation threshold of the electrode size and inter-electrode distance becomes less important when the thickness of the subcutaneous fat tissue increases. In that case, a large electrode can be used to increase comfort while keeping the activation.

In this study, the effect of inter-electrode distance and shape of the electrode are studied. The electrode location, size and shape are evaluated using the AV, AD, selectivity, and MT for nerve activation.

7.4.1 Parameters

This study simulates the effect of different distance between electrodes and its area on the nerve activation. The inter-electrode distance is varied between 1 cm and 12 cm. The area of the electrodes employed in the simulation are 0.25 cm² (0.5 cm x 0.5 cm), 2.25 cm² (1.5 cm x 1.5 cm), 6.25 cm² (2.5 cm x 2.5 cm), 12.25 cm² (3.5 cm x 3.5 cm), 20.25 cm² (4.5 cm x 4.5 cm), and 30.25 cm² (5.5 cm x 5.5 cm). The parameters are presented in Table 7.3.

7. ROLE OF THE FAT THICKNESS AND ELECTRODES

Table 7.3: Parameters to study the influence of inter-electrode distance and size of the electrode in nerve activation

Parameter	Value
Electrode shape	Square
Current	-20 mA(monophasic), 1 ms
Electrode area	(0.25, 2.25, 6.25, 12.25, 20.25, 30.25) cm ²
Inter-electrode distance	(1 to 12) cm
Fat thickness	5 cm

7.4.2 Results

The effect of the electrode size and inter-electrode distance are presented. The choice of the inter-electrode distance takes into account the possible range of the human thigh length. The effect of the nerve activation are evaluated using the AV, AD, and selectivity.

- VAV

Figure 7.5a illustrates the VAV for different inter-electrode distances. As expected, larger electrodes presents larger VAV. Additionally, there is a maximum VAV for each electrode. Larger electrodes have its maximum VAV at small inter-electrode distance. When the size of the electrode decreased, the location of the maximum VAV shifts to larger inter-electrode distances. For example, 0.25 cm² electrode has its maximum point at inter-electrode distance of 7 cm and 30.25 cm² between 1 cm and 4 cm.

The VAV has been normalized in Fig. 7.5b with respect to a reference (VAV of the smallest electrode, 0.25 cm²), where the maximum difference occurs at small inter-electrode distances. For example, the VAV of the 30.25 cm² electrode is 25% larger than the reference for inter-electrode distances lower than 5 cm.

- AD

Figure 7.6 (12) depicts the AD. As expected, smaller electrodes (0.25 cm², 2.25 cm², 6.25 cm²) present deeper activation. However, in the case of a inter-electrode distance smaller than 3 cm the AD decreased considerably, even lower than larger electrodes. For large electrodes (12.25 cm², 20.25 cm², 30.25 cm²), the AD is improved using small inter-electrode distance, in this simulation, around 2 cm and 3 cm.

- Selectivity

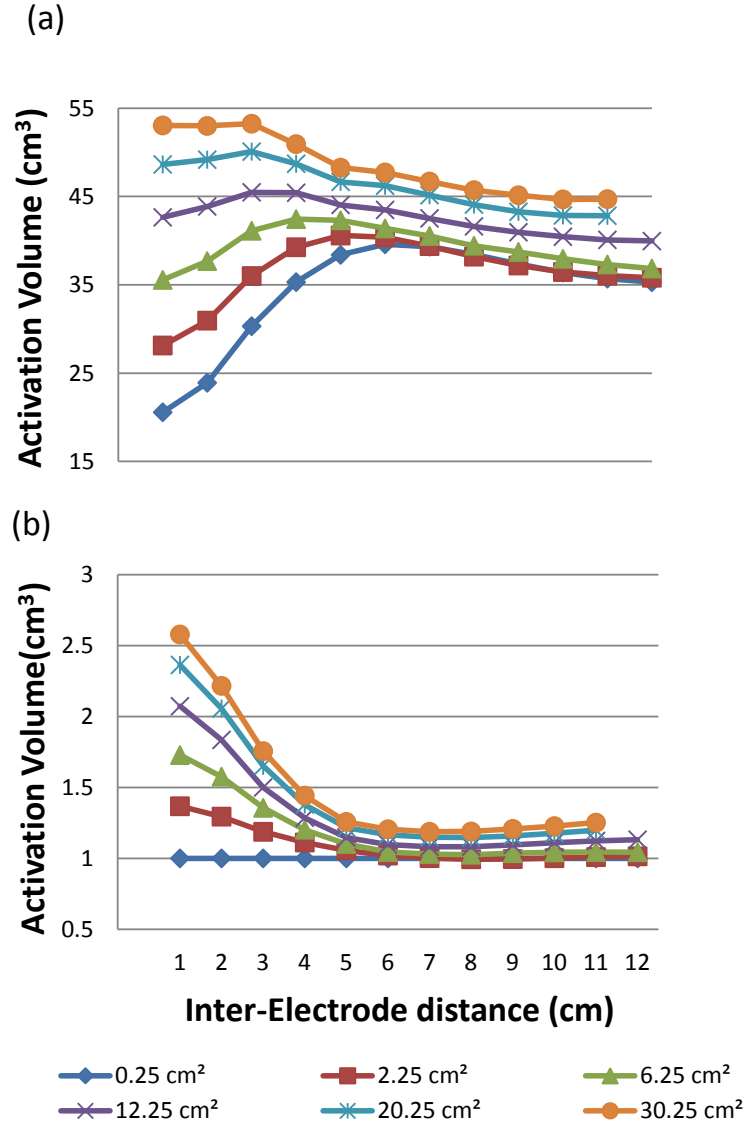


Figure 7.5: AV vs. inter-electrode distance. (a) Unnormalized values of the VAV are presented and (b) VAV values have been normalized with respect to the VAV of the smallest electrode size (42).

Selectivity is shown Fig. 7.7a. It is clear that selectivity is better for smaller electrodes. Additionally, the effect of inter-electrode distance on the electrode is very high for small electrodes. On the contrary, larger electrodes are not sensitive to inter-electrode distance, Fig. 7.7b.

7. ROLE OF THE FAT THICKNESS AND ELECTRODES

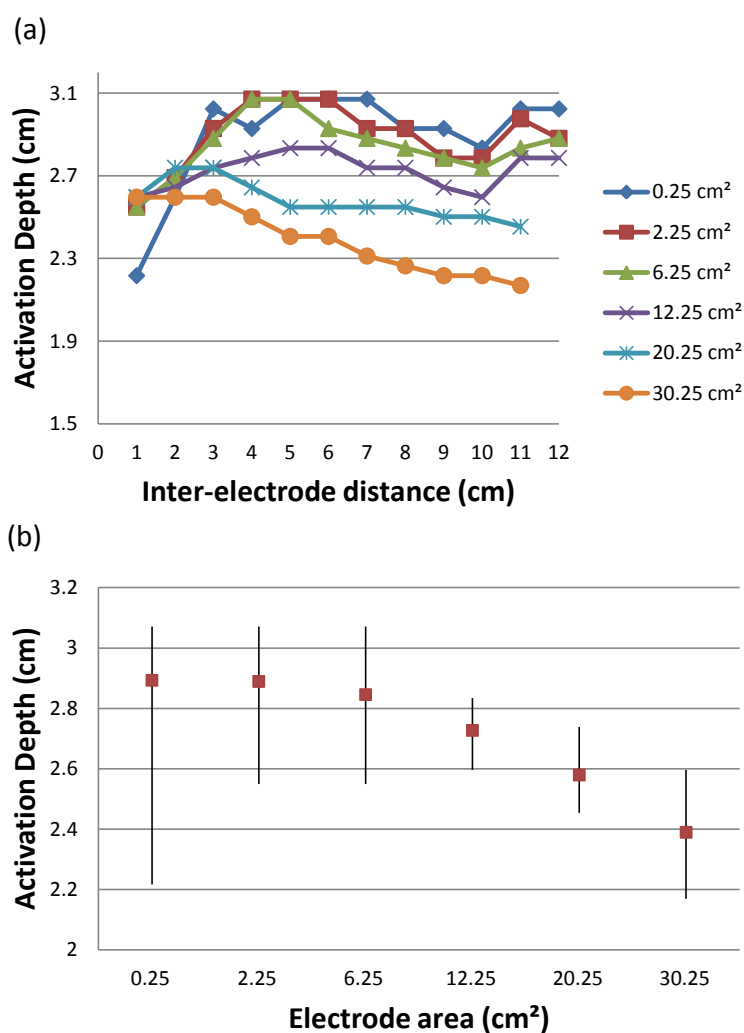


Figure 7.6: AD vs. inter-electrode distance. (a) Unnormalized values of the AD are presented and (b) AD range for a inter-electrode distance variation from 1 cm to 12 cm.

7.4.3 Discussion and conclusion

The main concern in powerful muscle activation is not selectivity but is the number of activated fibers, which can be quantify by the VAV. The results of inspecting the VAV are the following: 1) large electrode presents larger VAV compared to small electrode at the inter-electrode distances investigated and 2) the location of the inter-electrode distance should be taking into consideration, as illustrated in Fig. 7.5. In case of large electrode, maximum VAV occurs at small inter-electrode distance. On the other hand, maximum VAV takes place at larger inter-electrode distance when the area of

7.4 Inter-electrode distance and area of the electrode

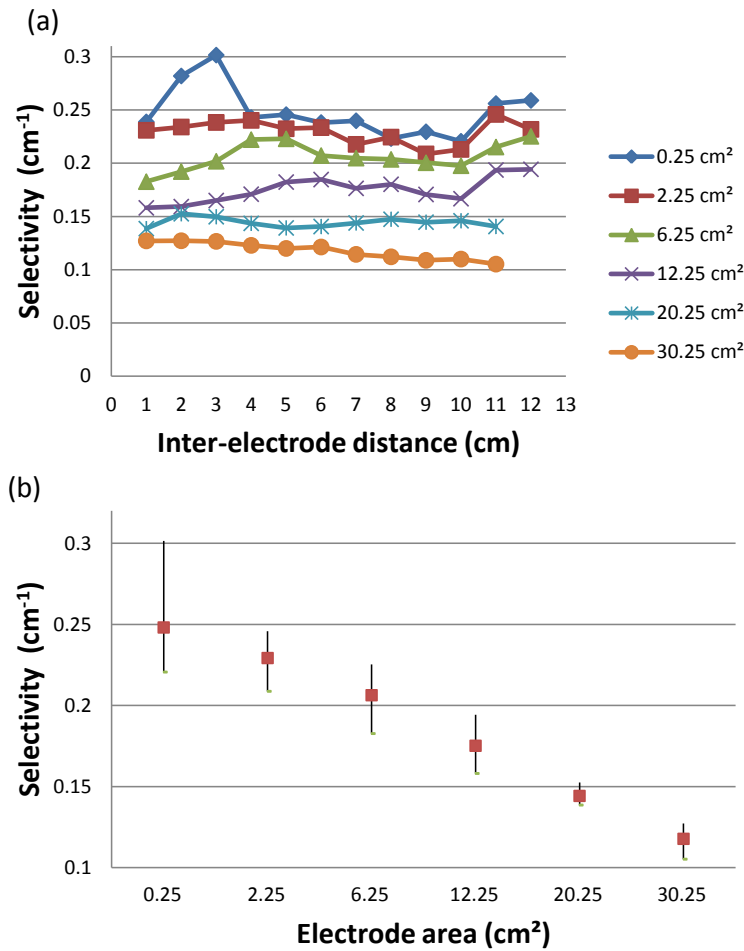


Figure 7.7: Selectivity vs. inter-electrode distance. (a) Unnormalized values of the selectivity are presented and (b) selectivity range for a inter-electrode distance variation from 1 cm to 12 cm (12).

the electrode is decreased.

Experimentally, large electrode produces more comfort and stronger motor response than small electrode, but more likely that the stimulation intensity need to be increased (140). The result of this study agrees because large electrode presents greater VAV than small electrode. Furthermore, the optimum size of electrode will depend on the size of muscle stimulated (selectivity) and location of stimulation (motor point) (142).

Doheny et al. (60) used the AF to simulated the effect of inter-electrode distance for different electrode's area. They investigated the inter-electrode distance (4 cm, 5.5 cm, and 8.25 cm) using a square electrode of area 0.707 cm². The result was a decrease

7. ROLE OF THE FAT THICKNESS AND ELECTRODES

of the AF for larger inter-electrode distance, which compared to our results using the VAV. Nevertheless, in the case of larger electrodes our results shows that VAV not only decreases, but also increases for short inter-electrode distance.

According to Fig. 7.5b, the maximum difference between electrodes occurs at small inter-electrode distances. In the case of 30.25 cm² electrode, its VAV is 25% larger than the reference at inter-electrode distances lower than 5 cm. The effect of the inter-electrode distance in the VAV can be explained by examining in detail the shape of the AV. In case of small electrodes, the shape of the AV is not symmetrical at small inter-electrode distance. Nevertheless, its shape tends to become symmetrical when inter-electrode distance increases, as observed in Fig. 7.8. The reason is that the shape of the AV under the cathode electrode is perturbed by the hyperpolarization beneath the anode electrode. The hyperpolarization interferes with the AV under the cathode electrode at close distance between the electrodes, decreasing it. The interference is less when two electrodes are separated explaining the effect of the inter-electrode in the AV.

As expected, small electrode (0.25 cm², 2.25 cm², 6.25 cm²) presents deeper activation, as reported in other studies (140, 143). However, it was not reported before that small electrode's penetration is diminished over small inter-electrode range and large electrodes experiences an increased in the AD. Moreover, selectivity is better for smaller electrodes, but inter-electrode distance should be considered for optimal selectivity. On the contrary, larger electrodes are not sensitive to inter-electrode distance.

In summary, for deeper penetration, small electrodes should be used for inter-electrode distances over 3 cm. In case of larger electrodes, small inter-electrode distance should be considered.

7.4 Inter-electrode distance and area of the electrode

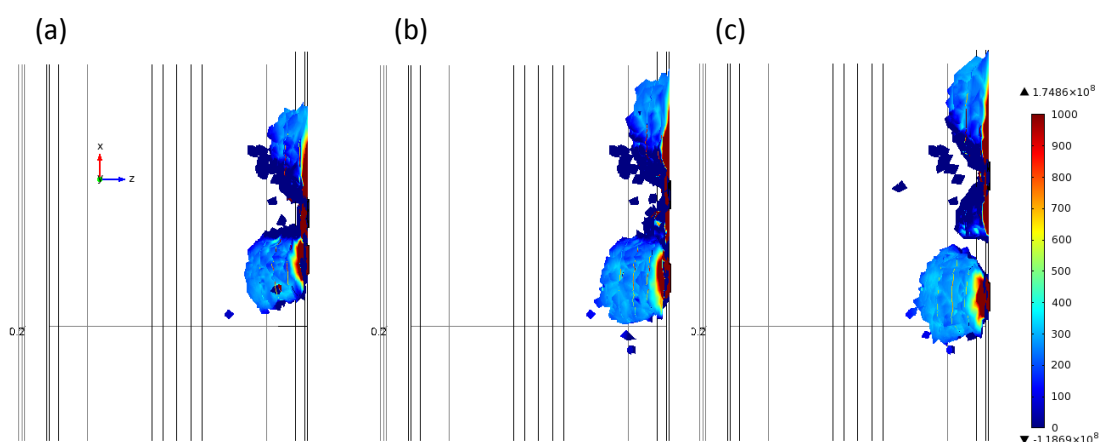


Figure 7.8: Shape of the AV at different inter-electrode distances. Lateral view of the AV at different inter-electrode distances: (a) 1 cm, (b) 3 cm, and (c) 5 cm. The upper electrode is the anode and the lower one is the cathode. The AV near the cathode is asymmetric at lower inter-electrode distance and symmetric at larger inter-electrode distances.

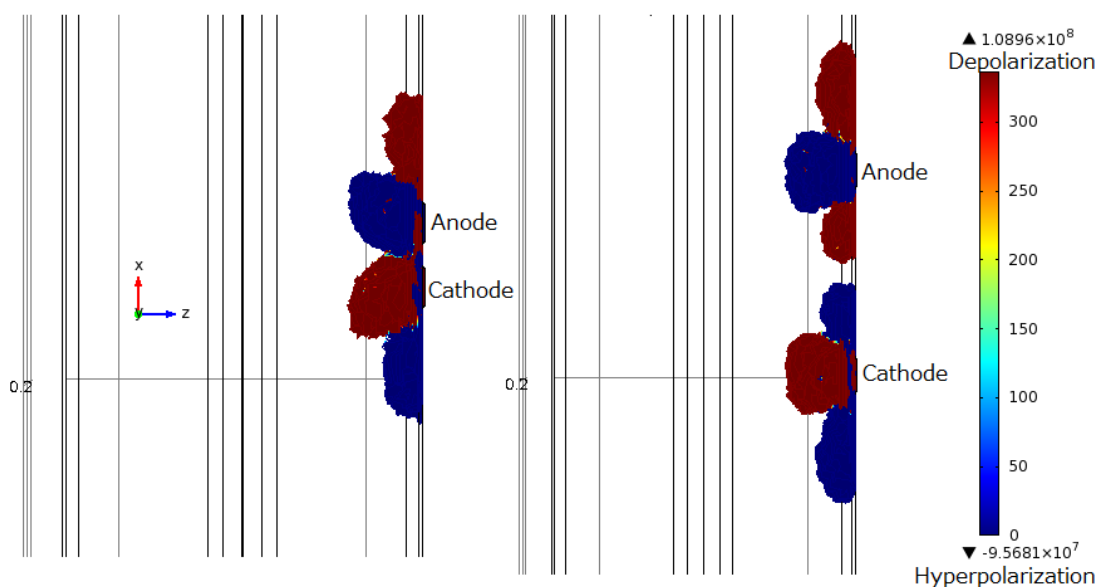


Figure 7.9: Depolarization and hyperpolarization regions under the cathode and anode electrode. The hyperpolarization (blue) and depolarization (red) regions are shown. Hyperpolarization inhibits the nerve activation and depolarization may lead to an AP. The hyperpolarization interferes the depolarization region under the cathode electrode reducing its volume at close inter-electrode distance.

7.5 Electrode shape and current study

Few studies have considered the effect of the electrode shape. Experimentally, Forrester and Petrofsky (144) studied the effect of three shapes (square, round, and serrated edge) with a similar area of 25.8 cm². They measured the pain using a visual analogue scale (VAS) and the current to reach 10% of MVC on three muscles (biceps, quadriceps and tibialis anterior). They obtained that the electrode shape did not significantly change electrical stimulation. On the other hand, simulation studies have not examined the effect of electrode shape to date.

This study evaluates the nerve activation by two electrode shapes (round and square) of same area at different stimulation current intensities. Then, MT, AV, AD, and selectivity are used to compare their effects in the nerve activation.

7.5.1 Parameters

Square and round electrodes are inspected using cathodic stimulation from 0 mA to 60 mA, and two areas are examined for each shape (0.25 cm² and 30.25 cm²). The parameters are presented in Table 7.4.

Table 7.4: Simulation parameters to study the effect of current intensity and shape of the electrode in nerve activation

Parameter	Value
Electrode shape	Square and Round
Current amplitude	(-5 to -90) mA, monophasic, 1 ms
Electrode area	(0.25 and 30.25) cm ²
Inter-electrode distance	6 cm
Fat thickness	5 cm
Nerve location	4.2 mm from muscle surface 10.7 mm from electrode

7.5.2 Results

MT in a nerve fiber of 14 μ m at 4.2 mm from the interface between the muscle and fat layer was calculated. The result of the simulation of the MT shows that there is no significant difference between the round and square electrode, as shown in Table 7.5.

7.5 Electrode shape and current study

The AV, AD, and selectivity are analyzed, as shown in Figs. 7.10a, 7.10b, and 7.10c (12), respectively. They also show no difference between round and square electrode of the same area.

Moreover, small and large electrodes present some differences when current intensity is modified:

1. Small and large electrode have similar VAV at low current (smaller than 10 mA), Fig. 7.10a. But, large electrode has greater VAV in contrast to small electrodes when applied current increases.
2. AD of small and large electrode tends to be similar at high current, Fig. 7.10b.
3. Selectivity converges to a similar value at high current, Fig. 7.10c.

Table 7.5: Motor threshold for a small and large electrode using a round and square electrodes

Shape	Size	
	0.25 cm^2	30.25 cm^2
Round	8.865 mA	83.75 mA
Square	8.815 mA	82.75 mA
Percentage difference	0.57	1.20

7. ROLE OF THE FAT THICKNESS AND ELECTRODES

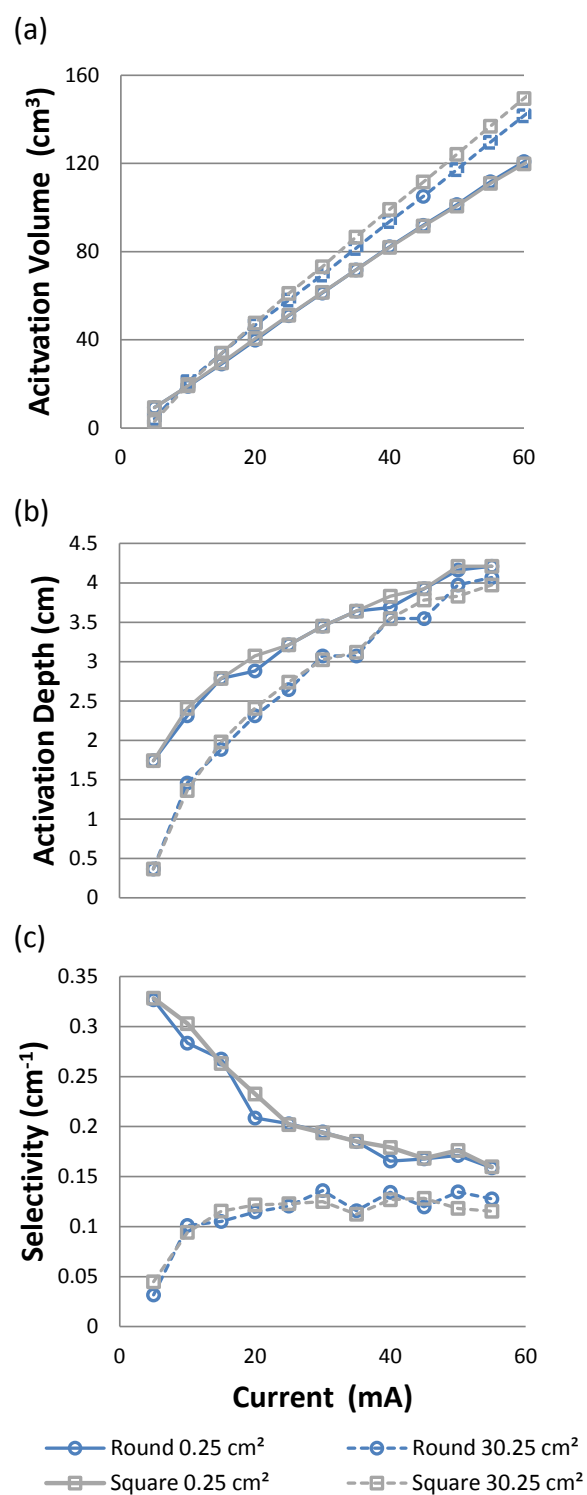


Figure 7.10: Effect of the current density in AV, AD, and selectivity. (a) AV vs. current intensity, (b) AD vs. current density, (c) selectivity vs. current density

7.5.3 Discussion and conclusion

The mean current necessary to evoke an AP using round electrodes is slightly greater than square electrode. However, there is no significant difference between round and square electrodes in nerve activation from the results of VAV, AD, selectivity, and MT, which was also observed experimentally by Petrosfky (144).

As has been said in the previous section, small electrode presents better AD and selectivity. In contrast, the AD and selectivity are similar between large and small electrodes in the case of high current stimulation, as observed in Figs. 7.10b and 7.10c. That is, high current stimulation decreases the selectivity of small electrodes, Fig. 7.10c. Therefore, larger electrodes are a better option for comfort and a major area of the muscle could be reached for activation.

Chapter 8

Conclusion and Future Work

8.1 Conclusions

Anatomical, electrical properties of the tissues, and stimulation factors should be carefully represented to have reliable and valid models of the neural activity. Reliable models do not only refer to numerical stability for convergence, but also to consistent results. Valid models refer to accurate computation of the extracellular potentials, nerve activation, and force generation according to experimental results. However, there are no studies that 1) confirm experimentally the validation of DMs and its simplified version (quasi-static approximation) when non-harmonic stimulation waveforms are used as input signal, 2) clarify the level of geometric detail necessary. Then, the resulting model can be used to study the effects of stimulation factor in electrical stimulation.

For this purpose, in chapter 3, an electrophysiological computational model responding to TES was developed in which different formulation approximations and geometry representations were investigated. In this model, the calculation of the nerve activation in the micro level was linked to the macro level by assuming that the activation of one representative nerve was the MT, and the percentage of activated nerves, from a group innervating a muscle, was proportional to the force. Evidence of these assumption is that stimulated muscle cross-section area, which is measured by muscle functional MRI, has a linear relationship with the force production (34).

The present implementation had the following limitations: 1) Prediction of the activation thresholds by the employed nerve model (CRRSS) was qualitative rather than quantitative. 2) The thickness of the nerve fiber was assumed to be one dimension,

8. CONCLUSION AND FUTURE WORK

and its action potential did not affect the extracellular potential. These simplifications could be replaced by 3D nerve models (145) and the coupling between the extracellular potential and the action potential propagation (146); however, 3D nerve model are necessary when target neurons are close to the stimulation electrodes, which is not the case. 3) The voltage drop in the electrode-skin was considered by the capacitance and resistance of the hydrogel material which was a viable method for large electrodes. 4) The uncertainty of the calculation of the activation threshold was caused by the number of DOF (degrees of freedom), the detection method of the action potential, and the spatial resolution of the voltage profile along the nerve fiber. Its convergence was guaranteed by increasing the number of DOF, using a spatial resolution of 0.1 mm for the voltage profile along the nerve and an error of 10 μA in the input to detect an action potential.

Chapter 4 introduced a new application of the tissue-like phantom: measurement of the potential distribution in a dielectrically dispersive material to validate the DM using non-harmonic input signals. From the validated model, the quasi-static approximation was investigated. It was found that it had an optimal frequency that allowed the simplification of the dielectric properties to a single parameter. It converged to a lower limit as pulse durations increased. The pulse duration of the experiments through this study was 0.5 ms (typical for FES), which was in the range of saturation where quasi-static approximation was in good agreement with DM.

Generally, limbs are simplified into concentric cylinders as a reasonable assumption in TES, but their limitations have not been revised. Chapter 5 provided evidence for the usage of simplified models, such as in applications of electrodes optimization. Also, nonhomogeneities (blood vessels and sciatic nerve) should be taken into account for stimulation of deep nerves, and their effect is negligible when stimulation comes from the anterior or lateral sites of the thigh. However, other morphologies need a different level of simplification like the brain tissues, which requires more detail in the description of non trivial effects, such as folding and crowns patterns in the gyrus (9, 147, 148).

Chapter 6 investigated experimentally and numerically the effect of the variation of the dielectric tissues in voltage and current stimulation. For that, the novel human-phantom coupling method was proposed to inspect muscle activation while parameters were systematically changed using an artificial fat tissue. As a result, current stimulation needed larger stimulation at lower impedance to generate muscle activity in con-

trast to voltage stimulation. And, long pulses had a larger voltage output for current stimulation; conversely, shorter pulses had a higher voltage at the muscle for voltage stimulation under the same dispersive tissues using PC stimulation.

Chapter 7 investigated the role of fat thickness and electrode configuration in the selectivity and nerve activation using the validated model. Large electrode area was found to have larger activation but lower selectivity. Conversely, small electrode area had lower activation area but better selectivity, which was reduced at high intensity stimulation. Two electrode shapes (round and square) did not have a significant difference.

In summary, the factors that influence directly the nerve activation should be carefully represented and modeled by the simulation studies. Some of the challenges of the present models are validation, model complexity, and parameters sensitivity. Therefore, we developed an electrophysiological computational model focused on nerve activation in the thigh to evaluate its reliability and validity under different anatomical and dielectric properties. We expect that by simplifying the formulation, morphology and dielectrically dispersive parameters, faster numerical solutions and feasible analytical solutions can be achieved, while keeping reliability and validity. Moreover, the methods applied in this study can be translated to different physics to evaluate the trade-off between computation cost and prediction of complex geometries and formulations, which in turn, can help in the development of a complete biophysically based computational modeling of the human.

The most important contribution and findings are listed below:

1. A novel experimental verification of the DM was carried out.
2. Quasi-static approximation was valid for non-harmonic stimulation signal by selecting an optimal frequency.
3. Optimal frequency converged to a lower limit for large pulse duration more than 0.1 ms.
4. The results obtained from CM and PM held for studies of electrode optimization similar to AM.
5. Human-phantom coupling is a novel experiment method that allows a systematic variation of tissues properties (fat) to study its effect in muscle contraction.

8. CONCLUSION AND FUTURE WORK

6. The model confirmed the relationships between selectivity and activation region for different electrode areas, and new insight in the effect of electrode shape were acquired.

8.2 Future work

It is important to further extend the validation results obtained in this study. Regarding validation of the voltage distribution simulation, 1) the geometry of the human-equivalent phantom should mimic closer the anatomy region under investigation, 2) voltage distribution in animal experiments should confirm the results of the human-equivalent phantom, 3) the effect of the muscle deformation on the voltage distribution should be clarified in the model. With regard to validation of nerve activation from superficial electrodes, motor threshold and strength duration-curve are indirect methods to validate the nerve activity at a macro level; however, nerve activation in the micro level needs to be investigated further for validation of physiologically-based model of the nerve. It can be achieved by in vivo measurements of the nerve activity by needle electrodes or a hybrid between tissue-equivalent phantom and a biological nerve.

In addition, the model should be improved to investigate in more detail the electrophysiological processes. The effect of spatial recruitment of muscle requires a closer representation of the peripheral nerve innervating the muscles under study. For that, muscle architecture, motor entry, endplate distribution, and its synapse should be carefully implemented and verified. Muscle function MRI and high density EMG can be used for validation. The former provides a spatially map of the recruitment postexercise, and the latter obtains the muscle temporal and spatial responses. This model can be used to investigate co-contraction between neighboring muscles. Also, the nerve model can be improved to investigate the effect in the nerve activity of nerve diseases related to morphological or electrical changes of the nerve.

References

- [1] ML NEAL AND R KERCKHOFFS. **Current progress in patient-specific modeling.** *Briefings in bioinformatics*, **2**(1):111–126, 2009. 2
- [2] P HUNTER, T CHAPMAN, P V COVENEY, B DE BONO, V DIAZ, J FENNER, A FRANGI, P HARRIS, R HOSE, P KOHL, P LAWFOED, K MCCORMACK, M MENDES, S OMHOLT, A QUARTERONI, N SHUBLAQ, J SKÅ R, K STROETMANN, J TEGNER, S THOMAS, I TOLLIS, I TSAMARDINOS, J VAN BEEK, AND M VICECONTI. **A vision and strategy for the virtual physiological human: 2012 update.** *Interface focus*, **3**(2):20130004, April 2013. 2
- [3] B CALVO AND E PEÑA. *Patient-specific computational modeling.* Springer, 2012. 2
- [4] MA AHAD AND S B RUTKOVE. **Finite element analysis of electrical impedance myography in the rat hind limb.** In *Conference Proceedings of the International Conference of IEEE Engineering in Medicine and Biology Society*, pages 630–633. Beth Israel Deaconess Medical Center, Harvard Medical School, Boston, MA 02215 USA. mahad@bidmc.harvard.edu, 2009. 2, 7, 75, 91
- [5] L MESIN. **Volume conductor models in surface electromyography: Computational techniques.** *Computers in Biology and Medicine*, **43**(7):942–952, 2013. 2, 10, 50, 75
- [6] L MESIN, R MERLETTI, AND T M M VIEIRA. **Insights gained into the interpretation of surface electromyograms from the gastrocnemius muscles: A simulation study.** *Journal of Biomechanics*, **44**(6):1096–1103, 2011. 2
- [7] Y OHMINE, T MORIMOTO, Y KINOCHI, T IRITANI, M TAKEUCHI, M HAKU, AND HI NISHITANI. **Basic study of new diagnostic modality according to non-invasive measurement of the electrical conductivity of tissues.** *The journal of medical investigation JMI*, **51**(3-4):218–225, 2004. 2, 75
- [8] H. LIN, M TAKAHASHI, K SAITO, AND K ITO. **Performance of Implantable Folded Dipole Antenna for In-Body Wireless Communication.** *IEEE Transaction on Antennas and Propagation*, **61**(3):1363–1370, 2013. 2
- [9] A OPITZ, M WINDHOFF, R M HEIDEMANN, R TURNER, AND A THIELSCHER. **How the brain tissue shapes the electric field induced by transcranial magnetic stimulation.** *NeuroImage*, **58**(3):849–859, 2011. 2, 76, 120
- [10] G R HERNÁNDEZ-LABRADO, J L POLO, EL LÓPEZ-DOLADO, AND J E COLLAZOS-CASTRO. **Spinal cord direct current stimulation: finite element analysis of the electric field and current density.** *Medical & Biological Engineering & Computing*, **49**(4):417–429, 2011. 2
- [11] J H K KIM, M L TREW, AJ PULLAN, AND O RÖHRLE. **Simulating a dual-array electrode configuration to investigate the influence of skeletal muscle fatigue following functional electrical stimulation.** *Computers in biology and medicine*, **42**(9):915–24, 2012. 2, 50

REFERENCES

- [12] J GOMEZ-TAMES, J GONZALEZ, AND W YU. **A study of thigh muscle activation for transcutaneous electrical stimulation using a 2D and 3D model explanatory models.** *The Japanese Bio-Electrical And Physical Stimulation Research Society*, **25**:38–47, 2011. 2, 86, 99, 100, 101, 104, 108, 111, 115
- [13] J GOMEZ-TAMES, J GONZALEZ, AND W YU. **A Simulation Study on the Dominance of the Tissues' Conductivity in the Muscle Recruitment.** *Journal of Medical Imaging and Health Informatics*, **3**(1):72–78, 2013. 2, 22, 35, 80, 82, 87
- [14] TM KESAR, R PERUMAL, AND A JANCOSKO. **Novel patterns of functional electrical stimulation have an immediate effect on dorsiflexor muscle function during gait for people poststroke.** *Physical therapy*, **90**(1):55–66, 2010. 3
- [15] G M LYONS, T SINKJAER, J BURRIDGE, AND D J WILCOX. **A review of portable FES-based neural orthoses for the correction of drop foot.** *IEEE Trans Neural Syst Rehabil Eng*, **10**(4):260–279, December 2002. 3
- [16] C Y YEH, K H TSAI, F C SU, AND H C LO. **Effect of a bout of leg cycling with electrical stimulation on reduction of hypertonia in patients with stroke.** *Archives of physical medicine and rehabilitation*, **91**(11):1731–6, November 2010. 3
- [17] L GRIFFIN, M J DECKER, J Y HWANG, B WANG, K KITCHEN, Z DING, AND J L IVY. **Functional electrical stimulation cycling improves body composition, metabolic and neural factors in persons with spinal cord injury.** *Journal of electromyography and kinesiology : official journal of the International Society of Electrophysiological Kinesiology*, **19**(4):614–22, August 2009. 3
- [18] T E JOHNSTON, B T SMITH, AND R R BETZ. **Strengthening of partially denervated knee extensors using percutaneous electric stimulation in a young man with spinal cord injury.** *Arch Phys Med Rehabil*, **86**(5):1037–1042, May 2005. 3
- [19] S HASEGAWA, M KOBAYASHI, R ARAI, A TAMAKI, T NAKAMURA, AND T MORITANI. **Effect of early implementation of electrical muscle stimulation to prevent muscle atrophy and weakness in patients after anterior cruciate ligament reconstruction.** *J Electromyogr Kinesiol*, **21**(4):622–630, August 2011. 3
- [20] F PICHON, J C CHATARD, A MARTIN, AND G COMETTI. **Electrical stimulation and swimming performance.** *Medicine and science in sports and exercise*, **27**(12):1671–6, December 1995. 3
- [21] N A MAFFIULETTI, S DUGNANI, M FOLZ, E DI PIERNO, AND F MAURO. **Effect of combined electrostimulation and plyometric training on vertical jump height.** *Medicine and science in sports and exercise*, **34**(10):1638–44, October 2002. 3
- [22] N BABAULT, G COMETTI, BERNARDIN, M POUSSON, AND J C CHATARD. **Effects of electromyostimulation training on muscle strength and power of elite rugby players.** *Journal of strength and conditioning research / National Strength & Conditioning Association*, **21**(2):431–7, May 2007. 3
- [23] E CAGGIANO, T EMREY, S SHIRLEY, AND R L CRAIK. **Effects of electrical stimulation or voluntary contraction for strengthening the quadriceps femoris muscles in an aged male population.** *The Journal of orthopaedic and sports physical therapy*, **20**(1):22–8, July 1994. 3
- [24] L PEDRINI AND F MAGNONI. **Spinal cord stimulation for lower limb ischemic pain treatment.** *Interact Cardiovasc Thorac Surg*, **6**(4):495–500, August 2007. 3
- [25] M SHIMOJO, T SUZUKI, A.NAMIKI, T SAITO, M KUNIMOTO, R MAKINO, H.OGAWA, M ISHIKAWA, AND K MABUCHI. **Development of a System for experiencing tactile sensation from a robot hand by electrically stimulating sensory nerve fiber.** In *Proc. IEEE Int. Conf. Robotics and Automation ICRA '03*, **1**, pages 1264–1270, 2003. 3

REFERENCES

- [26] M GOBBO, P GAFFURINI, L BISSOLOTTI, F ESPOSITO, AND C ORIZIO. **Transcutaneous neuromuscular electrical stimulation: influence of electrode positioning and stimulus amplitude settings on muscle response.** *Eur J Appl Physiol*, **111**(10):2451–2459, October 2011. 3
- [27] A DELITTO, M J STRUBE, A D SHULMAN, AND S D MINOR. **A study of discomfort with electrical stimulation.** *Physical therapy*, **72**(6):410–21; discussion on 421–4, June 1992. 3
- [28] M VANDERTHOMMEN, S DUTEIL, C WARY, J S RAYNAUD, A LEROY-WILLIG, J M CRIELAARD, AND P G CARLIER. **A comparison of voluntary and electrically induced contractions by interleaved 1H- and 31P-NMRS in humans.** *Journal of applied physiology (Bethesda, Md. : 1985)*, **94**(3):1012–24, March 2003. 3
- [29] C M GREGORY AND C S BICKEL. **Recruitment Patterns in Human Skeletal Muscle During Electrical Stimulation.** *Physical Therapy*, **85**(4):358–364, April 2005. 3, 4
- [30] R KINUGASA, D SHIN, J YAMAUCHI, C MISHRA, J A HODGSON, V R EDGERTON, AND S SINHA. **Phase-contrast MRI reveals mechanical behavior of superficial and deep aponeuroses in human medial gastrocnemius during isometric contraction.** *J Appl Physiol*, **105**(4):1312–1320, October 2008. 3
- [31] A J BERGQUIST, M J WIEST, AND D F COLLINS. **Motor unit recruitment when neuromuscular electrical stimulation is applied over a nerve trunk compared with a muscle belly: quadriceps femoris.** *Journal of applied physiology*, **113**(1):78–89, July 2012. 4
- [32] C S BICKEL, C M GREGORY, AND J C DEAN. **Motor unit recruitment during neuromuscular electrical stimulation: a critical appraisal.** *European journal of applied physiology*, **111**(10):2399–407, October 2011. 4
- [33] Y OKUMA, A J BERGQUIST, M HONG, K M CHAN, AND D F COLLINS. **Electrical stimulation site influences the spatial distribution of motor units recruited in tibialis anterior.** *Clinical neurophysiology : official journal of the International Federation of Clinical Neurophysiology*, **124**(11):2257–63, November 2013. 4
- [34] G R ADAMS, R T HARRIS, D WOODARD, AND G A DUDLEY. **Mapping of electrical muscle stimulation using MRI.** *Journal of applied physiology (Bethesda, Md. : 1985)*, **74**(2):532–7, February 1993. 4, 119
- [35] B YUAN, G SUN, J GOMEZ-TAMES, Y IKEMOTO, J GONZARLEZ, C MURAI, R ACHARYA, W YU, AND S INO. **The Effect of an Auxiliary Stimulation on Motor Function Restoration by FES.** *Journal of Medical Systems*, **35**(5):855–861, 2011. 4
- [36] W YU, H YAMAGUCHI, AND H YOKOI. **EMG automatic switch for FES control for hemiplegics using artificial neural network.** *Robotics and Autonomous Systems*, **40**(2-3):213–224, 2002. 4
- [37] L LAPICQUE. **Definition experimentale de l’excitabilite.** 1909. 4, 39
- [38] LA GEDDES AND JD BOURLAND. **The strength-duration curve.** *Biomedical Engineering*, **6**:458–459, 1985. 4, 39
- [39] H B BOOM, A J MULDER, AND P H VELTINK. **Fatigue during functional neuromuscular stimulation.** *Progress in brain research*, **97**:409–18, January 1993. 4
- [40] R PACKMAN-BRAUN. **Relationship Between Functional Electrical Stimulation Duty Cycle and Fatigue in Wrist Extensor Muscles of Patients with Hemiparesis.** *Physical Therapy*, **68**(1):51–56, January 1988. 4

REFERENCES

- [41] A KUHN, T KELLER, M LAWRENCE, AND M MORARI. **The influence of electrode size on selectivity and comfort in transcutaneous electrical stimulation of the forearm.** *IEEE Transactions on Neural Systems and Rehabilitation Engineering*, **18**(3):255–262, 2010. 5, 6, 10, 11, 38, 50, 75, 107
- [42] J GOMEZ-TAMES, J GONZALEZ, AND W YU. **A simulation study: Effect of the inter-electrode distance, electrode size and shape in Transcutaneous Electrical Stimulation.** In *Engineering in Medicine and Biology Society (EMBC)*, pages 3576–3579, 2012. 5, 7, 22, 29, 38, 99, 109
- [43] AR WARD. **Electrical stimulation using kilohertz-frequency alternating current.** *Physical therapy*, **89**(2):181–190, 2009. 5, 87, 97
- [44] AR WARD, VJ ROBERTSON, AND H IOANNOU. **The effect of duty cycle and frequency on muscle torque production using kilohertz frequency range alternating current.** *Medical engineering & physics*, **26**(7):569–579, 2004. 5, 87
- [45] J PETROFSKY AND M LAYMON. **The transfer of current through skin and muscle during electrical stimulation with sine, square, Russian and interferential waveforms.** *Journal of medical engineering*, **33**(2):170–181, 2009. 5, 8, 87, 96
- [46] G KANTOR, G ALON, AND H S.HO. **The effects of selected stimulus waveforms on pulse and phase characteristics at sensory and motor thresholds.** *Phys Ther*, **74**(10):951–962, October 1994. 5
- [47] SD BENNIE AND JS PETROFSKY. **Toward the optimal waveform for electrical stimulation of human muscle.** *European journal of applied physiology*, **88**(1-2):13–19, 2002. 5, 87, 96
- [48] Y LAUFER AND M ELBOIM. **Effect of burst frequency and duration of kilohertz-frequency alternating currents and of low-frequency pulsed currents on strength of contraction, muscle fatigue, and perceived discomfort.** *Phys Ther*, **88**(10):1167–1176, October 2008. 5, 95
- [49] E P DOHENY, B.M.CAULFIELD, C M MINOGUE, AND M M LOWERY. **The effect of subcutaneous fat thickness on the efficacy of transcutaneous electrical stimulation.** In *Proc. 30th Annual Int. Conf. of the IEEE Engineering in Medicine and Biology Society EMBS 2008*, pages 5684–5687, 2008. 6, 104
- [50] A KUHN, T KELLER, AND M LAWRENCE. **Transcutaneous stimulation technology.** *Journal of Biomechanics*, **39**(Suppl 1):371, July 2006. 6
- [51] M REICHEL, W MAYR, AND F RATTAY. **Computer simulation of field distribution and excitation of denervated muscle fibers caused by surface electrodes.** *Artif Organs*, **23**(5):453–456, May 1999. 6
- [52] W M GRILL AND J T MORTIMER. **Stimulus waveforms for selective neural stimulation.** *Engineering in Medicine and Biology Magazine*, **14**(4):375–385, 1995. 6, 99
- [53] A L HODGKIN AND A F HUXLEY. **A quantitative description of membrane current and its application to conduction and excitation in nerve.** *J Physiol*, **117**(4):500–544, August 1952. 6, 18, 30, 140
- [54] B FRANKENHAEUSER AND A F HUXLEY. **The action potential in the myelinated nerve fiber of xenopus laevis as computed on the basis of voltage clamp data.** *J Physiol*, **171**:302–315, June 1964. 6, 30, 140
- [55] SY CHIU AND JM RITCHIE. **A quantitative description of membrane currents in rabbit myelinated nerve.** *The Journal of Physiology*, **292**(1):149–166, 1979. 6, 27, 30, 65, 138

REFERENCES

- [56] J.D. SWEENEY, J.T. MORTIMER, AND D DURAND. **Modeling of mammalian myelinated nerve for functional neuromuscular electrostimulation.** *IEEE -97th ann. conf. Eng. Med. Biol. Soc. Boston*, **9**:1577–1578, 1987. 6, 27, 30, 65, 138, 140
- [57] DR MCNEAL. **Analysis of a model for excitation of myelinated nerve.** *IEEE Transactions on Biomedical Engineering*, **4**:329–337, 1976. 6, 23, 27, 65
- [58] F RATTAY. **Analysis of models for external stimulation of axons.** *Biomedical Engineering, IEEE Transactions on*, **BME-33**,(10):974–977, 1986. 6
- [59] LM LIVSHITZ. **Interaction of array of finite electrodes with layered biological tissue: effect of electrode size and configuration.** *Neural Systems and Rehabilitation Engineering*, **9**(4):355–361, 2001. 6, 11, 100
- [60] E P DOHENY, B M CAULFIELD, C M MINOGUE, AND M M LOWERY. **Effect of subcutaneous fat thickness and surface electrode configuration during neuromuscular electrical stimulation.** *Medical Engineering & Physics*, **32**(5):468–474, 2010. 6, 10, 11, 50, 75, 107, 111
- [61] J H K KIM AND M TREW. **Investigating the influence of multi-Array electrode configurations and functional electrical stimulation protocols on skeletal muscle fatigue.** *Computers in Biology and Medicine*, page submitted, 2011. 6
- [62] O RÖHRLE, J B DAVIDSON, AND A J PULLAN. **A physiologically based, multi-scale model of skeletal muscle structure and function.** *Frontiers in physiology*, **3**:358, January 2012. 6
- [63] M BÖL, R WEIKERT, AND C WEICHERT. **A coupled electromechanical model for the excitation-dependent contraction of skeletal muscle.** *Journal of the mechanical behavior of biomedical materials*, **4**(7):1299–310, October 2011. 6, 11
- [64] F RATTAY. **Current distance relations for fiber stimulation with pointsources.** *IEEE Trans Biomed Eng*, **55**(3):1122–1127, March 2008. 7
- [65] A KUHN, T KELLER, S MICERA, AND M MORARI. **Array electrode design for transcutaneous electrical stimulation: a simulation study.** *Medical Engineering & Physics*, **31**(8):945–951, 2009. 7, 11, 75
- [66] A PEYMAN. **Dielectric properties of tissues; variation with age and their relevance in exposure of children to electromagnetic fields; state of knowledge.** *Progress in biophysics and molecular biology*, **10**(3):434–438, 2011. 7
- [67] TATSUMA YAMAMOTO AND YOSHITAKE YAMAMOTO. **Analysis for the change of skin impedance.** *Medical & Biological Engineering & Computing*, **15**(3):219–227, May 1977. 7, 86
- [68] JS PETROFSKY, H JI SUH, S GUNDA, M PROWSE, AND J BATT. **Interrelationships between body fat and skin blood flow and the current required for electrical stimulation of human muscle.** *Medical engineering & physics*, **30**(7):931–6, September 2008. 7, 91
- [69] A BEATTI, A RAYNER, L CHIPCHASE, AND T SOUVLIS. **Penetration and spread of interferential current in cutaneous, subcutaneous and muscle tissues.** *Physiotherapy*, **97**(4):319–326, December 2011. 8, 85
- [70] J PETROFSKY. **The effect of the subcutaneous fat on the transfer of current through skin and into muscle.** *Medical engineering & physics*, **30**(9):1168–1176, 2008. 8, 20, 85

REFERENCES

- [71] A KUHN AND T KELLER. **A 3d transient model for transcutaneous functional electrical stimulation.** *International Functional Electrical Stimulation Society Conference*, **10**:385–7, 2005. 9, 49, 50, 60
- [72] N D FILIPOVIC, ALS PEULIC, N D ZDRAVKOVIC, V M GRBOVIC-MARKOVIC, AND A J JURISIC-SKEVIN. **Transient finite element modeling of functional electrical stimulation.** *General Physiology and Biophysics*, **30**(1):59–65, 2011. 9, 49, 50, 60, 75
- [73] M M LOWERY, N S STOYKOV, J A DEWALD, AND T A KUIKEN. **Volume conduction in an anatomically based surface EMG model.** *IEEE transactions on bio-medical engineering*, **51**(12):2138–47, December 2004. 9, 49, 75
- [74] SJ DORGAN AND RB REILLY. **A model for human skin impedance during surface functional neuromuscular stimulation.** *Rehabilitation Engineering, IEEE Transactions on*, **7**(3):341–348, 1999. 9
- [75] A KUHN, T KELLER, B PRENAJ, AND M MORARI. **The relevance of non-linear skin properties for a transcutaneous electrical stimulation model.** *International Functional Electrical Stimulation Society Conference*, **11**:100–2, 2006. 9
- [76] A KUHN, T KELLER, M LAWRENCE, AND M MORARI. **A model for transcutaneous current stimulation: simulations and experiments.** *Medical & Biological Engineering & Computing*, **47**(3):279–289, 2009. 9, 35, 49, 62, 75, 81
- [77] R PLONSEY AND DB HEPPNER. **Considerations of quasi-stationarity in electrophysiological systems.** *The Bulletin of mathematical biophysics*, **29**(4):657–664, 1967. 9, 25, 49, 65
- [78] C A BOSSETTI, M J BIRDNO, AND W M GRILL. **Analysis of the quasi-static approximation for calculating potentials generated by neural stimulation.** *Journal of neural engineering*, **5**(1):44–53, March 2008. 9, 10, 24, 25, 50, 61, 65
- [79] NS STOYKOV AND MM LOWERY. **Frequency-and time-domain FEM models of EMG: capacitive effects and aspects of dispersion.** *Biomedical Engineering, IEEE Transactions on*, **49**(8):763–772, 2002. 9, 50, 62
- [80] CR BUTSON AND CC MCINTYRE. **Tissue and electrode capacitance reduce neural activation volumes during deep brain stimulation.** *Clinical neurophysiology*, **116**(10):2490–2500, 2005. 10, 24, 50, 61
- [81] PF GRANT AND MM LOWERY. **Effect of dispersive conductivity and permittivity in volume conductor models of deep brain stimulation.** *Biomedical Engineering, IEEE Transactions on*, **57**(10):2386–2393, 2010. 10, 50, 61
- [82] G COOPER, A T BARKER, B W HELLER, T GOOD, L P J KENNEY, AND D HOWARD. **The use of hydrogel as an electrode-skin interface for electrode array FES applications.** *Medical Engineering & Physics*, **33**(8):967–972, 2011. 10, 11, 75, 94
- [83] Y STICKLER, J MARTINEK, C HOFER, AND F RATTAY. **A finite element model of the electrically stimulated human thigh: changes due to denervation and training.** *Artificial Organs*, **32**(8):620–624, 2008. 10, 11, 75
- [84] Z LERTMANORAT, KJ GUSTAFSON, AND DM DURAND. **Electrode array for reversing the recruitment order of peripheral nerve stimulation: experimental studies.** *Annals of biomedical Engineering*, **34**(1):152–160, 2006. 10, 11, 35, 75

REFERENCES

- [85] V TZ KRASTEVA, S P PAPAPOV, AND I K DASKALOV. **Peripheral nerve magnetic stimulation: influence of tissue non-homogeneity.** *BioMedical Engineering Online*, **2**:19, 2003. 10, 50, 75
- [86] O RÖHRLE, J B DAVIDSON, AND A J PULLAN. **A physiologically based, multi-scale model of skeletal muscle structure and function.** *Frontiers in physiology*, **3**:358, 2012. 11
- [87] LM LIVSHITZ, PD EINZIGER, AND J MIZRAHI. **Current distribution in skeletal muscle activated by functional electrical stimulation: image-series formulation and isometric recruitment curve.** *Annals of biomedical engineering*, **28**(10):1218–1228, 2000. 11, 86, 102
- [88] J MARTINEK, M REICHEL, F RATTAY, AND W MAYR. **Analysis of calculated electrical activation of denervated muscle fibers in the human thigh.** *Artif Organs*, **29**(6):444–447, June 2005. 11
- [89] ACTAM. **Diagram of neuron with arrows but no labels**, 2008. 17
- [90] F RATTAY. **The basic mechanism for the electrical stimulation of the nervous system.** *Neuroscience*, **89**(2):335–346, March 1999. 19, 29, 137
- [91] F RATTAY. **Modeling the excitation of fibers under surface electrodes.** *IEEE Trans Biomed Eng*, **35**(3):199–202, March 1988. 19, 31, 104, 139
- [92] C GABRIEL, S GABRIEL, AND E CORTHOOT. **The dielectric properties of biological tissues: I. Literature survey.** *Physics in medicine and biology*, **41**(11):2231, 1996. 20, 26, 44, 45, 46, 64, 89
- [93] FJ PETTERSEN AND JO HØ GETVEIT. **From 3D tissue data to impedance using Simpleware ScanFE+ IP and COMSOL Multiphysicsa tutorial.** *Journal of Electrical Bioimpedance*, **2**(1):13–32, 2011. 20
- [94] B J ROTH. *The Electrical Conductivity of Tissues*. Boca Raton: CRC Press LLC., second edition, 2000. 20
- [95] S GRIMNES AND G MARTINSEN. *Bioimpedance & Bioelectricity Basics*. Academic Press, 2005. 20
- [96] J GOMEZ-TAMES, J GONZALEZ, AND W YU. **Simulation of the Muscle Recruitment by Transcutaneous Electrical Stimulation in a Simplified Semitendinosus Muscle Model.** *Converging Clinical and Engineering Research on Neurorehabilitation*, pages 449–453, 2013. 22, 35, 85
- [97] Y FUKUHARA, J GOMEZ-TAMES, AND W YU. **An experimental study on the effect of fat conductivity on voltage distribution and muscle recruitment using tissue-equivalent phantoms.** *E-Health and Bioengineering Conference*, pages 1–4, 2013. 22, 47
- [98] L MESIN AND R MERLETTI. **Distribution of electrical stimulation current in a planar multilayer anisotropic tissue.** *Biomedical Engineering, IEEE Transactions on*, **55**(2):660–670, 2008. 25
- [99] S GABRIEL, RW LAU, AND C GABRIEL. **The dielectric properties of biological tissues: II. Measurements in the frequency range 10 Hz to 20 GHz.** *Physics in medicine and biology*, **41**(11):2251, 1996. 26
- [100] S GABRIEL, RW LAU, AND C GABRIEL. **The dielectric properties of biological tissues: III. Parametric models for the dielectric spectrum of tissues.** *Physics in medicine and biology*, **41**(11):2271, 1996. 26
- [101] JR SCHWARZ AND G EIKHOF. **Na currents and action potentials in rat myelinated nerve fibres at 20 and 37 C.** *Pflügers Archiv*, **409**(6):569–577, 1987. 31, 140

REFERENCES

- [102] JR SCHWARZ, G REID, AND H BOSTOCK. **Action potentials and membrane currents in the human node of Ranvier.** *Pflügers Archiv*, **430**(2):283–292, 1995. 31, 140
- [103] X ZHANG AND JR ROPPOLO. **Mechanism of nerve conduction block induced by high-frequency biphasic electrical currents.** *Biomedical Engineering, IEEE Transactions on*, **53**(12):2445–2454, 2006. 31
- [104] F RATTAY, S RESATZ, P LUTTER, K MINASSIAN, B JILGE, AND M R DIMITRIJEVIC. **Mechanisms of electrical stimulation with neural prostheses.** *Neuromodulation*, **6**(1):42–56, January 2003. 31
- [105] N IMAMOGLU. **Pulse-Coupled Neural Network Segmentation and Bottom-Up Saliency-On Feature Extraction for Thigh Magnetic Resonance Imaging Based 3D Model Construction.** *Journal of Medical Imaging and Health Informatics*, **4**(2):220–229, 2014. 33, 64
- [106] NJ FULLER, CR HARDINGHAM, AND M GRAVES. **Predicting composition of leg sections with anthropometry and bioelectrical impedance analysis, using magnetic resonance imaging as reference.** *Clinical Science*, **96**:647–657, 1999. 33, 81
- [107] X C AN, J H LEE, S IM, M S LEE, K HWANG, H W KIM, AND SEUNG-HO HAN. **Anatomic localization of motor entry points and intramuscular nerve endings in the hamstring muscles.** *Surg Radiol Anat*, **32**(6):529–537, July 2010. 34, 35, 81
- [108] E ROMERO, O CUISENAIRE, J F DENEFF, J DELBEKE, B MACQ, AND C VERAART. **Automatic morphometry of nerve histological sections.** *J Neurosci Methods*, **97**(2):111–122, April 2000. 34, 35, 85
- [109] S DESHPANDE, M E GORMLEY JR, AND J R CAREY. **Muscle fiber orientation in muscles commonly injected with botulinum toxin: an anatomical pilot study.** *Neurotox Res*, **9**(2-3):115–120, April 2006. 34
- [110] D BELAVÝ, T MIKOVIC, J RITTWEGER, AND D FELSEBERG. **Estimation of changes in volume of individual lower-limb muscles using magnetic resonance imaging (during bed-rest).** *Physiol Meas*, **32**(1):35–50, January 2011. 35
- [111] A KUHN AND T KELLER. **A model for transcutaneous electrical stimulation using activation volumes to describe the influence of the electrode placement and size.** *Vienna Int. Workshop on Functional Electrostimulation*, 2007. 38
- [112] EN WARMAN, WM GRILL, AND D DURAND. **Modeling the effects of electric fields on nerve fibers: determination of excitation thresholds.** *IEEE Transactions on Biomedical Engineering*, **39**(12):1244–1254, 1992. 38
- [113] Y OKANO, K ITO, I IDA, AND M TAKAHASHI. **The SAR evaluation method by a combination of thermographic experiments and biological tissue-equivalent phantoms.** *Microwave Theory and Techniques, IEEE Transactions on*, **48**(11):2094–2103, 2000. 41
- [114] T TAKIMOTO AND T ONISHI. **Characteristics of biological tissue equivalent phantoms applied to UWB communications.** *Electronics and Communications in Japan*, **90**(5):48–55, 2007. 41
- [115] Y UNO AND K SAITO. **Structure of cylindrical tissue-equivalent phantom for medical applications.** *Electromagnetics in Advanced Applications*, pages 406–409, 2010. 41
- [116] K ITO, H KAWAI, AND K SAITO. **State of the art and future prospects of biological tissue-equivalent phantoms.** *Transactions. of IEICE*, **85**:582–596, 2002. 41

REFERENCES

- [117] C GABRIEL, A PEYMAN, AND EH GRANT. **Electrical conductivity of tissue at frequencies below 1 MHz.** *Physics in medicine and biology*, **54**(16):4863–4878, 2009. 44, 64, 89, 93
- [118] J KYBER, H HANSGEN, AND F PLIQUETT. **Dielectric properties of biological tissue at low temperatures demonstrated on fatty tissue.** *Physics in medicine and biology*, **37**(8):1675, 1992. 45
- [119] GM HAHN AND P KERNAHAN. **Some heat transfer problems associated with heating by ultrasound, microwaves, or radio frequency.** *Annals of the New York Academy of Sciences*, **335**(1):327–346, 1980. 45
- [120] A KUHN, G RAUCH, B PANCHAPHONGSAPHAK, AND T KELLER. **Using transient FE models to assess anatomical influences on electrical stimulation.** In *FEM Workshop*, Ulm, July 2005. 50
- [121] JULIANA H K KIM, JOHN B DAVIDSON, OLIVER RHRLE, TANYA K SOBOLEVA, AND ANDREW J PULLAN. **Anatomically based lower limb nerve model for electrical stimulation.** *Biomed Eng Online*, **6**(1):48, 2007. 50
- [122] M M LOWERY, N S STOYKOV, AND T A KUIKEN. **Independence of myoelectric control signals examined using a surface EMG model.** *IEEE Trans Biomed Eng*, **50**(6):789–793, June 2003. 50
- [123] PF GRANT AND MM LOWERY. **Contribution of dielectric dispersions to voltage waveforms arising from electrical stimulation.** *Engineering in Medicine and Biology Society (EMBC)*, pages 4148–4151, 2012. 51
- [124] J GOMEZ-TAMES, J GONZALEZ, AND W YU. **Influence of Different Geometric Representations of the Volume Conductor on Nerve Activation during Electrical Stimulation.** *Computational and Mathematical Methods in Medicine*, **2014**:1–10, 2014. 63, 65, 67, 68, 69, 70, 72, 77
- [125] J GOMEZ-TAMES AND W YU. **Assessment of nerve morphology in nerve activation during electrical stimulation.** *Computational Models for Life Sciences Conference*, **15559**(1):355–358, 2013. 63, 73
- [126] J LADENBAUER. **Stimulation of the human lumbar spinal cord with implanted and surface electrodes: a computer simulation study.** *Neural Systems and Rehabilitation Engineering*, **18**(6):637–645, 2010. 76
- [127] SJ WOODLEY AND SR MERCER. **Hamstring muscles: architecture and innervation.** *Cells tissues organs*, **179**(3):125–141, 2005. 85
- [128] D PRODANOV AND H K P FEIRABEND. **Morphometric analysis of the fiber populations of the rat sciatic nerve, its spinal roots, and its major branches.** *J Comp Neurol*, **503**(1):85–100, July 2007. 85
- [129] M A AHAD, P NARAYANASWAMI, L J KASSELMAN, AND S B RUTKOVE. **The effect of subacute denervation on the electrical anisotropy of skeletal muscle: implications for clinical diagnostic testing.** *Clin Neurophysiol*, **121**(6):882–886, June 2010. 86
- [130] T MATSUNAGA, Y SHIMADA, AND K SATO. **Muscle fatigue from intermittent stimulation with low and high frequency electrical pulses.** *Archives of Physical Medicine and Rehabilitation*, **80**(1):48–53, January 1999. 95, 97
- [131] R BUTIKOFER AND P D LAWRENCE. **Electrocutaneous nerve stimulation-I: model and experiment.** *IEEE transactions on bio-medical engineering*, **25**(6):526–531, 1978. 99

REFERENCES

- [132] P H GORMAN AND J T MORTIMER. **The effect of stimulus parameters on the recruitment characteristics of direct nerve stimulation.** *Biomedical Engineering, IEEE Transactions on*, (7):407–414, 1983. 99
- [133] V T KRASTEVA AND S P PAPAPOV. **Estimation of current density distribution under electrodes for external defibrillation.** *Biomed Eng Online*, 1(1):1–7, 2002. 102
- [134] M REICHEL, W MAYR, AND F RATTAY. **Simulation of the three-dimensional electrical field in the course of functional electrical stimulation.** *Artif Organs*, 26(3):252–255, March 2002. 103
- [135] A KUHN. *Modeling transcutaneous electrical stimulation.* PhD thesis, September 2008. 104
- [136] J GOMEZ, J GONZALES, AND W YU. **Preliminary simulation of the current distribution across the skin during surface stimulation using finite element analysis.** In *CCCA*, pages 495–498, 2011. 106
- [137] J GOMEZ, J GONZALES, AND W YU. **Influence of subcutaneous fat thickness upon the activation volume in transcutaneous electrical stimulation to a thigh simulation model.** In *international Functional Electrical Stimulation Society*, number 16, 2011. 106
- [138] T BAJD. **Surface Electrostimulation Electrodes.** *Wiley Encyclopedia of Biomedical Engineering*, 2006. 106
- [139] D R MCNEAL AND L L BAKER. **Effects of joint angle, electrodes and waveform on electrical stimulation of the quadriceps and hamstrings.** *Ann Biomed Eng*, 16(3):299–310, 1988. 106
- [140] G ALON, G KANTOR, AND H S HO. **Effects of electrode size on basic excitatory responses and on selected stimulus parameters.** *J Orthop Sports Phys Ther*, 20(1):29–35, July 1994. 107, 111, 112
- [141] G ALON. **High voltage stimulation. Effects of electrode size on basic excitatory responses.** *Phys Ther*, 65(6):890–895, June 1985. 107
- [142] G M LYONS, G E LEANE, M CLARKE-MOLONEY, J V O'BRIEN, AND P A GRACE. **An investigation of the effect of electrode size and electrode location on comfort during stimulation of the gastrocnemius muscle.** *Med Eng Phys*, 26(10):873–878, December 2004. 107, 111
- [143] A KUHN, T KELLER, AND M LAWRENCE. **Selective finger and wrist activation using multi-channel transcutaneous electrical stimulation electrodes.** In *International Functional Electrical Stimulation Society Conference*, page 5.2, Philadelphia, PA USA, November 2007. 112
- [144] B J FORRESTER AND J S PETROFSKY. **Effect of electrode size, shape, and placement during electrical stimulation.** *J. Appl. Res*, 4(2):346–354, 2004. 114, 117
- [145] Y STICKLER, J MARTINEK, C HOFER, AND F RATTAY. **Modeling needle stimulation of denervated muscle fibers: voltage-distance relations and fiber polarization effects.** *IEEE Trans Biomed Eng*, 56(10):2396–2403, October 2009. 120
- [146] J MARTINEK, Y STICKLER, M REICHEL, W MAYR, AND F RATTAY. **A novel approach to simulate Hodgkin-Huxley-like excitation with COMSOL Multiphysics.** *Artif Organs*, 32(8):614–619, August 2008. 120
- [147] A OPITZ, W LEGON, A ROWLANDS, AND WK BICKEL. **Physiological observations validate finite element models for estimating subject-specific electric field distributions induced by transcranial magnetic stimulation of the.** *NeuroImage*, 81:253–264, 2013. 120
- [148] A O DE BERKER, M BIKSON, AND S BESTMANN. **Predicting the behavioral impact of transcranial direct current stimulation: issues and limitations.** *Frontiers in human neuroscience*, 7, 2013. 120

Publication List

Published Papers for Thesis

- (i) Gomez-Tames, J.; Gonzalez, J. & Yu, W.: Influence of Different Geometric Representations of the Volume Conductor on Nerve Activation during Electrical Stimulation, Computational and Mathematical Methods in Medicine Journal, Vol. 2014, pp. 1-10, August, 2014
- (ii) Gomez-Tames, J.; Gonzalez, J. & Yu, W.: A Simulation Study on the Dominance of the Tissues' Conductivity in the Muscle Recruitment, Journal of Medical Imaging and Health Informatics, Vol. 3, No.1, pp. 7278, March, 2013

Peer Reviewed Journal Paper

- (iii) Imamoglu, N.; Gomez-Tames, J.; Gonzalez, J.; Gu, D. & Yu, W.: PCNN Segmentation and Bottom-Up Saliency-On Feature Extraction for Thigh MRI based 3D Model Construction, Journal of Medical Imaging and Health Informatics, Vol.4, pp.1-10, June 2014
- (iv) Imamoglu, N.; Gomez-Tames, J. & Yu, W.: Salient Region Detection and Analysis Based on the Weighted Band-Pass Features, Journal of Software Engineering and Applications, Vol.6, No.5B, pp. 43-48, 2013 (Supporting paper)
- (v) Hiroki, C.; Gomez-Tames, J. & Yu, W.: A Cable Driven Robot with Integrated Suction Cups for NOTES Support, Transaction on Control and Mechanical Systems. Vol. 1, No1, pp. 6-12, May, 2012 (Supporting paper)

. PUBLICATION LIST

- (vi) Gomez-Tames, J.; Gonzalez, J. & Yu, W.: A study of thigh muscle activation for transcutaneous electrical stimulation using a 2D and 3D model explanatory models, Vol.25, pp. 39-47, March, 2011
- (vii) Yuan, B.; Sun, G.; Gomez-Tames, J.; Ikemoto, Y.; Gonzalez, J.; Murai, C.; Acharya U, R.; Yu, W. & Ino, S.: The Effect of an Auxiliary Stimulation on Motor Function Restoration by FES, Journal of Medical Systems, Vol. 35, No. 5, pp. 855-861, October, 2011 (Supporting paper)

Peer Reviewed Conference Paper

- (viii) Mahira, T.; Imamoglu, N.; Gomez-Tames, J.; Kita, K. & Yu, W.: Modeling Bi-manual Coordination Using Back Propagation Neural Network and Radial Basis Function Network, IEEE International Conference on Robotics and Biomimetics, 2014
- (ix) Kawamoto, S.; Imamoglu, N.; Gomez-Tames, J.; Kita, K. & Yu, W.: Ultrasound Imaging and Semi-Automatic Analysis of Active Muscle Features in Electrical Stimulation by Optical Flow, Proceedings of the International Conference of Engineering in Medicine and Biology Society, EMBC, August 2014 (Supporting paper)
- (x) Gomez-Tames, J. & Yu, W.: Assessment of nerve morphology in nerve activation during electrical stimulation, In American Institute of Physics Conference Series, Vol. 1559, pp. 355-358, October, 2013
- (xi) Gomez-Tames, J.; Gonzalez, J. & Yu, W.: Influence of the Fat Thickness and the Femur location on the Nerve Activity Computation, Intelligent Engineering Systems, INES, pp. 51-54, June, 2013
- (xii) Gomez-Tames, J.; Gonzalez, J. & Yu, W.: Temporal Muscle Activation Assessment by Ultrasound Imaging During Flexor Withdrawal Reflex and Voluntary Contraction, Proceedings of the International Conference on Engineering in Medicine and Biology Society, EMBC, pp. 3618-3621, July, 2013 (Supporting paper)

-
- (xiii) Fukuhara, Y.; Gomez-Tames, J. & Yu, W.: An experimental study on the effect of fat conductivity on voltage distribution and muscle recruitment using tissue-equivalent phantoms, E-Health and Bioengineering Conference, EHB, pp. 1-4, November, 2013
- (xiv) Imamoglu, N.; Gomez-Tames, J.; Gonzalez, J.; Gu, D. & Yu, W.: Bottom-up Saliency Feature and PCNN based Muscle Segmentation, 2nd International Conference on Engineering and Applied Science, ICEAS, 2013
- (xv) Akagi, T., Gomez-Tames, J., Gonzalez, J., Igarashi, T., & Yu, W.: Ultrasound Energy Transmission for WaFLES-Support Intra-abdominal Micro Robots, Autonomous Control Systems and Vehicles, pp. 279-289, 2013
- (xvi) Gomez-Tames, J.; Gonzalez, J.; Nakamura, S. & Yu, W.: Simulation of the Muscle Recruitment by Transcutaneous Electrical Stimulation in a Simplified Semitendinosus Muscle Model, Converging Clinical and Engineering Research on Neurorehabilitation, pp. 449-453, November, 2012
- (xvii) Gomez-Tames, J.; Gonzalez, J.; and Yu, W.: A simulation study: Effect of the inter-electrode distance, electrode size and shape in Transcutaneous Electrical Stimulation, Proceedings of the International Conference of Engineering in Medicine and Biology Society, EMBC, pp. 3576-3579, 2012
- (xviii) Gomez-Tames, J.; Gonzalez, J. & Yu, W.: Effect of the Electrical Properties of the Tissues in the Nerve Activation Using Transcutaneous Electrical Stimulation, International Conference of Rehabilitation Medical Engineering. Shanghai, 2012
- (xix) Nakamura, S., Gomez-Tames, J., Gonzalez, J., Ojima, S., Yamaguchi, T., & Yu, W.: Ultrasound Imaging and Analysis of Muscle Activity in Lower Limb. Converging Clinical and Engineering Research on Neurorehabilitation, 455-459, 2012
- (xx) Gomez-Tames, J.; Gonzalez, J. & Yu, W.: Influence of Subcutaneous Fat Thickness upon the Activation Volume in Transcutaneous Electrical Stimulation to a Thigh Simulation Model. Proceedings of the International Conference on Functional Electrical Stimulation, IFESS, September, 2011

. PUBLICATION LIST

- (xxi) Gomez-Tames, J.; Gonzalez, J. & Yu, W.: Preliminary Simulation Of The Current Distribution Across The Skin During Surface Stimulation Using Finite Element Analysis, Proceedings of the International Conference on Computers, Communications, Control and Automation (CCCA), pp. 495-4988, February, 2011

Appendix A

Nerve Activation Model

Equation of the compartment model of the nerve

The mathematical equation to obtain the membrane voltage in a compartment model of a myelinated fiber is presented. Equations A.1 and A.2 result from applying Kirchhoff's current law at the node to the compartment model that is shown in Fig. 3.4.

$$I_{c,n} + I_{ion,n} + I_{axon,n} = 0 \quad (\text{A.1})$$

$$c_m \frac{\partial v_{i,n} - v_{e,n}}{\partial t} + I_{ion,n} + \frac{v_{i,n} - v_{i,n-1}}{R/2 + R/2} + \frac{v_{i,n} - v_{i,n+1}}{R/2 + R/2} = 0 \quad (\text{A.2})$$

where $I_{c,n}$ is the membrane current, $I_{ion,n}$ is the ion current, and $I_{axon,n}$ is the axon current.

Equation A.3 calculates the temporal and spatial variation of the membrane voltage (V_n), which is obtained by considering $V = V_i - V_e - V_{rest}$ in every compartment (90).

$$c_m \frac{\partial v_n}{\partial t} = -I_{ion,n} + \frac{v_{n-1} - v_n}{R/2 + R/2} + \frac{v_{n+1} - v_n}{R/2 + R/2} + \frac{v_{e,n-1} - v_{e,n}}{R/2 + R/2} + \frac{v_{e,n+1} - v_{e,n}}{R/2 + R/2} \quad (\text{A.3})$$

or

$$c_m \frac{\partial v_n}{\partial t} = -I_{ion,n} + \frac{v_{n-1} - 2v_n + v_{n+1}}{R} + \frac{v_{e,n-1} - 2v_{e,n} + v_{e,n+1}}{R} \quad (\text{A.4})$$

where c_m is the membrane capacitance and R the intra-axonal resistance between the centers of two adjacent compartments.

Membrane model

The $I_{ion,n}$ to solve the membrane voltage. In the case of the internodes, they are considered as passive membranes and are assumed to have a constant membrane conductance $G_{m,n}$. In contrast, the nodes of Ranvier present non-linear activity. For that, CRRSS model (Chiu-Ritchie-Rogart-Stagg-Swenney) (55, 56), which describes the nonlinear gating mechanism of ion channels across the unmyelinated neuronal membrane, was used to calculate $I_{ion,n}$ at the nodes of Ranvier. The parameters used for simulation are listed in Table A.1.

$$I_{ion,n} = i_{Na} + i_L \quad (\text{A.5})$$

$$I_{ion,n} = G_{Na,n} m^2 h (V_n - E_{Na}) + G_{l,n} (V_n - E_l) \quad (\text{A.6})$$

$$G_{Na,n} = g_{Na} d_n \pi l_n \quad (\text{A.7})$$

$$G_{l,n} = g_l d_n \pi l_n \quad (\text{A.8})$$

where E_{Na} and E_l are the sodium and the leakage equilibrium potentials caused by different ionic concentrations at the inside and outside of the fiber. $G_{Na,n}$ and $G_{l,n}$ are the sodium channel and leakage channel conductance, g_{Na} and g_l are the maximum conductivities per square unit area.

m and h are probabilities of the gating of the sodium channel (with values between 0 and 1) that reduce its maximum conductance

$$\frac{\partial m}{\partial t} = [\alpha_m(1 - m) - \beta_m m]k \quad (\text{A.9})$$

$$\frac{\partial h}{\partial t} = [\alpha_h(1 - h) - \beta_h h]k \quad (\text{A.10})$$

$$k = 3^{(0.1T-3.7)} \quad (\text{A.11})$$

$$\alpha_m = \frac{97 + 0.363V}{1 + \exp(\frac{31-V}{5.3})} \quad (\text{A.12})$$

$$\beta_m = \frac{\alpha_m}{\exp(\frac{V-23.8}{4.17})} \quad (\text{A.13})$$

$$\alpha_h = \frac{\beta_m}{\exp(\frac{V-5.5}{5})} \quad (\text{A.14})$$

$$\beta_h = \frac{15.6}{1 + \exp(\frac{24-V}{10})} \quad (\text{A.15})$$

α and β are voltage dependent variables that characterize the voltage-gated channels. k is a temperature coefficient which accelerates the gating process for temperature higher than the original experimental temperature of 37°C. The initial conditions of the differential equation system are:

$$V(0) = 0 \quad (\text{A.16})$$

$$m(0) = 0.003 \quad (\text{A.17})$$

$$h(0) = 0.75 \quad (\text{A.18})$$

Table A.1: Parameters of the CRRSS nerve model

Parameter	Variable	Value	Unit
Fiber diameter (internode)	D	8 to 20×10^{-4}	cm
Node diameter (axon)	d	$0.64D$	cm
Internode length	L_n	$100D$	cm
Node length	l_n	1.5×10^{-4}	cm
Specific membrane capacity	c_m	1	μ F/cm ²
Axoplasmatic resistivity	ρ_a	0.07	k $\Omega \cdot$ cm
Membrane conductivity	g_m	1	mS/cm ²
Number of myelin sheath layers	N	$75 \times 10^4 D$	1
Sodium channel conductivity	g_{Na}	1445	mS/cm ²
Leak channel conductivity	g_l	128	mS/cm ²
Equilibrium potential for sodium channels	E_{Na}	115	mV
Equilibrium potential for leakage channels	E_l	-0.01	mV

Activation function

The right term of equation A.3 is called activation function (equation A.19). It explains the principle of external stimulation without the inclusion of complicated ion-channel dynamics (91).

$$f_n = \left(\frac{v_{e,n-1} - v_{e,n}}{R/2 + R/2} + \frac{v_{e,n+1} - v_n}{R/2 + R/2} \right) / c_n \quad (\text{A.19})$$

A. NERVE ACTIVATION MODEL

Considering the neural elements are cylinders of constant diameter d and length Δx , and with $R/2 = 2\rho_i \Delta x_n/d^2\pi$, $C_{m,n} = d_n \Delta x_n\pi c_{m,n}$, equation A.19 becomes

$$f_n = \frac{d}{4\rho_i c_m} \frac{v_{e,n-1} - 2v_{e,n} + v_{e,n+1}}{\Delta x_n^2} \quad (\text{A.20})$$

In the case of a long homogeneous fiber (unmyelinated axon or a muscle fiber), the activating function is proportional to the second derivative of the extracellular potential (omitting the endings of the fiber), by considering $\Delta x \rightarrow 0$, where x is the fiber length coordinate.

$$f_n = \frac{d}{4\rho_i c_m} \frac{\partial^2 V_e}{\partial x^2} \quad (\text{A.21})$$

Nerve models review

The table below is a revision of the evolution of different nerve models.

Table A.2: Comparison of nerve models

	HH model (53)	FH model (54) Huxley	CRRSS model (56) Chiu-Ritchie- Rogart-Stagg- Swenney	SE model (101) Schwarz- Eikhof	SRB model (102) Schwarz- Reid- Bostock
Authors	Hodgkin- Huxley	Frankenhaeuser- Huxley	Chiu-Ritchie- Rogart-Stagg- Swenney	Schwarz- Eikhof	Schwarz- Reid- Bostock
Year	1952	1964	1979,1987	1987	1995
Axon	Squid	Frog	Rabbit	Rat	Human
Currents	Na ⁺ , K ⁺ , L	Na ⁺ , K ⁺ , L, Non-specific	Na ⁺ , L	Na ⁺ , K ⁺ , L	Na ⁺ , K _{fast} ⁺ , K _{slow} ⁺ , L
Na ⁺ current role (depolarization)	Fundamental	Fundamental	Fundamental	Fundamental	Fundamental
K ⁺ current role (repolarization)	Fundamental	Important	Almost absent	Very small	Very small ^a
L current role (repolarization)	Small	Important	Fundamental	Fundamental	Fundamental

^a K_{slow}⁺ is important for limitation of repetitive firing.

Appendix B

Lumped Model Equations

Current stimulation

The current in R_{Muscle} that is in parallel with R_{FatL} is obtained using current divider. The following equation describes the variation of the current in the muscle in relationship with the current stimulation.

$$\frac{I_{Muscle}}{I_{Stim}} = \frac{R_{FatL}}{R_{FatL} + R_{Muscle}} \quad (B.1)$$

where $R_{Muscle} = R_{MuscleT} + R_{MuscleL}$.

For low conductivity of the fat layer,

$$\lim_{R_{FatL} \rightarrow \infty} \frac{I_{Muscle}}{I_{Stim}} = \frac{R_{FatL}}{R_{FatL} + R_{Muscle}} = 1 \quad (B.2)$$

For high conductivity of the fat layer,

$$\lim_{R_{FatL} \rightarrow 0} \frac{I_{Muscle}}{I_{Stim}} = 0 \quad (B.3)$$

Voltage stimulation

The voltage in $R_{Muscle} \parallel R_{fatL}$ that is connected in series with R_{FatT} is obtained using voltage divider. The following equation describes the variation of the voltage in the muscle in relationship with the voltage stimulation.

$$\frac{V_{Muscle}}{V_{Stim}} = \frac{R_{Muscle} \parallel R_{FatL}}{R_{FatT} + R_{Muscle} \parallel R_{FatL}} \quad (B.4)$$

B. LUMPED MODEL EQUATIONS

$$\frac{V_{Muscle}}{V_{Stim}} = \frac{R_{Muscle}R_{FatL}}{R_{FatT}R_{FatL} + R_{FatT}R_{Muscle} + R_{FatL}R_{Muscle}} \quad (\text{B.5})$$

Assuming $R_{FatL} = kR_{FatT}$

$$\frac{V_{Muscle}}{V_{Stim}} = \frac{kR_{Muscle}}{kR_{FatT} + R_{Muscle} + kR_{Muscle}} \quad (\text{B.6})$$

For low conductivity of the fat layer,

$$\lim_{R_{FatT} \rightarrow \infty} \frac{V_{Muscle}}{V_{Stim}} = \frac{kR_{Muscle}}{kR_{FatT} + R_{Muscle} + kR_{Muscle}} = 0 \quad (\text{B.7})$$

For high conductivity of the fat layer,

$$\lim_{R_{FatT} \rightarrow 0} \frac{V_{Muscle}}{V_{Stim}} = \frac{k}{(1+k)} \quad (\text{B.8})$$